International Journal of Modern Physics A, Vol. 14, No. 18 (1999) 2791–2886
© World Scientific Publishing Company

B LIFETIMES, MIXING AND CP VIOLATION AT CDF

MANFRED PAULINI

Lawrence Berkeley National Laboratory,
MS 50B-5239, Berkeley, California 94720, USA

Received 5 March 1999

We review the status of bottom quark physics at the CDF experiment. The measurements reported are based on about 110 pb^{-1} of data collected at the Fermilab Tevatron $p\bar{p}$ Collider operating at $\sqrt{s} = 1.8$ TeV. In particular, we review results on B hadron lifetimes, measurements of the time dependence of $B^0\bar{B}^0$ oscillations, and a search for CP violation in $B^0 \to J/\psi K^0_S$ decays. Prospects for future B physics at CDF in the next run of the Tevatron Collider, starting in the year 2000, are also presented.

1. Introduction

In 1977, the bottom quark was discovered as a resonance in the dimuon invariant mass spectrum in 400 GeV proton–nucleus collisions at Fermilab.[1] Soon after the discovery of this new $b\bar{b}$ bound state with a mass of about 9.5 GeV/c^2, the Υ resonances were confirmed in e^+e^- collisions at the DORIS storage ring at DESY.[2] Today, more than 20 years later, all lowest mass bound states containing a b quark have been discovered and are experimentally well established. The pseudoscalar B meson states[a] are $B^0 = |\bar{b}d\rangle$, $B^+ = |\bar{b}u\rangle$, $B^0_S = |\bar{b}s\rangle$ and $B^+_c = |\bar{b}c\rangle$, while $\Lambda^0_b = |bdu\rangle$ is the b baryon ground state with lowest mass. The rest masses of the B hadrons[3] are between 5.3 GeV/c^2 and 6.4 GeV/c^2, approximately six times the mass of a proton. The lowest-lying B hadrons decay via the weak interaction.

B hadrons play a special role among hadrons. The heaviest quark, i.e. the top quark, decays weakly into a real W boson and a b quark before it is able to form a meson with another antiquark through the strong interaction. Therefore, hadrons containing a b quark are the heaviest hadrons experimentally accessible. The principal interest in studying B hadrons in the context of the Standard Model[4] arises from the fact that B hadron decays provide valuable information on the weak mixing matrix, i.e. the Cabibbo–Kobayashi–Maskawa (CKM) matrix.[5,6] In fact, B decays measure five of the nine CKM matrix elements: V_{cb}, V_{ub}, V_{td}, V_{ts} and V_{tb}. Future interest in B physics certainly lies in the study of CP violation in the system of B mesons.

[a]Throughout the paper, unless otherwise noted, references to a specific charge state are meant to imply the charge conjugate state as well.

Traditionally, B physics has been the domain of e^+e^- machines operating on the $\Upsilon(4S)$ resonance or the Z^0 pole. But the UA 1 collaboration has already shown that B physics is feasible in a hadron collider environment (for a review see Ref. 7). Although B physics did not play a significant role in the considerations for the original 1981 technical design report of the Collider Detector at Fermilab (CDF), several features in the CDF design are advantageous for the studies of B decays. These features include a large solenoidal magnetic tracking volume, a well-segmented calorimeter for the detection of electrons, and muon chambers that allow low momentum muon detection. However, the device that made B physics possible at CDF in a competitive way, allowing for a broad B physics program, is a silicon microvertex detector, installed in 1992.

There are several motivations for pursuing B physics at the Fermilab Tevatron $p\bar{p}$ Collider operating at $\sqrt{s} = 1.8$ TeV. The primary reason is demonstrated by comparing the B production cross section in e^+e^- collisions — which is about 1 nb at the $\Upsilon(4S)$ and about 6 nb at the Z^0 pole — to the large b quark production cross section at a hadron collider. At the Tevatron, σ_b is $\sim$50 μb within the central detector region of rapidity less than 1. This is a huge cross section which results in about $5 \cdot 10^9$ $b\bar{b}$ pairs being produced in 100 pb^{-1} of data. However, the total inelastic cross section at the Tevatron is still about three orders of magnitude larger than the b cross section. This puts certain requirements on the trigger system used to find B decay products, as will be further discussed later.

In addition to high rates of B hadrons, the Tevatron offers other features worth noting. First, in contrast to an e^+e^- machine operating at the $\Upsilon(4S)$, all B hadron species are produced at a hadron collider. Second, the transverse momentum spectrum for B hadrons scales with the B mass and is significantly harder for heavy hadrons than that for light hadrons. As a result, the B hadrons are Lorentz-boosted at all rapidities, including the central detector region where the production rate is the highest with an average transverse B momentum around 4–5 GeV/c. Third, the hard B hadron momentum spectrum can be exploited to improve the signal-to-background ratio in finding B decay products. For all momenta, b production accounts for about 0.2% of the total $p\bar{p}$ inelastic cross section, while at high momenta the ratio of b jet to inclusive jet production is close to 2%. Finally, the initial $p\bar{p}$ state is a CP symmetric state where we expect equal rates of B and $\bar{B}$ hadrons to be produced, at least in the central detector region.

In this article, we review recent B physics results at CDF concentrating on B lifetime measurements, proper-time-dependent measurements of $B^0\bar{B}^0$ oscillations, and the search for CP violation in $B^0 \to J/\psi K^0_S$. The measurements reported here are based on about 110 pb^{-1} of data collected at the Fermilab Tevatron Collider. Prospects for future B physics at CDF in the next run of the Tevatron, starting in the year 2000, are also discussed.

The outline of this paper is as follows. In Sec. 2, we give a brief overview of heavy quark production in $p\bar{p}$ collisions. In Sec. 3, we describe the experimental environment including the Tevatron Collider, as well as the CDF detector. We

focus on the collection of B physics datasets at CDF in Sec. 4, emphasizing the CDF trigger scheme. In Sec. 5, we highlight several features of B physics in a hadron collider environment and describe some of the ways B decays are studied at CDF. Section 6 is devoted to the measurements of B hadron lifetimes, where the lifetimes of all weakly decaying B mesons as well as the Λ_b^0 baryon are measured at CDF. We then review several proper-time-dependent measurements of $B^0\bar{B}^0$ oscillations in Sec. 7 and discuss various B tagging methods to identify the B flavor in hadronic collisions. The search for CP violation using the current data set of $B^0 \to J/\psi K_S^0$ decays is summarized in Sec. 8. An outlook for future B physics at CDF in the next run of the Tevatron Collider, starting in the year 2000, is given in Sec. 9. Finally, we offer our conclusions in Sec. 10.

2. Heavy Quark Production in Hadronic Collisions

In this section, we give a short introduction to heavy quark production in $p\bar{p}$ collisions. By the expression "heavy quark" we will mainly refer to b quarks. The discussion will be rather qualitative and cannot serve as a complete review of heavy quark production in hadronic collisions. It is meant to give an idea of the main issues, introducing some of the nomenclature often used in the literature. The interested reader is referred to reviews in Refs. 8–10. Here, we first discuss the parton model and parton distribution functions. Then, we summarize heavy quark production in lowest order QCD, as well as next-to-leading-order QCD calculations, and discuss hadronization of heavy quarks. Finally, we briefly compare theoretical predictions of b quark production to measurements at CDF.

2.1. *Parton model and parton distribution functions*

In a static picture, a proton is a bound state of three quarks $|uud\rangle$ with a radius of about 1 fm. However, in a hadronic collision such as that found at the Tevatron, a proton is better characterized as a beam of free partons: three constituent quarks (valence quarks), virtual gluons and quark–antiquark pairs (sea quarks).[8] The different partons do not necessarily divide up the beam energy equally. The distribution of partons within the proton is described by the so-called parton distribution function (PDF) $F_i^a(x, Q^2)$, which is the number density of parton i (quark or gluon) carrying the momentum fraction x of the hadron a (proton or antiproton) when probed at momentum transfer Q^2.

Information on parton distributions comes from measurements of deep inelastic lepton or nucleon scattering, such as ep, eN, μN or νN. Once parton distributions have been measured at some value of Q^2 (normally at low Q^2), and the running coupling constant $\alpha_s(Q^2)$ of the strong interaction has been determined, QCD permits one to compute the parton distributions at higher values of Q^2 based on the formalism provided by the Altarelli–Parisi equations[11] and the evolution calculations pioneered by Dokshitzer, Gribov and Lipatov.[12] Modern representations and predictions of parton distribution functions, used for comparison with

hadron collider data, come, for example, from the Martin–Roberts–Stirling (MRS) group[13,14] or from a collaboration of theorists and experimentalists called the CTEQ collaboration.[15]

As an example, Fig. 1(a) illustrates the flavor content of the proton as measured by the momentum fraction $\int_0^1 dx\, xF_i(x, Q^2)$ carried by each parton species i, as obtained for the CTEQ4 parton distributions.[16] Gluons carry about half of the proton's momentum almost independently of Q^2, while the momentum is shared more and more equally among the quark and antiquark flavors as Q^2 increases.

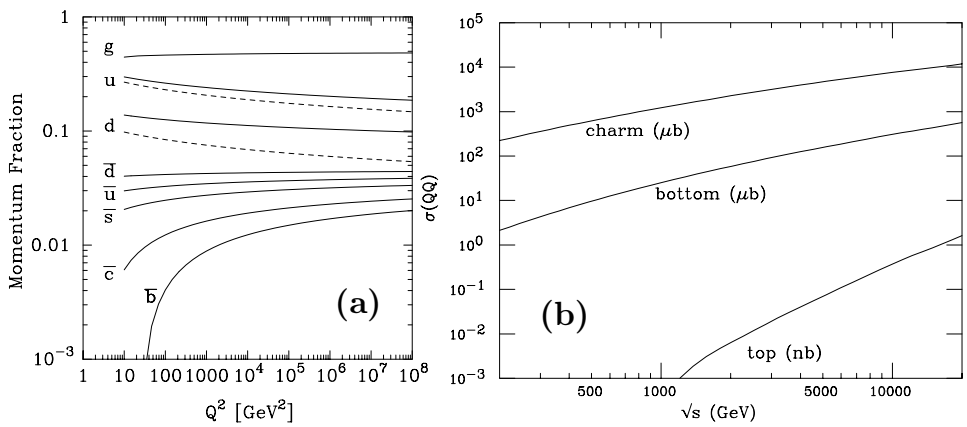

Fig. 1. (a) Q^2 evolution of the momentum fractions carried by the various parton species in the proton for the CTEQ4 parton distributions.[16] (b) Total production cross sections for charm, bottom and top quark pairs in $p\bar{p}$ collisions[10] as a function of the hadronic center-of-mass energy $\sqrt{s}$.

2.2. *QCD predictions for hard scattering in $p\bar{p}$ collisions*

In a $p\bar{p}$ interaction at the Tevatron, heavy quarks $\mathcal{Q}$ are produced in the hard collision of two partons, one from each hadron. In terms of the rapidity y, defined as

$$y = \frac{1}{2} \ln \left(\frac{E + p_z}{E - p_z} \right) , \tag{1}$$

and transverse momentum p_t, the relativistically invariant phase space volume element of the final state heavy quark with four-momentum (E, p_x, p_y, p_z) is

$$\frac{d^3p}{E} = dy\, d^2p_t \,. \tag{2}$$

The differential partonic cross section $\hat{\sigma}_{ij}$ per invariant phase space volume for the production of a heavy quark in a given parton–parton subprocess can be written as

$$\frac{d^3\hat{\sigma}_{ij}}{d^3p/E} = \frac{E\, d^3\hat{\sigma}_{ij}}{d^3p}(x_i p_a, x_j p_b, p; m_{\mathcal{Q}}, \Lambda, \mu_R, \mu_F) \,, \tag{3}$$

where $x_i p_a$ and $x_j p_b$ are the momenta of the incoming partons i and j, p is the momentum of the outgoing heavy quark, and p_a and p_b are the momenta of the

colliding hadrons. The remaining variables are parameters of the theory: $m_{\mathcal{Q}}$ is the mass of the heavy quark, Λ determines the coupling strength of the strong interaction expressed through α_s, μ_R is the renormalization scale (which is related to the energy scale used in the evaluation of α_s), and μ_F is the factorization scale used in the evolution of the parton densities. In QCD, the partonic cross section can be expressed as a perturbative expansion in α_s, provided $m_{\mathcal{Q}}$ is sufficiently large.

The cross section for heavy quark production in the collision of two hadrons ($a + b \to \mathcal{Q} + X$) is then obtained by convoluting the partonic cross section above with parton distribution functions $F_i(x, Q^2)$, where it is common to equate the momentum transfer $Q^2 = m_{\mathcal{Q}}^2 + p_t^2$ with $\mu^2 = \mu_R^2 = \mu_F^2$. Note that the uncertainty on the choice of the μ scale, which is not extractable from the data, is one of the large sources of uncertainties in QCD predictions of heavy quark production. The perturbative QCD formula for the inclusive production of a heavy quark in a hadron–hadron collision is then given as

$$\frac{E\, d^3\sigma}{d^3p} = \sum_{ij} \int dx_i\, dx_j \left(\frac{E\, d^3\hat{\sigma}_{ij}}{d^3p}(x_i p_a, x_j p_b, p; m_{\mathcal{Q}}, \Lambda, \mu) \right) F_i^a(x_i, \mu^2) F_j^b(x_j, \mu^2)\,. \tag{4}$$

The corrections to Eq. (4) are suppressed by powers of the heavy quark mass. Finally, the total cross section for the production of a heavy quark is obtained by integrating Eq. (4) over momentum p. As a further illustration, Fig. 1(b) compares the total production cross sections for charm, bottom and top quark pairs in $p\bar{p}$ collisions[10] as a function of the hadronic center-of-mass energy $\sqrt{s}$. Note the different units used for top quarks compared to charm and bottom.

2.2.1. *$b\bar{b}$ production in leading order QCD*

The leading order (LO) α_s^2 diagrams for heavy flavor production are the $2 \to 2$ processes of gluon–gluon fusion $g + g \to \mathcal{Q} + \bar{\mathcal{Q}}$ as shown in Figs. 2(a)–(c) and the quark–antiquark annihilation $q + \bar{q} \to \mathcal{Q} + \bar{\mathcal{Q}}$ displayed in Fig. 2(d), respectively. In the latter process, the $\mathcal{Q}\bar{\mathcal{Q}}$ pair is always in a color octet state while in $gg \to \mathcal{Q} + \bar{\mathcal{Q}}$ both color singlet and octet are allowed. The gluon–gluon fusion process is the dominant production mechanism for b quarks at the Tevatron, while top quarks are mainly produced from the quark–antiquark annihilation process. The lowest order $\mathcal{O}(\alpha_s^2)$ matrix elements in the α_s expansion and the cross sections for these processes have been available in the literature for some time.[17]

We briefly summarize some of the phenomenological consequences of the $\mathcal{O}(\alpha_s^2)$ processes. First, we note that the partonic cross section $\hat{\sigma}$ is proportional to $\alpha_s^2/m_{\mathcal{Q}}^2$. The average transverse momentum of the heavy quark grows approximately with its mass $\langle p_t(\mathcal{Q})\rangle \sim m_{\mathcal{Q}}$, meaning that the average b quark transverse momentum is about 4–5 GeV/c. In addition, the p_t distribution falls rapidly to zero as p_t becomes larger than the heavy quark mass. Furthermore, the heavy quark and antiquark are produced back-to-back in the parton–parton center-of-mass rest frame and are

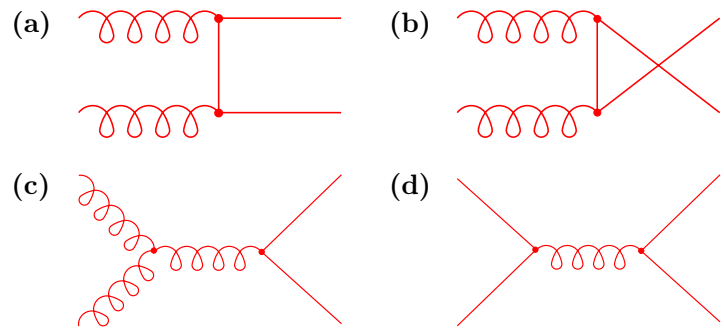

Fig. 2. Lowest order $\mathcal{O}(\alpha_s^2)$ diagrams for heavy quark production through (a)–(c) gluon–gluon fusion and (d) quark–antiquark annihilation.

correspondingly back-to-back in the plane transverse to the colliding hadron beams. In addition, the rapidity distribution of the $\mathcal{Q}\bar{\mathcal{Q}}$ pair has a typical bell shape, becoming wider and flatter as the partonic energy grows. This means that heavy quark production is larger in the central region falling at higher rapidities. The rapidity difference between the $\mathcal{Q}$ and $\bar{\mathcal{Q}}$ tends to be of order unity. But for a fixed value of p_t, the production rate is highly suppressed when the rapidity difference becomes large, which means that $\mathcal{Q}$ and $\bar{\mathcal{Q}}$ tend to be produced with similar rapidity.

2.2.2. *$b\bar{b}$ production in next-to-leading-order QCD*

The next-to-leading-order (NLO) terms in the α_s expansion were originally considered "corrections" to the LO terms. But, it was soon recognized that the higher order corrections could be large.[18] It was noticed that the process $g+g \to g+g$ with $g \to \mathcal{Q}+\bar{\mathcal{Q}}$, which is formally of order α_s^3, can be as important as the lowest order processes because the cross section for the production of gluons $g+g \to g+g$ is about a hundred times larger than the LO cross section for the process $g+g \to \mathcal{Q}+\bar{\mathcal{Q}}$. The complete calculations of NLO corrections to heavy quark production in hadronic collisions have been performed by several authors.[19,20] It has been shown that the $\mathcal{O}(\alpha_s^3)$ terms are actually larger than the lowest order processes for b and c quark production, if the hadron–hadron center-of-mass energy is much larger than $m_{\mathcal{Q}}$, which is the case for the Tevatron.

Examples of order α_s^3 diagrams are displayed in Fig. 3. These processes include real emission matrix elements [Fig. 3(a)] and the interference of virtual matrix elements with the leading order diagrams shown in Fig. 3(b). Other NLO contributions come from gluon splitting diagrams [Fig. 3(c)] or the flavor excitation process as displayed in Fig. 3(d). In the gluon splitting case, the probability of finding a heavy quark from a gluon with large p_t has a logarithmic increase. Phenomenologically, the $\mathcal{Q}\bar{\mathcal{Q}}$ pair is produced close in phase space and will often appear as a single jet. In the flavor excitation process, the heavy quark is considered to be already present with a certain heavy quark density in the incoming hadron. It is excited

by the exchange of a gluon with the other hadron and appears on mass shell in the final state. In the case of a flavor excitation process, only one of the quarks from the $\mathcal{Q}\bar{\mathcal{Q}}$ pair is usually at high p_t.

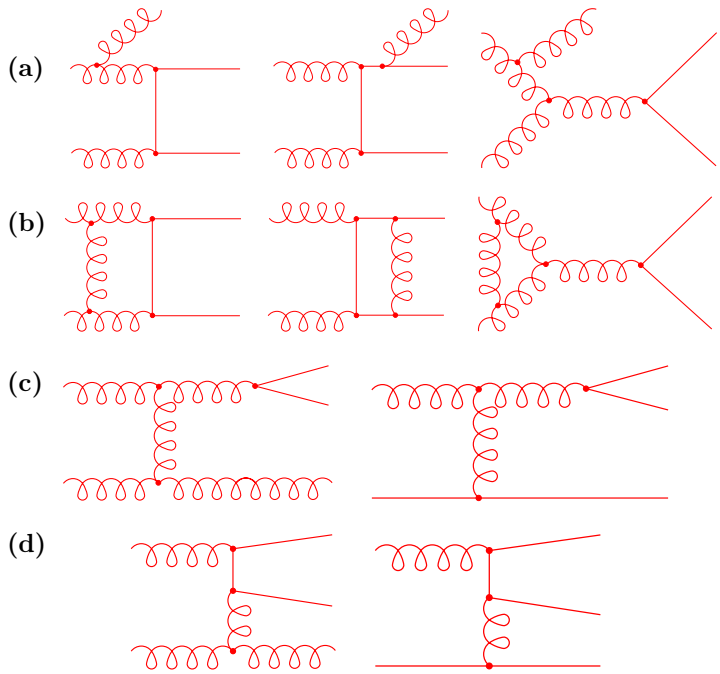

Fig. 3. Examples of diagrams for heavy quark production at next-to-leading order: (a) real emission diagrams, (b) virtual emission diagrams, (c) gluon splitting and (d) flavor excitation.

In summary, NLO processes are an important contribution to b quark production in $p\bar{p}$ collisions at $\sqrt{s} = 1.8$ TeV. These processes are the source of $b\bar{b}$ pairs that can be close together in phase space and do not necessarily appear in the central detector region as compared to the LO processes which result in back-to-back quark pairs. However, there is evidence (see Subsec. 2.4.) that NLO processes are not sufficient for obtaining accurate estimates since large μ-scale dependences are still present. These are an indication that higher order corrections could be large.

2.3. *Hadronization of b quarks*

Once b quarks are produced through the initial hard scattering, the process of forming B hadrons follows and is called hadronization or fragmentation. It is a low Q^2 process and is beyond the reach of perturbative QCD calculations. The hadronization process is therefore described by semiempirical models inspired by theory. A commonly used approach is the string fragmentation model.[21] In a naive picture, we can imagine a "cloud" of gluons acting as a string between the b and

$\bar{b}$ quark pair. As the quark and antiquark separate, the string stretches until it breaks and a new $q\bar{q}$ pair is created out of the vacuum to form the new ends of the string. These new strings also stretch and break, producing more quark–antiquark pairs until there is no longer sufficient energy available to generate new $q\bar{q}$ pairs. The particles produced in this hadronization process, along with the B hadron, are usually referred to as fragmentation particles. The fraction of the initial b quark momentum transferred to the B hadron is commonly described by a so-called fragmentation function, suggested, for example, by Peterson *et al.*[22] for the case of a heavy quark $\mathcal{Q}$ forming a hadron together with a light quark $\bar{q}$:

$$\frac{dN}{dz} \propto \frac{1}{z} \cdot \left(1 - \frac{1}{z} - \frac{\epsilon_b}{1-z}\right)^{-2} . \tag{5}$$

Here, ϵ_b is the so-called Peterson fragmentation parameter, related to the ratio of the effective light and heavy quark masses, $\epsilon_b \sim (m_{\bar{q}}/m_{\mathcal{Q}})^2$. The variable z is originally defined as $z = (E + p_{\parallel})_{\mathcal{Q}\bar{q}}/(E + p_{\mathcal{Q}})$, where $p_{\parallel}$ is the projection of the momentum of the hadron onto the direction of the heavy quark before hadronization. This variable is often approximated with experimentally better accessible parameters, such as $x_p = p/p_{\max}$ or $x_E = E_{\text{hadron}}/E_{\text{beam}}$ used in e^+e^- annihilation.

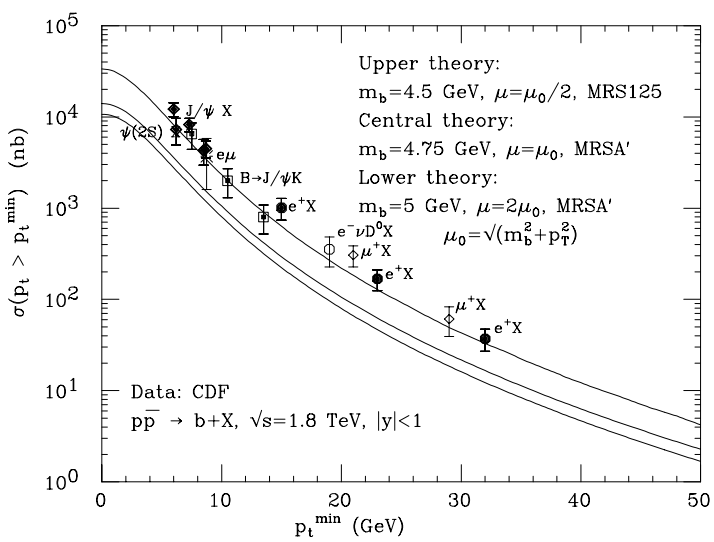

Fig. 4. Integrated cross section for b quark production versus p_t compared to the results of next-to-leading-order QCD predictions.[9]

2.4. *Comparison of heavy quark production with CDF data*

To conclude our review of heavy quark production, we compare in Fig. 4, taken from Ref. 9, various CDF measurements of b quark production with NLO predictions. The distribution most commonly studied by hadron collider experiments is the

b quark differential p_t spectrum, integrated above a given p_t threshold $p_t^{\min}$ and within a fixed rapidity range which is usually set to $y_{\max} = 1$ at CDF:

$$\sigma(p_t > p_t^{\min}) = \int_{|y|<y_{\max}} dy \int_{p_t > p_t^{\min}} dp_t \frac{d^2\sigma}{dy\, dp_t} \,. \tag{6}$$

Different techniques, involving primarily CDF's silicon vertex detector to improve background rejection, are used to obtain the data points from, for example, high-$p_t J/\psi$ mesons reconstructed through $\mu^+\mu^-$ or high-p_t leptons accompanied by a nearby charm meson (D^0). The measurements are compared to NLO QCD calculations which agree very well in shape with the data. However, the data are higher by a factor of almost 3 than the default prediction based on $\mu = \mu_0 = \sqrt{p_t^2 + m_b^2}$. Using variations on, for example, m_b, μ, and the parton distribution function, theory is able to accommodate the data, as indicated by the upper curve in Fig. 4. Since the production of b quarks and B hadrons is not the subject of this review, we refer to the literature[9,23] for a further discussion on this issue.

3. Experimental Environment

In this section, we summarize the experimental environment beginning with the Tevatron Collider. We then describe the CDF detector, emphasizing the device that made a broad B physics program possible at CDF, i.e. the silicon microvertex detector.

3.1. *Tevatron collider*

The Fermilab Tevatron, with a circumference of 6.28 km, is a proton–antiproton collider operating at a center-of-mass energy of $\sqrt{s} = 1.8$ TeV. The Tevatron delivered its first physics collisions in 1987. In this article, however, we will concentrate on the data taking period referred to as Run I, which started in May 1992 and ended in Feb. 1996. During that time, the Tevatron operated with six bunches of protons and six bunches of antiprotons crossing every 3.5 μs at CDF's interaction region.

Figure 5 shows a time profile of the delivered and accumulated luminosity at CDF throughout Run I. During this period, a total integrated luminosity of about 175 pb^{-1} was delivered to the CDF experiment. During Run I, the highest instantaneous luminosities reached were around $2.5 \cdot 10^{31}$ cm^{-2}s^{-1}. The Run I running period was divided up into Run Ia, from May 1992 through June 1993, Run Ib, from Dec. 1993 to July 1995, and a Run Ic, from Dec. 1995 to Feb. 1996. The collected integrated luminosities of data used for physics analyses were about 19.3 pb^{-1} for Run Ia, approximately 90 pb^{-1} for Run Ib, and about 10 pb^{-1} for Run Ic. However, the Run Ic data taking period was dedicated to the accumulation of very specialized trigger datasets and is usually not included in Run I physics analyses, resulting in about 110 pb^{-1} of data used for physics results from Run I.

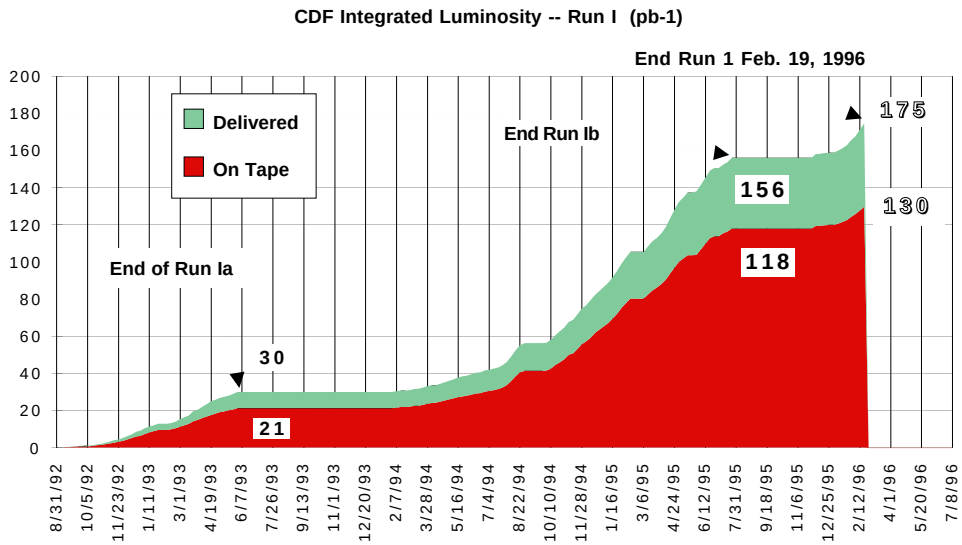

Fig. 5. Time profile of the luminosity delivered by the Tevatron Collider and accumulated by the CDF experiment throughout Run I.

All measurements presented in this paper refer to this Run I luminosity, unless otherwise noted.

3.2. *CDF detector*

The CDF detector is a multipurpose apparatus designed to study 1.8 TeV $p\bar{p}$ collisions produced by the Fermilab Tevatron Collider. It has both azimuthal and forward–backward symmetry. A superconducting solenoid, 4.8 m in length and 1.5 m in radius, generates a 1.4 T magnetic field containing tracking chambers used to detect charged particles and measure their momenta. Surrounding the solenoid, sampling calorimeters measure electromagnetic and hadronic energies of jets, electrons and photons. Outside the calorimeters are drift chambers for muon detection.

A schematic view of the CDF experiment can be found in Fig. 6, while a side-view quarter cross section of the CDF detector is displayed in Fig. 7. The CDF experiment uses a coordinate system with the z axis along the proton beam direction, the y axis pointing vertically upwards, and the x axis pointing horizontally out of the Tevatron ring. Throughout this article, φ is the azimuthal angle, θ is the polar angle measured from the proton direction, and r is the radius perpendicular to the beam axis. The pseudorapidity η is defined as $\eta = -\ln[\tan(\theta/2)]$. The transverse momentum p_t is the component of the track momentum p transverse to the z axis ($p_t = p \cdot \sin\theta$), while $E_t = E \cdot \sin\theta$, with E being the energy of the calorimeter cluster. A more complete description of the CDF detector can be found elsewhere.[24] We summarize here only those detector features most relevant to B physics.

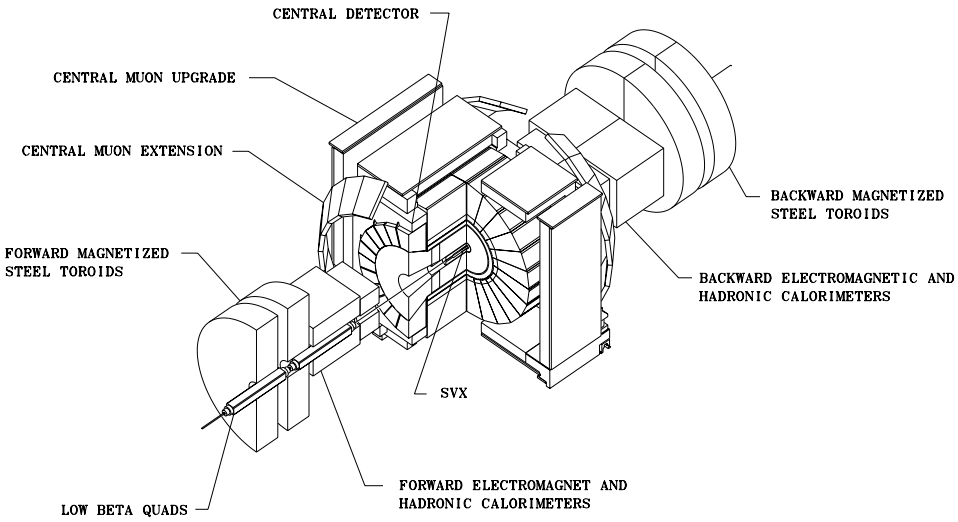

Fig. 6. Schematic view of the CDF detector.

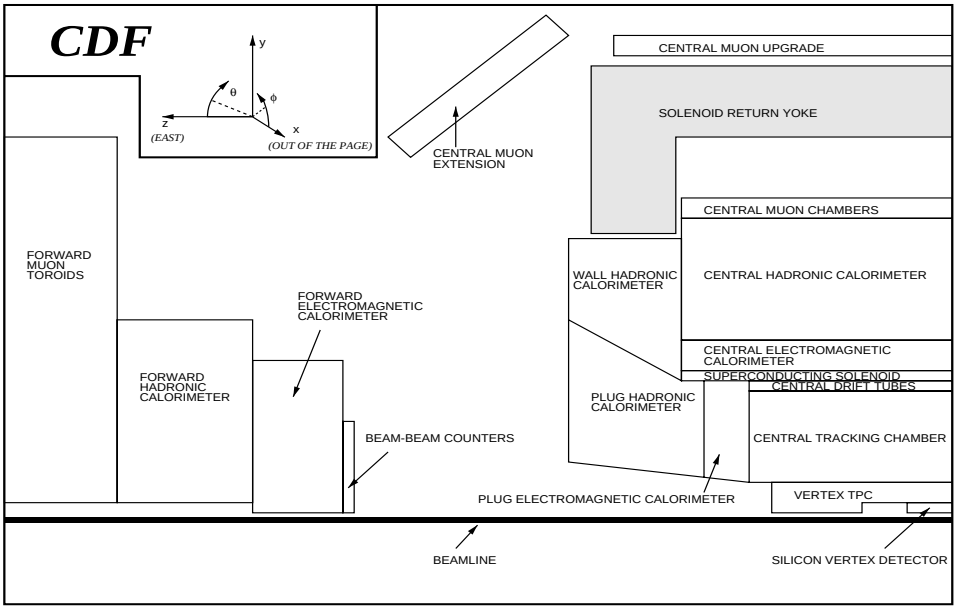

Fig. 7. Side-view quarter cross section of the CDF detector. For a full view, the image is to be reflected to the left and below. The $p\bar{p}$ interaction point is at the lower right corner of the figure.

Three devices inside the 1.4 T solenoidal magnetic field are used for the tracking of charged particles: the silicon vertex detector (SVX), a set of vertex time projection chambers (VTX), and the central tracking chamber (CTC). The SVX is described in more detail in Subsec. 3.2.1. The VTX, which is located outside the

SVX up to a radius of 22 cm, reconstructs track segments in the rz plane up to $|\eta| < 3.25$. The VTX is used to determine the z position of the primary interaction vertex with a resolution of about 0.2 cm on average.

Surrounding the SVX and VTX is the CTC, located between radii of 30 cm and 132 cm. The CTC is a 3.2-m-long cylindrical drift chamber that contains 84 layers of sense wires grouped into nine alternating superlayers of axial and stereo wires with a stereo angle of 3°. The CTC provides three-dimensional tracking and covers the pseudorapidity interval $|\eta|$ less than about 1.1. The outer 54 layers of the CTC are instrumented to record the specific ionization dE/dx of charged particles.

Outside the solenoid are electromagnetic (CEM) and hadronic (CHA) calorimeters ($|\eta| < 1.1$) which employ a projective tower geometry back to the nominal interaction point with a segmentation of $\Delta\eta \times \Delta\varphi \sim 0.1 \times 15°$. The sampling medium is composed of scintillators layered with lead absorbers in the electromagnetic calorimeter and steel in the CHA. The energy resolution for the CDF central calorimeter is $\sigma(E_t)/E_t = [(13.5\%/\sqrt{E_t})^2 + (2\%)^2]^{1/2}$ for electromagnetic showers and $\sigma(E_t)/E_t = [(50\%/\sqrt{E_t})^2 + (3\%)^2]^{1/2}$ for hadrons with E_t measured in GeV. A layer of proportional chambers (CES), with wire and strip readout, is located six radiation lengths deep in the CEM calorimeters, approximately near the shower maximum for electromagnetic showers. The CES provides a measurement of electromagnetic shower profiles in both the φ and z directions. Proportional chambers located between the solenoid and the CEM constitute the central preradiator detector (CPR), which samples the early development of electromagnetic showers in the material of the solenoid coil, providing information in $r\varphi$ only. Finally, plug and forward calorimeters instrument the region of $1.1 < |\eta| < 4.2$. These consist of gas proportional chambers as active media, while lead and iron are used as absorber materials.

The central calorimeters act as a hadron absorber for the muon detection system. Four of its layers of planar drift chambers (CMU) are located beyond the central calorimeters. The CMU system covers $|\eta| \leq 0.6$ and can be reached by muons with p_t in excess of 1.4 GeV/c. To reduce the probability of misidentifying penetrating hadrons as muon candidates in the central detector region, four additional layers of drift chambers (CMP) were added in 1992 and are located behind 0.6 m of steel outside the CMU system. Approximately 84% of the solid angle for $|\eta| \leq 0.6$ is covered by the CMU detector, 63% by the CMP, and 53% by both. To reach these two detectors, particles produced at the primary interaction vertex, with a polar angle of 90°, must traverse material totaling 5.4 and 8.4 pion interaction lengths, respectively. An additional set of muon chambers (CMX) is located in the pseudorapidity interval $0.6 < |\eta| < 1.0$ to extend the polar acceptance of the muon system. Approximately 71% of the solid angle for $0.6 < |\eta| < 1.0$ is covered by the free-standing conical arches of the CMX. Finally, the forward muon system (FMU) is a magnetic spectrometer consisting of three planes of drift chambers surrounding two 1-m-thick iron toroids located ±10 m from the interaction point.

3.2.1. *CDF silicon microvertex detectors*

Surrounding the 1.9 cm radius beryllium beampipe is the CDF silicon microvertex detector (SVX)[25] originally installed at CDF in 1992. The SVX is 51 cm long and consists of two identical cylindrical modules which meet at $z = 0$, with a gap of 2.15 cm between them. A sketch of one of these modules is shown in Fig. 8(a). Both SVX modules consist of four layers of silicon microstrip detectors segmented into 12 30° wedges. The basic detector element is called a ladder and is shown in Fig. 8(b). There are 96 such ladders in the complete detector. The four layers of the SVX are located at radii of 2.9 cm, 4.2 cm, 5.7 cm and 7.9 cm from the beamline. Axial microstrips, with a 60 μm pitch on the three innermost layers and a 55 μm pitch on the outermost layer, provide precision spatial measurements in the $r\varphi$ plane transverse to the beam. The geometric acceptance of the SVX is about 60% of the $p\bar{p}$ interactions, as it covers only $\pm$ 25 cm from the nominal interaction point, whereas the luminous region of the Tevatron beam has an RMS of $\sim$30 cm along z.

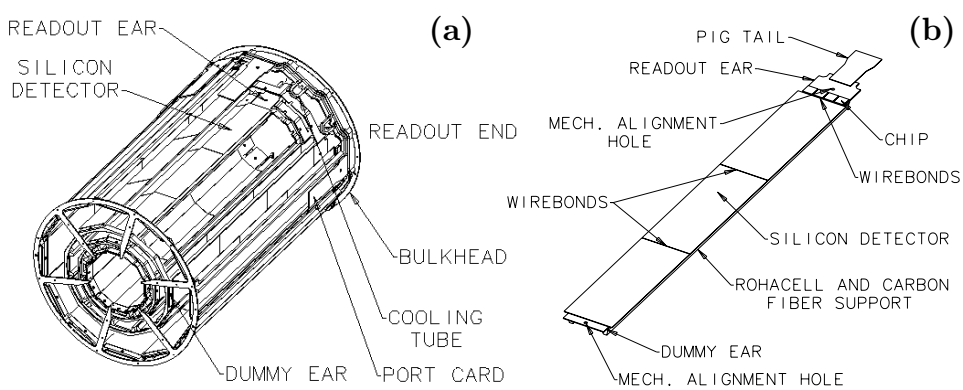

Fig. 8. (a) Isometric view of one of the SVX cylindrical modules. (b) Sketch of a ladder detector.

Because of radiation damage to the SVX readout chip, the performance of the SVX deteriorated over the course of the Run Ia data taking period. At the beginning of Run Ib, the SVX was replaced with a new silicon vertex detector (SVX′)[26] which is equipped with a radiation hard readout chip able to tolerate more than 1 MRad of radiation. The typical charge gain of the readout chip is around 21 mV/fC, with typical values for the noise of around 1300 electrons (10.8 ADC counts), compared to about 2200 electrons for the original SVX detector. One improvement in noise level resulted from the fact that SVX′ is AC-coupled, in comparison to SVX, which was DC-coupled. This allowed the SVX′ detector to be operated in double sample and hold mode, with one charge integration, resulting in a reduction in noise by a factor of $\sqrt{2}$ compared to SVX, which was operated in quadruple sample and hold mode, with two successive charge integrations for the determination of the outgoing signal.

The SVX′ position resolution is found to be better than 10 μm after alignment of the detector, using track data, as can be seen in Fig. 9(a). Here, the residual distribution of the distance of track intersection from reconstructed cluster centroids on an SVX′ layer is plotted. The track impact parameter resolution is measured to be about $(13 + 40/p_t)$ μm, with p_t given in GeV/c. In Fig. 9(b), the SVX track impact parameter resolution is shown versus $1/p_t$. Note the contribution from

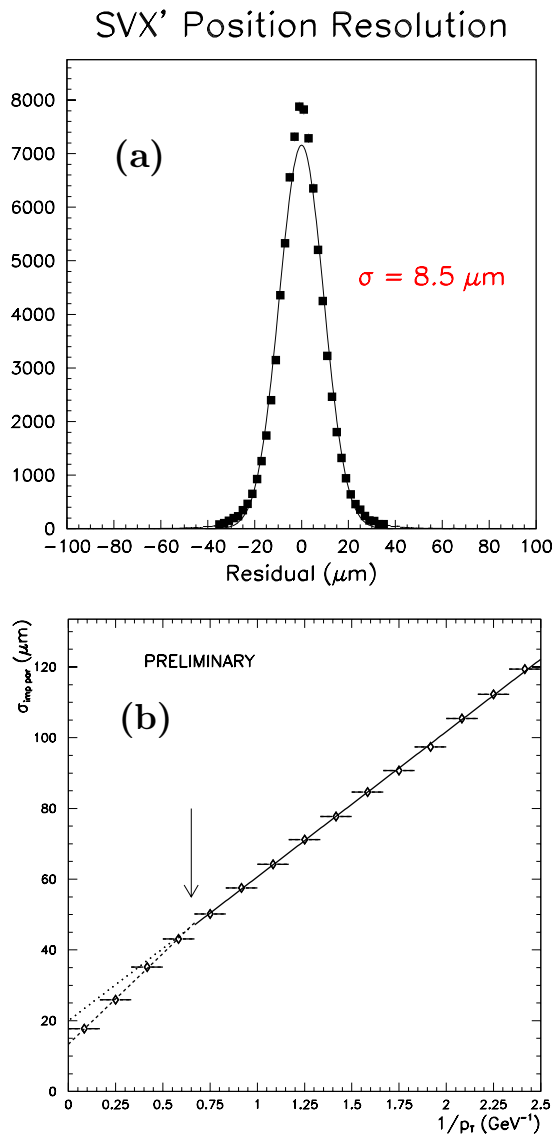

Fig. 9. (a) SVX′ residual track position resolution. (b) Track impact parameter resolution versus $1/p_t$.

multiple scattering at low p_t, while the impact parameter resolution at high p_t is dominated by the intrinsic detector resolution. The p_t resolution of the CTC combined with the SVX is $\sigma(p_t)/p_t = [(0.0066)^2+(0.0009\,p_t)^2]^{1/2}$, with p_t measured in GeV/c, while, for CTC tracks alone, the resolution is $\sigma(p_t)/p_t = [(0.0066)^2 + (0.002\,p_t)^2]^{1/2}$.

4. Collection of B Physics Data

In this section, we describe the collection of datasets used for B physics analyses. We begin with the description of the B physics trigger data sets, followed by a summary of the selection requirements used to identify leptons, hadrons and jets. At the end of this section, we describe the Monte Carlo simulation of CDF's B physics data.

4.1. *B physics triggers*

The total inelastic $p\bar{p}$ cross section at the Tevatron is about three orders of magnitude larger than the b production cross section, putting certain requirements on the trigger system in terms of finding B decay products. In addition, the cross section for b quark production is a steeply falling cross section, as seen in Fig. 4. It drops by almost two orders of magnitude between a b quark p_t of about 8 GeV/c and 25 GeV/c. In order to find B decay products in hadronic collisions, it is desirable to go as low as possible in the decay products transverse momentum, exploiting as much as possible of the steeply falling b cross section. Of course, the limiting factor is the bandwidth of CDF's data acquisition system. Throughout Run I, the CDF collaboration was able to maintain low p_t thresholds, without increasing the deadtime of the experiment during data taking.

In Run I, all B physics triggers at CDF are based on leptons. Inclusive single lepton triggers (e and μ) and dilepton triggers (dimuon and $e\mu$) both exist. CDF uses a three-level trigger system to identify events to be written to tape. The first two levels are hardware-based triggers. The Level 1 trigger uses information from detector subsystems, such as the muon chambers or the calorimeter, reducing the beam crossing rate from about 300 kHz to about 2 kHz. At Level 2, information from different detector subsystems is combined, such as a track stub in the CTC with hits in the muon chambers. This reduces the trigger rate to about 30 Hz. Level 3 is a software trigger based on the offline reconstruction code, optimized for computational speed, resulting in an event rate to tape of up to 10 Hz.

4.1.1. *Inclusive single lepton trigger*

The inclusive single lepton trigger identifies events with at least one electron or one muon, providing datasets enriched in events from semileptonic B decays. Inclusive electrons are selected at Level 1 by the presence of a single calorimeter tower above a threshold of 6–8 GeV, depending on run conditions, while inclusive muons require

the presence of a track in the CMU as well as the CMP. At Level 2, both of these triggers demand a charged track with $p_t > 7.5$ GeV/c reconstructed in the $r\varphi$ plane of the CTC by the central fast tracker (CFT),[27] a hardware track processor, which uses fast timing information from the CTC as input. The momentum resolution of the CFT is $\sigma(p_t)/p_t^2 = 3.5\%$ with a high efficiency. In the case of the electron trigger, this track has to be matched to a cluster in the electromagnetic calorimeter with transverse energy $E_t > 8.0$ GeV. In the case of the muon trigger, this track must be matched to a reconstructed track segment in both the CMU and the CMP. The trigger efficiency for a single lepton turns on at $p_t \sim 6$ GeV/c, rises to about 50% at a transverse momentum of $\sim$8 GeV/c, and typically plateaus at over 90% at $p_t \sim 10$ GeV/c, depending on the exact trigger conditions.

At Level 3, a computer farm is used to fully reconstruct the data, including three-dimensional track reconstruction in the CTC. However, the fast algorithm used for tracking is only efficient for particles with $p_t > 1.4$ GeV/c. In the third level of the trigger, more stringent electron and muon selection criteria, similar to those described in Subsec. 4.2, are applied. During Run I, about $7.5 \cdot 10^6$ electron trigger events and about $2.5 \cdot 10^6$ inclusive muon trigger events were recorded by CDF. Table 1 details the numbers of events recorded by the different trigger streams for the Run Ia and Run Ib data taking periods. The numbers of events do not necessarily scale with the integrated luminosities of Run Ia and Run Ib. This is due to different trigger thresholds and prescale factors, which accept only every second or third event triggered at high instantaneous luminosities, to prevent an increased deadtime.

Table 1. Numbers of events recorded by the different B physics trigger streams for the Run Ia and Run Ib data taking periods.

Trigger stream	Run Ia	Run Ib
Single electrons	$1.9 \cdot 10^6$	$5.7 \cdot 10^6$
Single muons	$4.1 \cdot 10^5$	$2.1 \cdot 10^6$
Dimuons		
$m_{\mu\mu} < 2.8$ GeV/c^2	$5.2 \cdot 10^5$	$8.0 \cdot 10^5$
2.8 GeV/$c^2 < m_{\mu\mu} < 3.4$ GeV/c^2	$2.2 \cdot 10^5$	$1.0 \cdot 10^6$
3.4 GeV/$c^2 < m_{\mu\mu} < 4.1$ GeV/c^2	$2.5 \cdot 10^5$	$7.4 \cdot 10^5$
8.5 GeV/$c^2 < m_{\mu\mu} < 11.3$ GeV/c^2	$8.1 \cdot 10^4$	$2.8 \cdot 10^5$
$m_{\mu\mu} > 4.0$ GeV/c^2	$5.1 \cdot 10^5$	$1.9 \cdot 10^6$
Electron–muons	$2.4 \cdot 10^5$	$5.0 \cdot 10^5$

As an example, Fig. 10(a) shows the transverse energy spectrum of electrons from the single electron triggers recorded in Run Ib. The trigger turn-on is visible at $E_t \sim 8$ GeV, followed by an exponentially falling energy spectrum. The shoulder around 40 GeV originates from a different physics process. These are electrons from W boson decays $W \to e\nu$, demonstrating how large the b cross section is compared to other physics processes like W production. The distribution in Fig. 10(a) is

obtained by identifying electrons with $E_t > 5$ GeV in single electron trigger events. The enhancement of electrons at 5 GeV below the trigger turn-on results from additional volunteer electrons in these events, which are not the trigger electrons. For comparison, Fig. 10(b) shows the p_t spectrum of inclusive single muons.

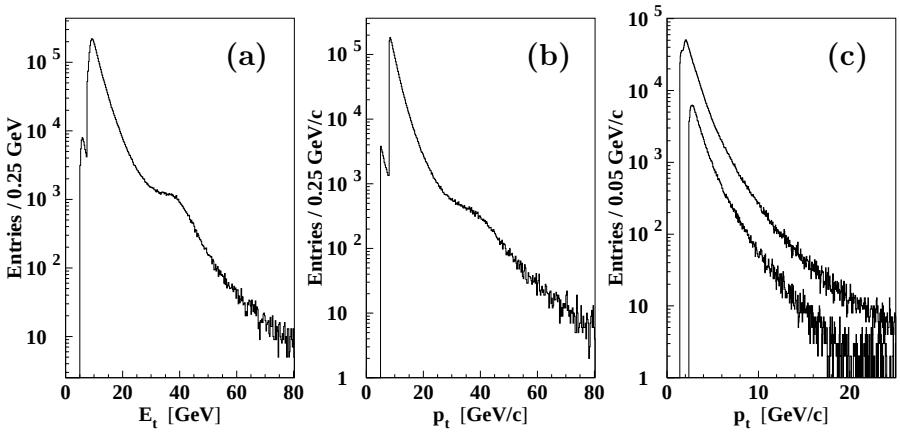

Fig. 10. Distribution of (a) transverse energy spectrum of inclusive single electrons and p_t spectrum of (b) inclusive single muons and (c) muons from dimuon trigger data. The upper curve in (c) represents Run Ib events while the lower distribution is obtained from Run Ia data.

4.1.2. *Dimuon trigger*

The collection of dimuon trigger data requires two muon candidates to be observed in the muon system at Level 1. The trigger efficiency for a muon at Level 1 rises from about 50% at $p_t = 1.6$ GeV/c to 90% at $p_t \sim 3.1$ GeV/c with a plateau of $\sim$95%. As an illustration of the trigger turn-on, Fig. 11(a) shows the Level 1 efficiency for CMU muons plotted versus $1/p_t$ using $J/\psi \to \mu\mu$ and $Z^0 \to \mu\mu$ data. The range-out at low momenta is predicted to occur for $p_t < 1.4$ GeV/c. The second level trigger requires that at least one of the muon tracks be matched in φ to a track found by the CFT. The efficiency for finding a track with the CFT rises from 50% at p_t of about 1.9 (2.6) GeV/c to 90% at $p_t \sim 2.2$ (3.1) GeV/c and reaches a plateau of $\sim$94% (93%). The numbers given in brackets refer to the Run Ia settings where the dimuon trigger was operated with a slightly higher momentum threshold. Figure 11(b) shows the Level 2 efficiency for CMU muons plotted versus $1/p_t$ again using $J/\psi \to \mu\mu$ and $Z^0 \to \mu\mu$ data. The Level 2 efficiency is displayed for positive and negative muons separately, indicating no charge dependence of the L2 trigger turn-on.

At Level 3, the events are again fully reconstructed, requiring two CTC tracks to be matched with two tracks in the muon chambers. For offline reconstruction the dimuon data are split into different samples, according to the dimuon invariant mass, as detailed in Table 1, which again shows the numbers of events separately for the Run Ia and Run Ib data taking periods. The data with $2.8 < m_{\mu\mu} <$

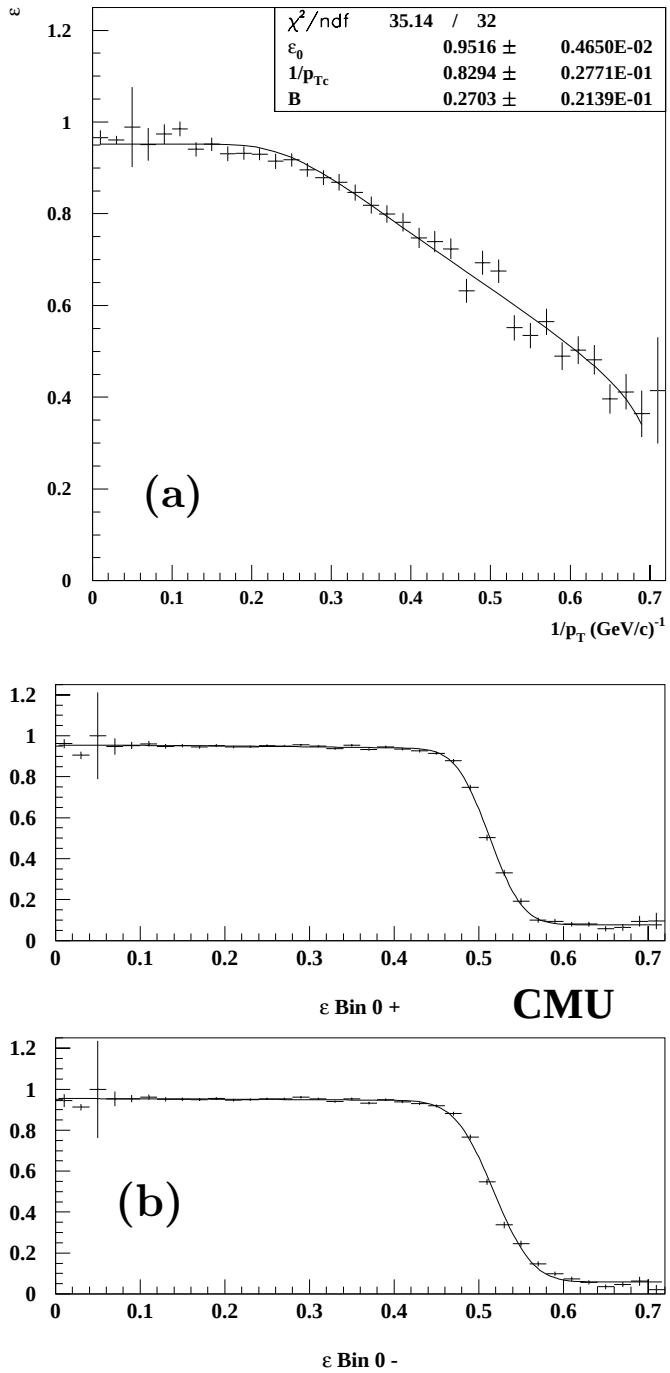

Fig. 11. (a) Level 1 and (b) Level 2 trigger turn-on efficiency for CMU muons plotted versus $1/p_t$ using $J/\psi \to \mu\mu$ and $Z^0 \to \mu\mu$ data. The Level 2 efficiency is displayed for positive (top) and negative (bottom) muons separately.

3.4 GeV/c^2 are the source of CDF's $J/\psi \to \mu^+\mu^-$ events, while the data with $3.4 < m_{\mu\mu} < 4.1$ GeV/c^2 contain $\psi(2S) \to \mu^+\mu^-$ events. Dimuon decays of the Υ resonances are contained in the sample with $8.5 < m_{\mu\mu} < 11.3$ GeV/c^2. Events with $m_{\mu\mu} < 2.8$ GeV/c^2 are a source of double-semileptonic decays $b \to c\,\mu X$ followed by $c \to \mu X$, while the high-mass dimuon stream with $m_{\mu\mu} > 4.0$ GeV/c^2 provides events where the two muons originate from the decay of a b and $\bar{b}$ quark.

As a further illustration, Fig. 10(c) shows the p_t spectrum of muons from the dimuon trigger data. The upper curve in Fig. 10(c) represents Run Ib events, while the lower distribution is obtained from Run Ia data. The higher muon momentum threshold in Run Ia is clearly visible and the trigger turn-on is softer compared to the single muon events [see Fig. 10(b)].

4.1.3. *Electron–muon trigger*

CDF also triggered on events containing an electron and a muon. The trigger is a combination of the single electron and muon triggers. This sample has a principal electron E_t threshold of about 5 GeV and a principal muon p_t threshold of about 3.0 GeV/c for Run Ia data and ~ 2.5 GeV/c for Run Ib. Because of the higher lepton threshold, the $e\mu$ data constitute a significantly smaller dataset compared to the dimuon data, as shown in Table 1.

4.2. *Lepton identification*

4.2.1. *Electron identification*

The identification of electron candidates reconstructed after data collection uses information from both the calorimeters and the tracking chambers. Here, we describe typical selection criteria used for electron identification at CDF. The longitudinal shower profile must be consistent with an electron shower with a leakage energy from the CEM into the CHA of less than 4%, if one track is pointing to the calorimeter tower, or less than 10% if more than one track is pointing to the calorimeter tower. The lateral shower profile of the CEM cluster has to be consistent with that from test beam electrons. Additionally, a χ^2 comparison of the CES shower profile with that of test beam electrons has to result in $\chi^2 < 10$. For the association of a single high p_t track with the calorimeter shower, based on the position matching at the CES plane, it is required that $r|\Delta\varphi| < 1.5$ cm and $|\Delta z \sin\theta| < 3$ cm. In addition, we demand the E_t of the electron candidate, reconstructed offline, to be greater than 6 GeV (5 GeV) for single electron ($e\mu$) data. Usually electron candidates from photon conversion are removed from the analysis by looking for oppositely charged tracks which have a small opening angle with the electron candidate.

4.2.2. *Muon identification*

The typical reconstruction of muon candidates at CDF is very similar for the single muon and dimuon datasets. Usually, a χ^2 characterizing the separation between the

track segment in the muon chamber and the extrapolated CTC track is computed, where the uncertainty in this χ^2 variable is dominated by the multiple scattering in the detector material. Typical selection requirements are $\chi^2 < 9$ in the $r\varphi$ view (CMU, CMP and CMX) and $\chi^2 < 12$ in the rz view (CMU and CMX). A minimum energy deposition of 0.5 GeV in the hadron calorimeter is required for a muon candidate, as expected for a minimum ionizing track. The transverse muon momentum reconstructed offline is usually required to be greater than 7.5 GeV/c for inclusive muons. For the dimuon sample, this cut is typically placed at $p_t > 2$ GeV/c for each muon candidate.

4.3. *Charged particle selection*

Charged particles are identified as tracks in CDF's central tracking chamber. To ensure a good track reconstruction, quality cuts requiring a minimum number of hits in the CTC are usually imposed. Typical requirements are at least five hits in two or more CTC axial superlayers and at least two hits in more than one CTC stereo superlayer. In addition, tracks are often required to be reconstructed in the SVX with hits in at least three out of the four silicon layers. In many analyses, a χ^2 is calculated and defined as the increase in the track fit χ^2, when the SVX hits are included in the CTC track fit. This χ^2 divided by the number of SVX hits usually has to be less than six to reject badly measured tracks. The track quality requirements are generally applied to hadrons as well as leptons. For optimal vertex resolution, hadron and lepton candidate tracks are often required to be reconstructed in the SVX detector.

4.3.1. *Hadron selection*

Usually, all reconstructed tracks are assigned the desired particle hypotheses, due to the lack of a sophisticated particle identification at CDF. Applying cuts on the tracks transverse momenta are often the only means of reducing combinatorial background. The minimum p_t cut on tracks is usually set at 0.4 GeV/c. However, the specific ionization information dE/dx from the CTC provides a π/K separation of about one σ for tracks with p_t greater than about 1.2 GeV/c. Therefore, dE/dx information from the CTC is sometimes used to help identify hadrons. Because of the large Landau tail of the ionization distribution, the 80% truncated mean of the measured charges from the CTC sense wires is taken as the best estimator of the track dE/dx. The probabilities, $P(i)$, for a track to be consistent with the $i = e$, μ, π, K or p hypotheses are then calculated using the measured dE/dx value and the predictions for the assumed particle hypotheses. A likelihood ratio, $\ell h^K_{dE/dx}$, for a track being, for example, a kaon is defined to be the ratio of $P(K)$ divided by the sum of the probabilities of all particle hypotheses. Usually, this likelihood ratio is required to be greater than 0.01.

The kinematic selection criteria used in a particular analysis are often optimized by maximizing the quantity $N_S/\sqrt{N_S + N_B}$, where N_S is the predicted number of

signal events based on Monte Carlo calculations (see Subsec. 4.5) and N_B is the observed number of background events estimated, for example, from the signals sideband regions.

4.4. *Jet reconstruction*

Some analyses require the reconstruction of jets which are usually formed from charged particles in B physics analyses, rather than from the more commonly used calorimeter clusters. A jet in a B event is often of low momentum and its energy is therefore not very precisely measured in the calorimeter. In addition, there is a difference between jets associated with electrons compared to jets containing a muon, since electrons deposit much more energy in the calorimeter than muons. If calorimeter clusters were used to find jets, electrons would be associated with jets much more often than muons for any minimum jet energy requirement. Therefore, jets are formed in B physics analyses from tracks using a cone-clustering algorithm. Usually, tracks with $p_t > 1.0$ GeV/c are used as jet seeds. If two seeds are within a cone with radius $\Delta R = \sqrt{(\Delta\eta)^2 + (\Delta\varphi)^2} < 0.7$, the momenta of the seeds are added together to form a new seed. After all possible seed merging, lower momentum tracks (usually $0.4 < p_t < 1.0$ GeV/c) that are within $\Delta R < 0.7$ of a seed are added to form the final jet. A jet can, in principle, consist of a single track with $p_t > 1$ GeV/c.

4.5. *Simulation of heavy flavor production and decay*

Monte Carlo (MC) generation programs are used to simulate heavy flavor production in $p\bar{p}$ interactions. These programs are supplemented by phenomenological models of hadronization and decays of unstable particles. They are usually used in conjunction with programs that simulate the detector response to the final state particles. MC programs are necessary tools for calculating the geometrical and kinematic acceptance for observing heavy flavor events and are also used to estimate backgrounds for particular analyses. While considerable effort has gone into developing and tuning simulations for e^+e^- collisions, the state of the art is somewhat less well developed for the more complex high energy hadron–hadron collisions.

At CDF, two types of Monte Carlo simulations are used. Calculations depending only on the production and decay of B hadrons employ a Monte Carlo generator that simulates only a single B hadron and its decay products. Situations which depend on the fragmentation particles resulting from the hadronization of the b quark, as well as the "underlying event" particles from the $p\bar{p}$ scattering, use a full event generator like the PYTHIA program package.[28] In the following, we describe both Monte Carlo generators as well as the CDF detector simulation.

4.5.1. *Simulation of a single B hadron*

The simulation of a single B hadron begins with a model of b quark production based on an NLO QCD calculation.[20] This calculation employs the MRSD0 parton

distribution function[13] with $m_b = 4.75$ GeV, $\Lambda = 215$ MeV, and a renormalization scale of $\mu = \mu_0 = \sqrt{p_t^2 + m_b^2}$ to model the kinematics of the initial state partons. Usually, b quarks are generated in the rapidity interval $|y_b| < 1.0$ with a minimum p_t for the b quark chosen in a way to avoid any biases in the B meson kinematic distributions after the application of the kinematic cuts used in an analysis. The b quarks are then fragmented into B hadrons, with no additional hadronization products, according to a model using the Peterson fragmentation function[22] with a Peterson parameter of $\epsilon_b = 0.006$ (see Subsec. 2.3). The bottom and charm hadrons are decayed into the various final states using branching ratios and decay kinematics governed by the world average masses and lifetimes of the involved particles.[3] The decay of bottom hadrons is accomplished using the QQ program[29] developed by the CLEO collaboration, extended to include B_S^0 mesons and b baryons.

4.5.2. *Monte Carlo simulation of the whole event using PYTHIA*

The PYTHIA Monte Carlo generator[28] is used in instances where more than just a single decaying B meson is required. PYTHIA simulates a complete $p\bar{p}$ interaction: the $b\bar{b}$ pair, the hadronization products, and the remaining beam fragments from the $p\bar{p}$ scattering ("underlying event"). PYTHIA exploits an improved string fragmentation model tuned to experimental data, mostly from high energy e^+e^- collisions. PYTHIA generation at CDF uses most of the typical default parameters including the CTEQ2L[30] parton distribution functions. The b quarks are again fragmented using the Peterson fragmentation model.[22] However, the actual B decay performed by PYTHIA is suppressed and, instead, the QQ program[29] is invoked.

The PYTHIA generator is controlled by a series of parameters whose default values are adjusted to achieve good agreement with primarily high energy e^+e^- data. Discrepancies between the "default" PYTHIA and CDF $p\bar{p}$ data are apparent, especially when one is considering particle production that does not originate from the b hadronization but from the "underlying event." The fidelity of the "default" PYTHIA generator is studied by comparing generated semileptonic $B \to D\ell X$ Monte Carlo data after detector simulation to real CDF data. This comparison studied track multiplicities in ΔR and $\Delta\varphi$ intervals around the $B \to D\ell$ direction and found the data to have a higher multiplicity of underlying event tracks than PYTHIA predicts. A good description of the charged particle multiplicities and p_t distributions is obtained by adjusting several PYTHIA parameters. The properties of multiple interactions and beam remnants are controlled primarily through the multiple interaction cross section [PARP(31)], the model for their generation [MSTP(82)], the ratio of gg and $q\bar{q}$ multiple interactions [PARP(85,86)], and the width of the Gaussian p_T spread of particles produced in the breakup of color strings [PARJ(21)]. Once these parameters are adjusted to obtain agreement with the data away from the b jets, it is assumed that the underlying event is well modeled. In addition, the Peterson parameter PARJ(55) is modified so that the generated multiplicity of tracks inside a cone of $|\Delta R| < 1$ around the b quark matches the observed

one. Table 2 lists the default and tuned values of the relevant PYTHIA parameters. More details of the tuning procedure may be found in Ref. 31.

Table 2. The PYTHIA Monte Carlo parameters modified from their defaults to agree with $B \to D\ell X$ data at CDF.

Parameter	Default	Tuned	Description
MSTP(82)	1	3	model of multiple interactions
PARP(85)	0.33	1.0	fraction of color-connected gg multiple interactions
PARP(86)	0.66	1.0	total fraction of gg multiple interactions
MSTP(33)	No	Yes	multiply cross sections by PARP(31)
PARP(31)	1.00	1.66	increase cross sections by 66%
PARJ(21)	0.36	0.6	$\sigma^{\text{frag}}(p_t)$
MSTJ(11)	4	3	use Peterson fragmentation for b, c
PARJ(55)	0.006	0.0063	Peterson fragmentation parameter ϵ_b

4.5.3. *Detector simulation*

The output of the MC generation is often simply passed through the standard fast simulation of the CDF detector which is based on parametrizations and simple models of the detector response determined from data or test beam measurements. The detector response is often parametrized as a function of the particle kinematics. The inclusive lepton or dilepton trigger usually introduces a strong kinematic bias on an analysis. This bias must be well modeled in the MC simulation to obtain the proper relative reconstruction efficiencies. Often, an empirical approach is taken rather than simulating the trigger directly. The trigger is either modeled by a simple parametrization of the CFT trigger, depending on the lepton p_t, or by an error function parametrization of the ratio of the observed lepton p_t distribution in the data compared to that generated by the simulation. For example, the efficiency parametrization of the single electron trigger follows the functional form

$$A \cdot \text{freq}\left(\frac{p_t - B_1}{C_1}\right) \cdot \text{freq}\left(\frac{p_t - B_2}{C_2}\right), \tag{7}$$

where $A = 0.927$, $B_1 = 6.18$ GeV/c, $C_1 = 4.20$, $B_2 = 7.48$ GeV/c, $C_2 = 0.504$, and freq is the normal frequency function. After the simulation of the CDF detector, the same selection criteria applied to the data are usually imposed on the Monte Carlo events.

5. Features of B Physics at a Hadron Collider: A Brief Tour

In this section, we highlight some of the features of B physics at a hadron collider. We also make an attempt to describe, in an illustrative way, how CDF studies B decays. We will emphasize some of the tools used to find B decay products in hadronic collisions, omitting technical details which may be found later.

To set the stage, we first compare current producers of B hadrons. Table 3 summarizes some of the important features of B physics experiments and the accelerators at which they operate. There are three main approaches to producing B hadrons. First, $e^+e^- \to \Upsilon(4S) \to B\bar{B}$ at the CLEO experiment, located at the CESR storage ring at Cornell and the DORIS storage ring at DESY, where the ARGUS experiment operated until 1993. Second, $e^+e^- \to Z^0 \to b\bar{b}$ at the four experiments ALEPH, DELPHI, L3 and OPAL, located at the LEP storage ring at CERN, as well as the SLD detector at the SLC Collider at SLAC. Finally, $p\bar{p} \to b\bar{b}X$ at the Tevatron, where the CDF and DØ detectors are operated. As discussed earlier, the main motivation for studying B physics at a hadron collider is the large b quark cross section (see Table 3).

Table 3. Comparison of important features of different experiments studying B physics.

	$e^+e^- \to \Upsilon(4S) \to B\bar{B}$	$e^+e^- \to Z^0 \to b\bar{b}$	$p\bar{p} \to b\bar{b}X$
Accelerator	CESR, DORIS	LEP, SLC	Tevatron
Detector	ARGUS, CLEO	ALEPH, DELPHI L3, OPAL, SLD	CDF, DØ
$\sigma(b\bar{b})$	$\sim$1 nb	$\sim$6 nb	$\sim$50 μb
$\sigma(b\bar{b}) : \sigma(\text{had})$	0.26	0.22	$\sim$0.001
B^0, B^+	yes	yes	yes
B_S^0, B_c^+, Λ_b^0	no	yes	yes
Boost $\langle\beta\gamma\rangle$	0.06	6	$\sim$ 2–4
$b\bar{b}$ production	both B at rest	$b\bar{b}$ back-to-back	$b\bar{b}$ not back-to-back
Multiple events	no	no	yes
Trigger	inclusive	inclusive	leptons only

Figure 12 shows examples of typical B events at the $\Upsilon(4S)$ recorded with the ARGUS detector (left) and the CLEO experiment (right). At the $\Upsilon(4S)$ resonance, only $B^0\bar{B}^0$ or B^+B^- pairs are produced nearly at rest, resulting in a spherical event shape with an average charged particle multiplicity of about ten tracks. At the LEP or SLC accelerators, $b\bar{b}$ quark pairs are produced from the decay of the Z^0 boson where both quarks share half of the energy of the Z^0 resonance of 91.2 GeV. This results in two b jets being back-to-back as seen in Fig. 13, where examples from the OPAL (left) and SLD (right) experiments are displayed. The average boost of B hadrons at the Z^0 resonance is $\beta\gamma \sim 6$.

Figure 14 represents a typical B event from the Tevatron, shown on the left hand side in the $r\varphi$ view of the CDF central drift chamber. No well-defined jet structure is visible; the average multiplicity is about 40 charged tracks, including tracks from the "underlying event" particles. It might appear challenging to find the B decay products in this quite messy environment of a hadronic collision. One way to extract B decays in a $p\bar{p}$ collision is illustrated on the right hand side of Fig. 14. The relatively long lifetime of a B hadron and a particle boost of about $\beta\gamma \sim 2$–4, depending on the trigger which recorded the event, results in a B decay

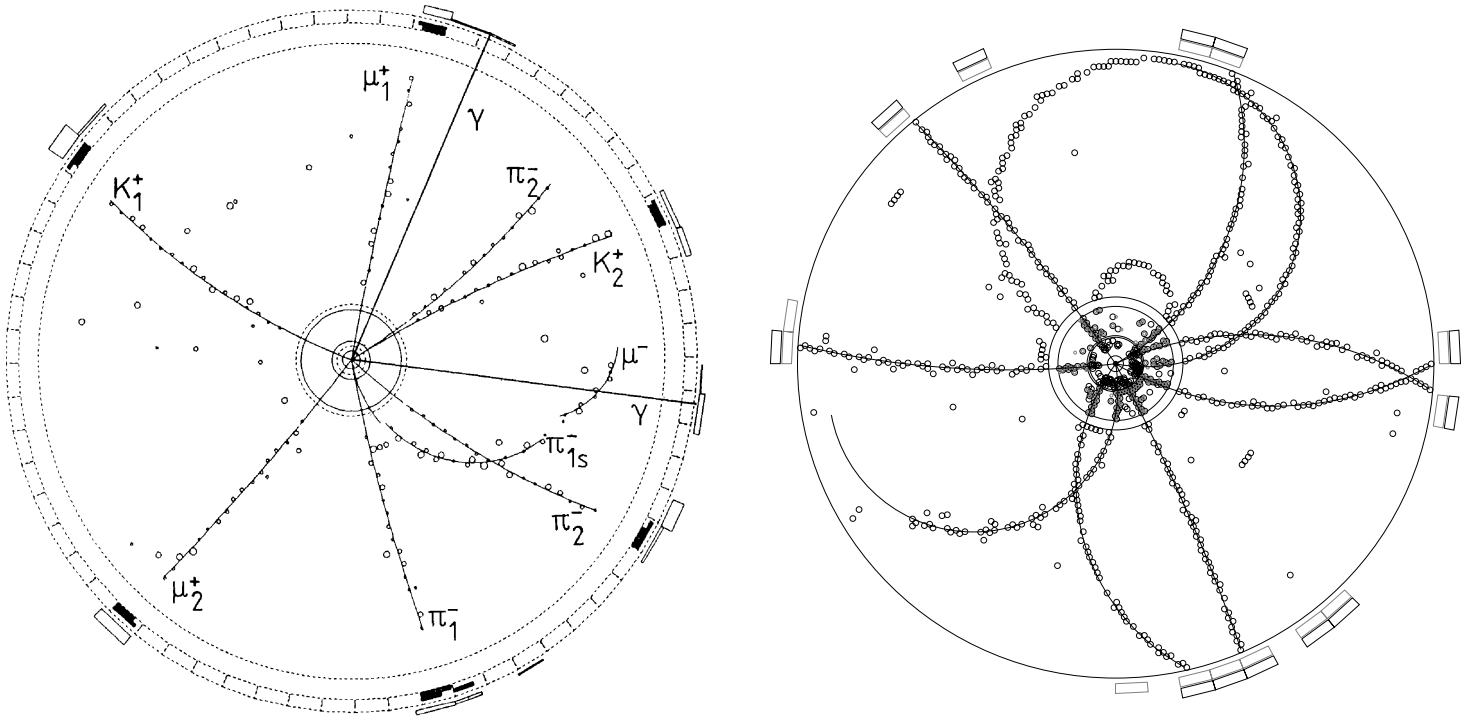

Fig. 12. A typical B event at the $\Upsilon(4S)$ in the $r\varphi$ view from the ARGUS experiment (left) and the CLEO detector (right).

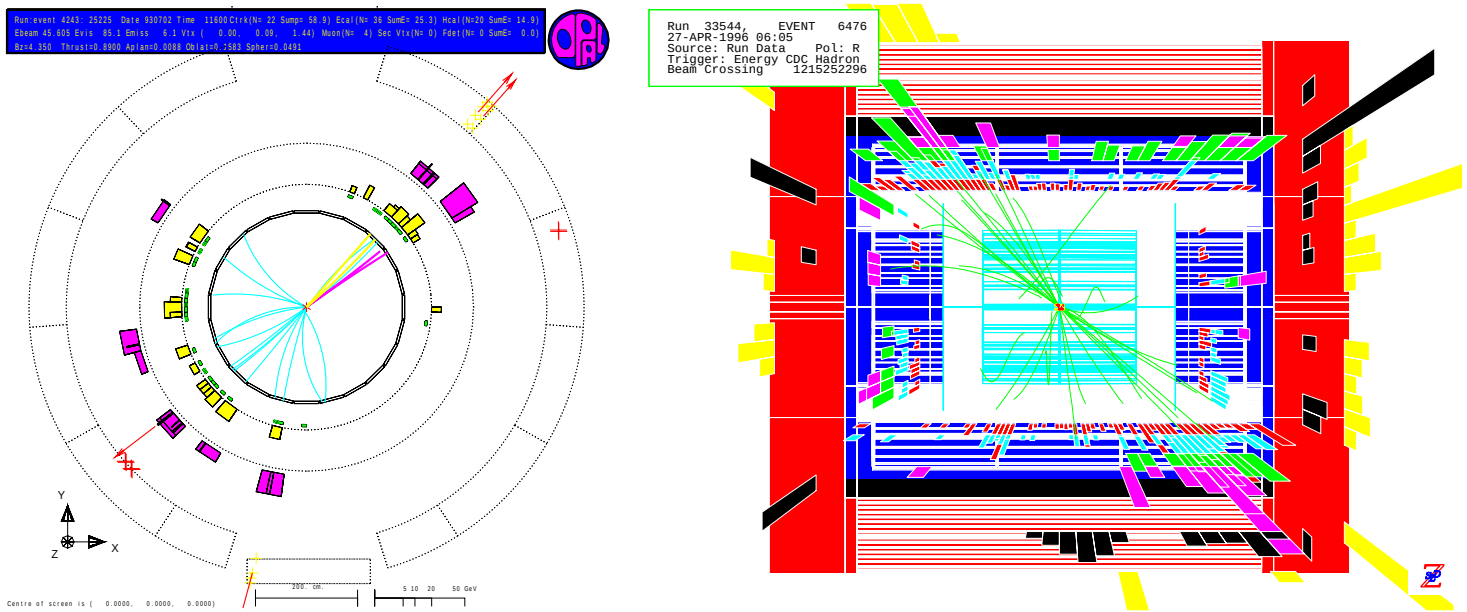

Fig. 13. A typical B event at the Z^0 pole recorded with the OPAL detector (left) in the $r\varphi$ view and the SLD experiment (right) in the rz view.

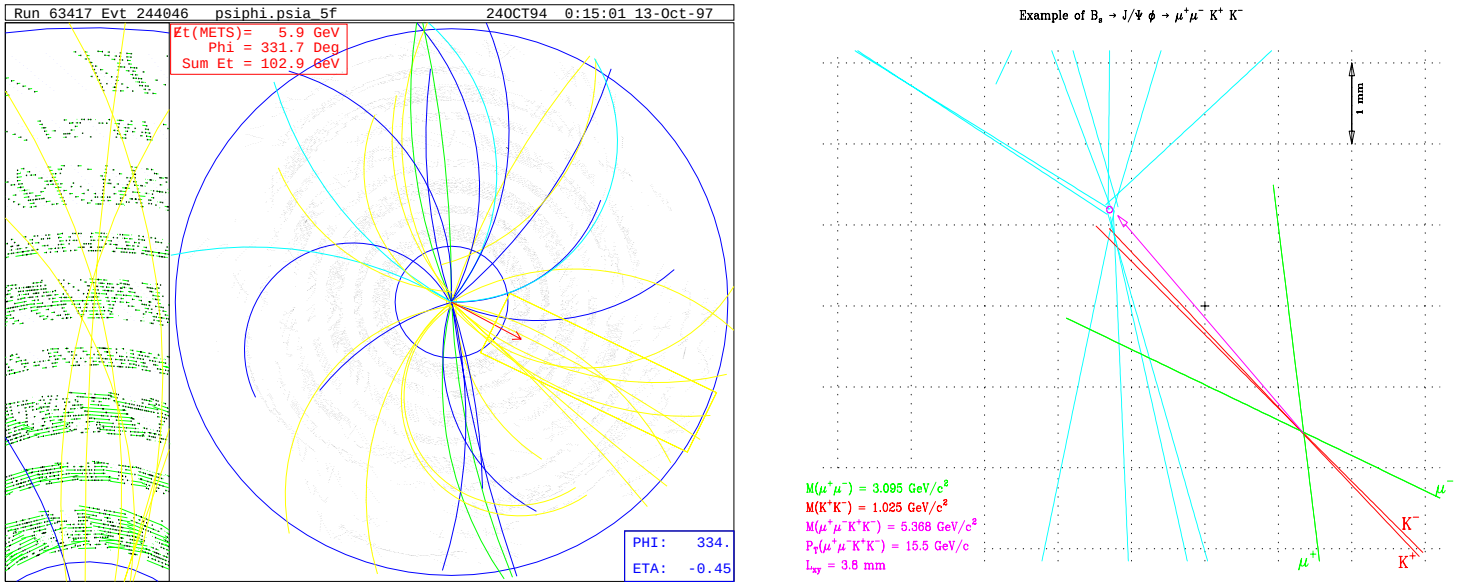

Fig. 14. A typical B event at the Tevatron recorded with the CDF detector (left). On the right hand side, the decay vertex of a $B_S^0 \to J/\psi\phi$ decay with $J/\psi \to \mu^+\mu^-$ and $\phi \to K^+K^-$ is clearly separated from the primary interaction vertex.

vertex which is clearly separated from the primary $p\bar{p}$ interaction vertex. In the example shown on the right hand side of Fig. 14, the decay vertex of a $B_S^0 \to J/\psi\phi$ decay with $J/\psi \to \mu^+\mu^-$ and $\phi \to K^+K^-$ is clearly visible and about 3.8 mm separated from the primary interaction vertex.

In the following, we give a few more examples of how B decays are studied at CDF and which essential tools are used for B physics in hadron collisions. In Subsec. 4.1, we already pointed out the importance of the trigger to select events containing B hadrons. Another important feature for B physics at a hadron collider is the good tracking capability, such as that at CDF. The central tracking chamber together with the SVX provide excellent track momentum resolution which translates into an excellent invariant mass resolution, as illustrated in Fig. 15. Here, the dimuon invariant mass is displayed for muons from the dimuon trigger stream. A prominent J/ψ peak is visible with about $(243,000 \pm 540)$ J/ψ signal candidates from the Run I data on low background. For this distribution, where both muons are reconstructed in the SVX, the mass resolution of the J/ψ peak is about 16 MeV/c^2.

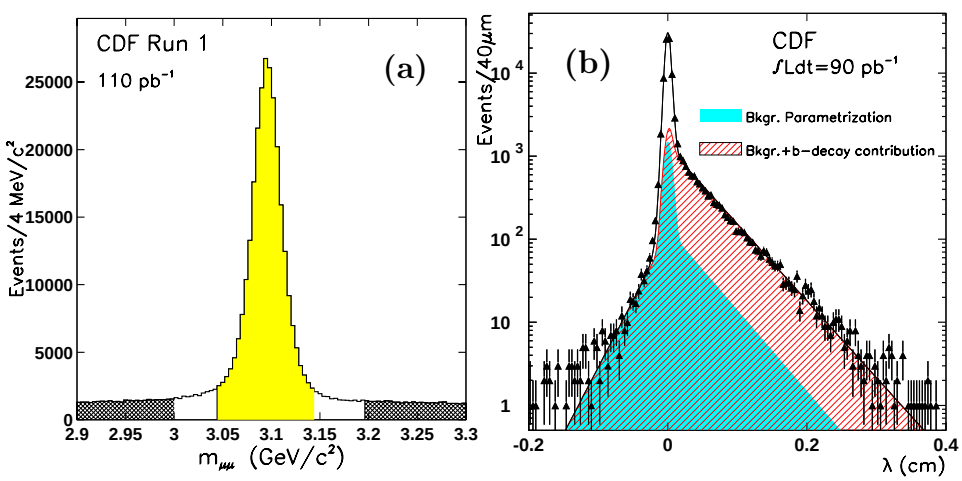

Fig. 15. (a) Invariant mass distribution of oppositely charged muon pairs from the CDF dimuon trigger. (b) Decay length distribution of the signal events indicated as a shaded area in (a) with the result of a fit superimposed (see text).

In addition to excellent tracking, superb vertexing is the other essential feature of successful B physics studies at a hadron collider. This is demonstrated in Fig. 15(b), where the two muons of the J/ψ signal candidates [light-shaded area in Fig. 15(a)] are vertexed using tracking information from the SVX. The two-dimensional distance between the primary $p\bar{p}$ interaction vertex and the reconstructed dimuon vertex is plotted. This distribution shows several features: a prominent peak at zero decay length results from prompt J/ψ candidates which are produced at the primary interaction vertex and constitute about 80% of all J/ψ candidates. The width of this peak reveals information about the vertexing resolution, which is on

average 40–50 μm, for this sample. At positive decay lengths, J/ψ mesons from B hadron decays are described by an exponential slope. At a distance of about 100 μm from the primary interaction vertex, mainly J/ψ's from B decays remain. There is also a small exponential slope at negative decay lengths where the particle seems to decay, before the point where it is produced. These events result from the combinatorial background underneath the J/ψ signal. This is indicated by events from the J/ψ sidebands [dark-shaded regions in Fig. 15(a)] which describe well the distribution at negative decay lengths as seen by the dark-shaded area in Fig. 15(b).

In order to fully reconstruct B mesons, for example through the decay $B^+ \to J/\psi K^+$, the J/ψ candidates from the signal region of Fig. 15(a) are paired with another track in the event, assumed to be a kaon. A $J/\psi K^+$ invariant mass distribution, such as the one in Fig. 16(a), is observed with a B^+ signal on a large background. This background can be drastically reduced if a displaced B vertex is required. This is demonstrated in Fig. 16(b) with a cut on the B decay length of greater than 100 μm. A clear B signal can now be found on a small background.

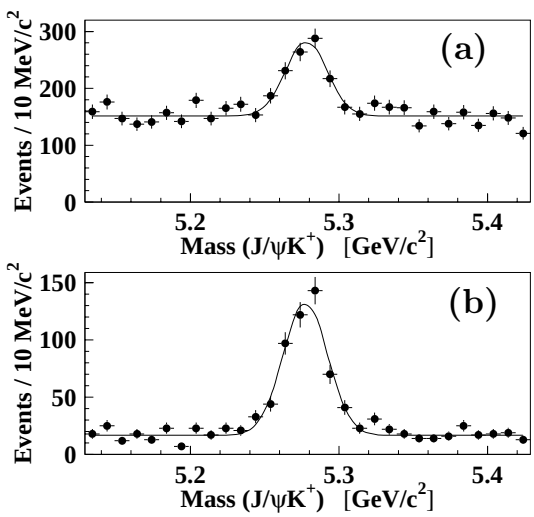

Fig. 16. Invariant mass distribution of reconstructed $B^+ \to J/\psi K^+$ candidates with $J/\psi \to \mu^+\mu^-$ (a) without a requirement on the B decay length and (b) with a cut on the B decay length of greater than 100 μm.

Another tool in separating B decays in hadronic collisions can be obtained from the fact that B decays are often isolated. This means that there is usually not much track activity in the vicinity of a B hadron decay as illustrated in Fig. 17(a). This fact can be exploited by a track-based isolation quantity I. It is typically defined as the p_t of the reconstructed B candidate divided by the scalar sum of the transverse momenta of all tracks within a cone in $\eta\varphi$ space around the B candidate direction, including the tracks from the B decay. A typical cone radius is $\Delta R < 1$ and a typical cut value requires more than 50% of all momentum within the cone to be carried

by the B candidate. The effect of the isolation cut is demonstrated in Fig. 17(b) on a $\phi \to K^+K^-$ signal from a $B_S^0 \to D_S^- \mu^+ \nu$ decay with $D_S^- \to \phi\mu^-\bar{\nu}$. The upper distribution shows the K^+K^- invariant mass before a cut on $I > 0.5$ is applied to obtain the lower distribution. The combinatorial background is drastically reduced with a high efficiency on the ϕ signal. Finally, the significantly harder momentum spectrum of particles from b hadrons, compared to light hadrons, can be used to place high p_t cuts of several GeV/c on B candidates. This also results in a strong reduction of combinatorial background from light quark jet production.

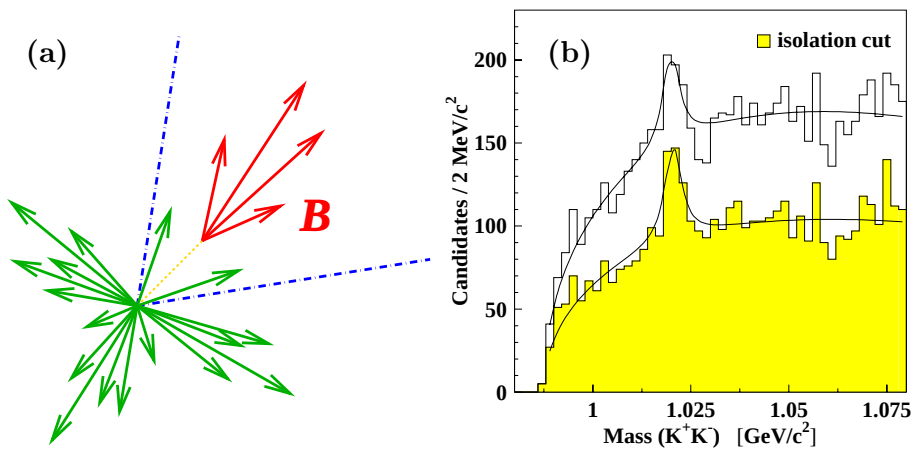

Fig. 17. (a) Illustration of the isolation of B mesons in hadronic collisions. (b) Invariant K^+K^- mass distribution from $B_S^0 \to D_S^- \mu^+ \nu$ decays with $D_S^- \to \phi\mu^-\bar{\nu}$. The upper distribution shows the K^+K^- invariant mass before an isolation requirement is applied resulting in the shaded K^+K^- mass distribution.

To summarize, the essential features to extract B hadron decays in hadronic collisions at CDF are excellent tracking in the CTC and SVX, the superb vertexing capabilities of CDF's silicon vertex detector exploiting the long lifetimes of B hadrons by requiring decay vertices to be displaced from the primary interaction vertex, the harder momentum spectrum of particles from b hadrons, and the fact that B mesons are often isolated.

6. Measurements of B Hadron Lifetimes

CDF has measured the lifetimes of all weakly decaying B mesons (B^0, B^+, B_S^0 and B_c^+) as well as the lifetime of the Λ_b^0 baryon. In this section, we discuss the B lifetime measurements at CDF. After a short introduction to the theory of B lifetimes, we describe experimental techniques of B lifetime measurements, including the determination of the primary $p\bar{p}$ interaction vertex, the measurement of the B hadron decay length, and a description of the fitting procedure. We then review the lifetime measurements of the individual B species at CDF, emphasizing crucial aspects of a particular measurement rather than describing an analysis in detail.

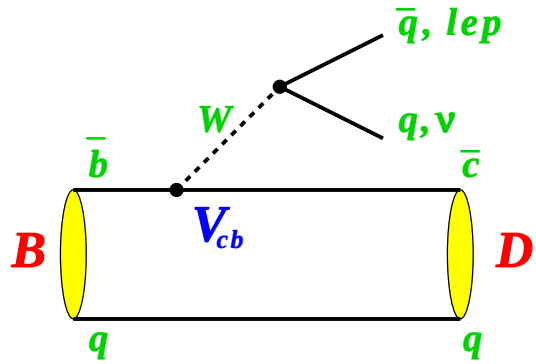

Fig. 18. Sketch of the spectator model of a B hadron decay.

6.1. *Introduction to B hadron lifetimes*

The lifetimes of B hadrons are fundamental properties of these particles and are often needed to determine other Standard Model[4] quantities, like the CKM matrix element $|V_{cb}|$, or to measure the time dependence of $B\bar{B}$ oscillations. In the simple spectator model of a B hadron decay, where the b quark decays into a c quark emitting a W boson which couples to a $\ell\nu$ or $q\bar{q}$ pair, as illustrated in Fig. 18, the $\bar{q}$ quark within the B hadron only acts as a spectator and the b quark decays as a free particle. In this case, the B hadron lifetime would be given in analogy to the muon lifetime as

$$\Gamma = \frac{1}{\tau} = \frac{G_F^2 m_b^5}{192\pi^3} \cdot |V_{cb}|^2 \cdot \mathcal{F}\,, \tag{8}$$

where $\mathcal{F}$ is a phase space factor. Here, we have neglected $b \to u$ transitions resulting in a term with $|V_{ub}|^2$ which is small. In the spectator model, all hadrons containing a b quark would have the same lifetime. However, this picture does not hold for the prediction of charm hadron lifetimes which are measured[3] to be

$$\tau(D^-) \sim 2.5\tau(D^0) \sim 2.5\tau(D_S^-) \sim 5.0\tau(\Lambda_c^-)\,. \tag{9}$$

Possible causes of these lifetime differences originate from nonspectator effects, playing an important role in the decay of charm hadrons. These nonspectator decays include contributions like the W exchange process for neutral B mesons, shown in Fig. 19(a), or the B^+ annihilation diagram displayed in Fig. 19(b). Other nonspectator mechanisms are caused by so-called final state Pauli interference effects. An example is shown in Fig. 19 for the decay $B^+ \to \bar{D}^0\pi^+$, which can occur through a so-called external W emission [Fig. 19(c)] or a so-called internal W emission [Fig. 19(d)]. There is a destructive interference between the two diagrams which causes the B^+ decay width to be smaller than the B^0 width. This is one of the reasons the B^+ lifetime is predicted to be larger than the B^0 lifetime. Measurements of the lifetimes of individual B hadron species can therefore probe B decay

mechanisms beyond the simple spectator model decay picture. However, among bottom hadrons, the lifetime differences are expected to be smaller than in the charm system due to the heavier bottom quark mass.

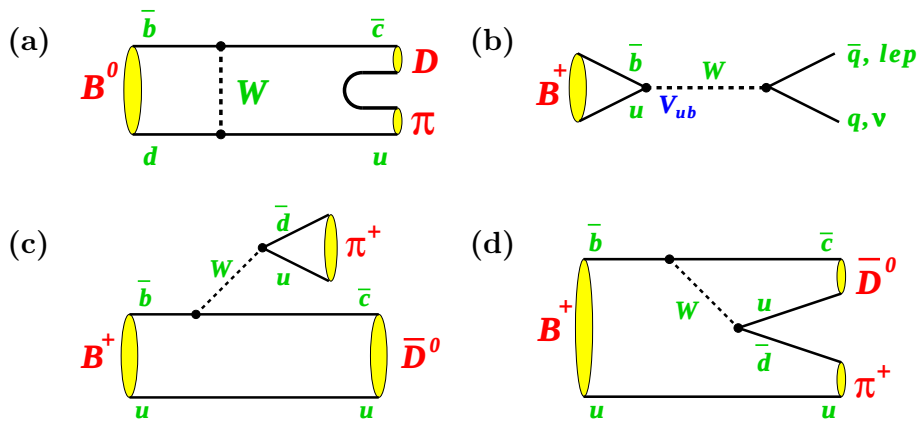

Fig. 19. Illustration of (a) W exchange process, (b) B^+ annihilation diagram as well as final state interference through (c) external W emission and (d) internal W emission.

In the past few years, the heavy quark expansion technique has been applied extensively to the calculations of inclusive decay rates of heavy hadrons, for both spectator and nonspectator decays. It provides quantitative predictions for lifetime differences among the heavy hadrons. It is generally believed that a lifetime difference of order 5–10% should exist between the B^+ and the B^0 meson. Reference 32 predicts that the B^+ meson lifetime should be longer than the B^0 meson lifetime by about 5%. However, Ref. 33 questions some assumptions made in Ref. 32 and states that the sign of the deviation from unity cannot be predicted reliably. There is agreement that the models expect a much smaller difference, of less than about 1%, between the B^0 and B_S^0 lifetimes.

Since this subject seems to be controversial, it might be best solved by precisely measuring all the B hadron lifetimes. Several direct measurements of B^+ and B^0 meson lifetimes have been performed by e^+e^- experiments (see Ref. 3 for an overview) and by CDF. The precision of current measurements now approaches the level where the predicted small differences can be seen and improvements in these measurements will provide a strong test of B hadron decay mechanisms.

6.2. *Experimental techniques*

In general, two experimental methods have been employed to measure B hadron lifetimes. The first is based on the signed track impact parameter, the distance of closest approach of the track trajectory extrapolated to the B hadron production point. The average impact parameter is proportional to the lifetime of the B hadron. The advantage of using the impact parameter is that it is fairly insensitive to

the boost of the B hadron: a B hadron with a large Lorentz boost will travel further, but the decay products will come out at a smaller angle, leaving the impact parameter unchanged. To extract the B hadron lifetime, a Monte Carlo model is used to reproduce the observed impact parameter distribution as a function of the B lifetime. Impact parameter measurements typically use leptons from semileptonic B decays. In fact, the first measurement of a b lifetime[34] used the signed impact parameter of leptons.

The second method for measuring B hadron lifetimes is based on the decay length, which is the distance from the B hadron production point to the B hadron decay point. The decay length L is related to the proper decay time t in the B rest frame by the Lorentz boost $\beta\gamma$ as $L = \beta\gamma ct$. Unlike the impact parameter method, it is necessary to know the boost value. In the case of a fully reconstructed B hadron decay, its boost value is determined as $\beta\gamma = p_B/m_B$, where p_B is the B hadron momentum and m_B is the B hadron mass. If the B hadron is only partially reconstructed, the boost value must be inferred using a Monte Carlo model.

All B hadron lifetime results at CDF are based on the decay length measurement using fully reconstructed B hadrons as well as partially reconstructed B decays, which usually comprise higher statistics samples. In the following, we give an overview of how B lifetimes are measured at CDF, using the more complicated example of a partially reconstructed B decay. We first describe the Tevatron beam profile and the determination of the B hadron production point, the primary event vertex. Then, the B hadron decay length reconstruction using CDF's silicon vertex detector is the subject of Subsec. 6.2.3, while Subsec. 6.2.4 gives a description of the lifetime fit procedure used to extract the B hadron lifetime from the measured decay length.

6.2.1. *Tevatron $p\bar{p}$ beam profile*

With a proton and antiproton bunch length of about 0.4 m, the primary $p\bar{p}$ interaction vertices are distributed along the beam direction according to approximately a Gaussian function, with a width of $\sim$30 cm, as shown in Fig. 20(a). Near the interaction region, the p and $\bar{p}$ beams follow straight lines but could have an offset and slope with respect to the z axis of the tracking detectors. The profile of the beam for a typical data acquisition run is shown in Fig. 20(b). The deviation of reconstructed primary vertices from the calculated average beam position is plotted in the transverse plane. To ensure that the spread of the beam, instead of the resolution of the vertex fit, is the dominant contribution to the width of the observed distribution, only vertices with high track multiplicities are used. The upper two plots show the two-dimensional distribution of the beam spot for a typical Run I data acquisition run. The lower two plots show the x and y projections, respectively, with a fit to a Gaussian distribution superimposed. This shows that the transverse profile of the Tevatron beam was roughly Gaussian and circular, with a width σ of $\sim$25 μm in both the x and the y direction.

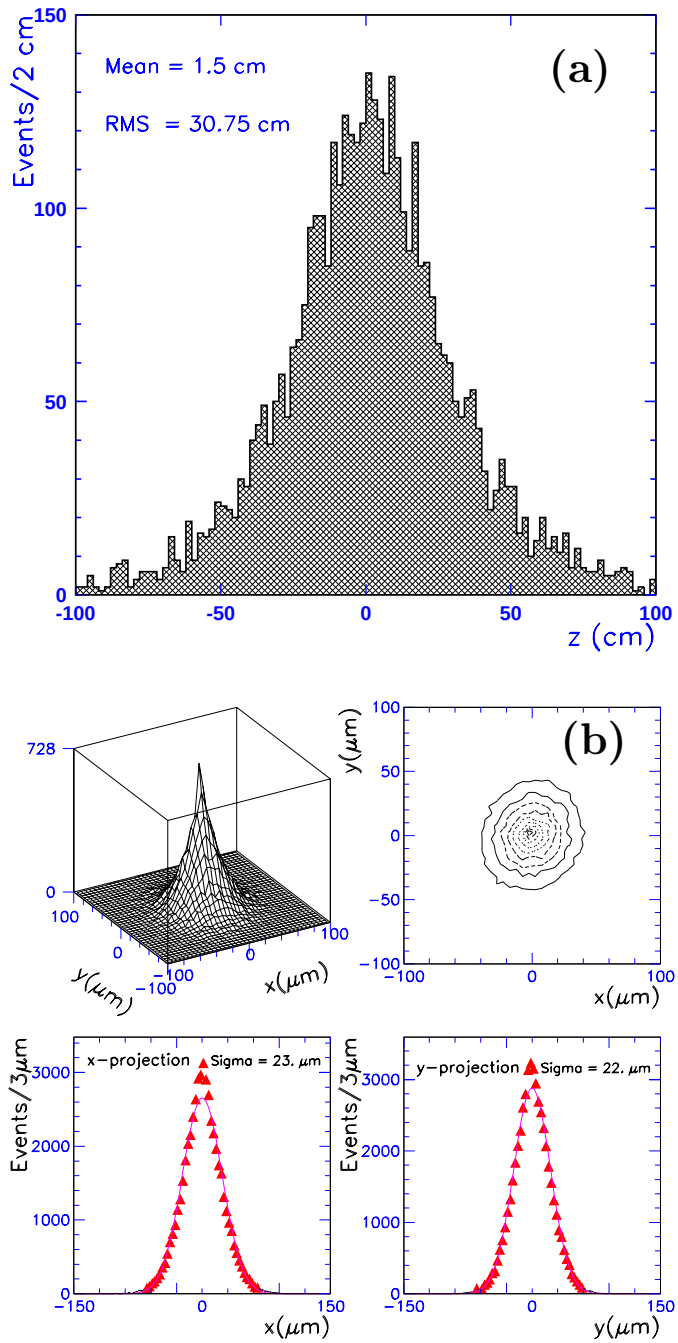

Fig. 20. (a) Distribution of primary $p\bar{p}$ interaction vertices along the proton direction (z) for a typical data acquisition run during the 1994–95 running period. (b) The two-dimensional distribution of the beam spot for a typical data acquisition run is shown in the upper two diagrams. The x and y projections, respectively, are shown in the lower two plots.

6.2.2. *Primary event vertex*

The B hadron lifetime measurements reported in this article are based on measuring the distance between the primary $p\bar{p}$ event vertex and the secondary B decay vertex in the transverse plane exploiting CDF's silicon vertex detector. First, the z position of the primary interaction vertex is identified, using the tracks reconstructed in the VTX detector, and then the transverse position of the primary event vertex is determined, using the run average beam position. The tracks reconstructed in the VTX detector, when projected back to the beam axis, determine the longitudinal location of the primary interaction with an accuracy of about 0.2 cm along the beam direction. On average during Run I, the number of reconstructed interaction vertices in a given event follows a Poisson distribution with a mean of about 2.5. For B hadron lifetime measurements, the z location of the primary event vertex is usually determined by choosing the $p\bar{p}$ interaction vertex, recorded by the VTX which is closest to the intercept of the B candidate with the beamline. Usually, the z coordinates of all tracks from the B decay are required to be within 5 cm of the z position of this primary vertex, in order to exclude tracks from other $p\bar{p}$ interactions in the event.

The transverse position of the primary event vertex is determined using the average beam position through the detector, together with the knowledge of the longitudinal primary vertex position from the VTX. The average beam position is calculated offline for each data acquisition run. It is found that the average beam trajectory is stable over the period in which a given $p\bar{p}$ beam is stored in the Tevatron Collider. For B lifetime measurements, usually only events from data runs with a sufficiently large number of collected events are considered in order to allow a good determination of the run averaged beamline.

In B lifetime analyses, the primary vertex is usually not measured on an event-by-event basis, because the presence of a second b quark decay in the event, coupled with the low multiplicity in for example semileptonic B decays, can lead to a systematic bias in the lifetime determination. The algorithm that determines the primary event vertex on an event-by-event basis calculates first the z position of the primary $p\bar{p}$ interaction vertex from the VTX in the same way described above. The transverse position of the primary vertex is then determined for each event by a weighted fit of all SVX tracks, with a z coordinate within 5 cm of the z vertex position obtained from the VTX. At first, all SVX tracks are fit to originate from a common vertex. Tracks which have large impact parameters, with respect to this vertex, are then removed and the fit is repeated in an iterative process until no more tracks are removed. At least five tracks must remain for a successful primary vertex reconstruction to occur. The uncertainty in the fitted primary vertex coordinates transverse to the beam direction ranges from about 10 to 35 μm, depending on the number of tracks used in the fit and the event topology.

6.2.3. *Decay length measurement*

In the following, we describe the reconstruction of the B hadron decay length on the more complicated example of a partially reconstructed B decay. We shall point out the difference to the simpler case of a fully reconstructed B hadron. As our example, we choose a semileptonic decay $B \to D\ell\nu$, which would represent a lifetime measurement using, for example, $B^0 \to D^-\ell^+\nu$ or $B_S^0 \to D_S^-\ell^+\nu$ decays. A schematic representation of such a semileptonic $B \to D\ell\nu$ decay is displayed in Fig. 21.

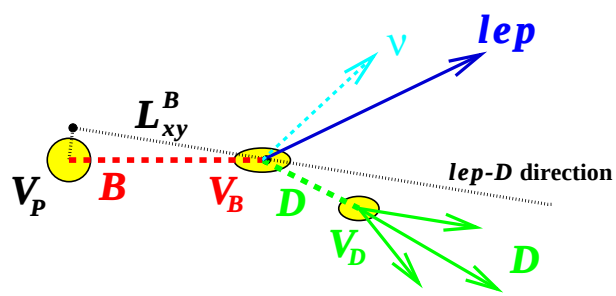

Fig. 21. Schematic representation of a semileptonic $B \to D\ell\nu$ decay.

Usually, the D candidate is searched for in a cone in $\eta\varphi$ space around the lepton candidate and fully reconstructed. The tracks forming the D candidate are then refit with a common vertex constraint referred to as the tertiary vertex and marked as V_D in Fig. 21. The secondary vertex, where the B decays to a lepton and a D (referred to as V_B), is obtained by simultaneously intersecting the trajectory of the lepton track with the flight path of the D candidate. If the D meson is fully reconstructed, which is usually the case, the D flight path and thus the B decay vertex are known. The confidence level (CL) of the combined vertex fit is typically required to be greater than 1%. Furthermore, it is often required that the reconstructed D decay vertex V_D be positively displaced from the primary vertex, as projected along the direction of the $D\ell$ momentum.

The decay length L_{xy}^B is then defined as the displacement of the secondary vertex V_B from the primary event vertex V_P, measured in the plane transverse to the beam axis and projected onto the transverse momentum of the $D\ell$ system (see Fig. 21):

$$L_{xy}^B = \frac{(\mathbf{V}_B - \mathbf{V}_P) \cdot \mathbf{p}_t(D\ell)}{|\mathbf{p}_t(D\ell)|} \,. \tag{10}$$

L_{xy}^B is a signed variable which can be negative for the configuration, where the particle seems to decay before the point where it is produced. The B meson decay time is given by

$$ct(B) = L_{xy}^B \, \frac{m(B)}{p_t(B)} \,, \tag{11}$$

where $m(B)$ is the mass of the B hadron. In the case of a fully reconstructed B hadron, $p_t(B)$ is known and $ct(B)$ is used as input to fit directly for the B lifetime. In the case of a semileptonic B decay, where the B meson is not fully reconstructed, a "pseudo-proper decay length" is usually defined as

$$\lambda = L_{xy}^{B} \frac{m(B)}{p_t(D\ell)} \,. \tag{12}$$

Using single lepton trigger data, the reconstructed B decay length has a typical uncertainty of ~ 50–60 μm, including the contribution from the finite size of the primary event vertex. In addition, the ratio K of the observed momentum to the true momentum is introduced as

$$K = \frac{p_t(D\ell)}{p_t(B)} \,, \tag{13}$$

to correct between the reconstructed $p_t(D\ell)$ and the unknown $p_t(B)$ in the data. The B meson decay time is then given as

$$ct(B) = L_{xy}^{B} \frac{m(B)}{p_t(D\ell)} \otimes K \,. \tag{14}$$

The correction between $p_t(D\ell)$ and $p_t(B)$ is done statistically by smearing an exponential decay distribution with a Monte Carlo distribution of the correction factor K, when extracting $c\tau(B)$ from the pseudo-proper decay length in the lifetime fit procedure as described in Subsec. 6.2.4.

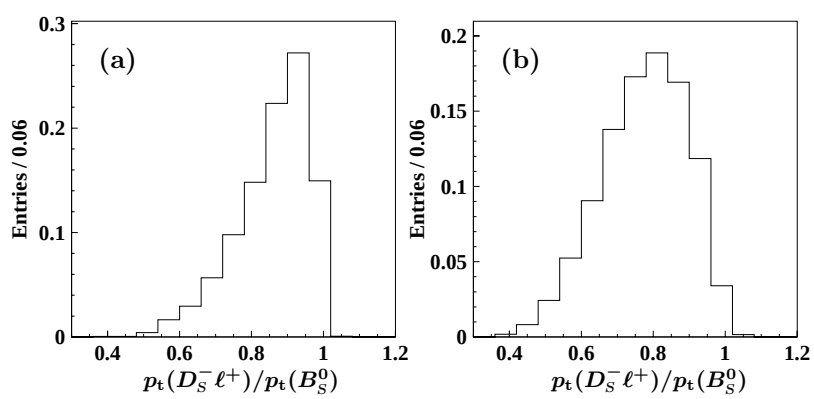

Fig. 22. Examples of normalized K factor distributions $p_t(D_S^-\ell^+)/p_t(B_S^0)$, for $B_S^0 \to D_S^-\ell^+\nu X$ Monte Carlo decays with (a) $D_S^- \to \phi\pi^-$ and (b) $D_S^- \to \phi\mu^-\bar{\nu}$.

The K distribution is obtained from $D\ell$ combinations which originate from a Monte Carlo simulation of the semileptonic B decay of interest. As an example, the K distribution is shown in Fig. 22 for the B_S^0 lifetime measurement using the semileptonic decay $B_S^0 \to D_S^-\ell^+\nu$, which is further described in Subsec. 6.5. Figures 22(a) and 22(b) show the K distribution for the cases where the D_S^- meson

is reconstructed in the $D_S^- \to \phi\pi^-$ and $D_S^- \to \phi\mu^-\bar{\nu}$ decay modes, respectively. These K distributions have mean values of 0.86 and 0.77, with RMS values of 0.10 and 0.12 for $D_S^- \to \phi\pi^-$ and $D_S^- \to \phi\mu^-\bar{\nu}$, respectively. The K distribution is approximately constant as a function of $p_t(D\ell)$ in the range of interest, which is typically 15–25 GeV/c for single lepton trigger data.

To ensure a precise B lifetime determination, usually only B candidates are considered for which the pseudo-proper decay length is measured with an uncertainty of less than 0.1 cm. In addition, the D candidates are often required to have a proper decay length measured between V_B and V_D of less than 0.1 cm and an uncertainty on this proper decay length of less than 0.1 cm. These requirements reject poorly measured decays and reduce random track combinations.

6.2.4. *Description of the lifetime fit procedure*

We now describe the fit procedure used to extract the B lifetime from the pseudo-proper decay length distribution. We continue to use our example of a semileptonic $B \to D\ell\nu$ decay. As input to the B hadron lifetime fit, usually, a signal sample is defined by a mass window around the respective D mass peak. To model the pseudo-proper decay length distribution of the background events contained in the signal sample, a background sample is defined consisting of events from the D sidebands. See Fig. 15(a) for a better understanding of the definition of signal events (light-shaded area) and sideband samples (dark-shaded area), shown here for a $J/\psi \to \mu^+\mu^-$ invariant mass distribution.

The pseudo-proper decay length distribution obtained from the signal sample is then fit using an unbinned maximum log-likelihood method. Both the B lifetime, denoted as $c\tau$ below, and the background shape are determined in a simultaneous fit using the signal and background samples. Thus the likelihood function $\mathcal{L}$ is a combination of two parts:

$$\mathcal{L} = \prod_i^{N_S} \left[f_{\rm sig}\mathcal{F}^i_{\rm sig} + (1 - f_{\rm sig})\mathcal{F}^i_{\rm bg} \right] \cdot \prod_j^{N_B} \mathcal{F}^j_{\rm bg}\,, \tag{15}$$

where N_S and N_B are the number of events in the signal and background samples. Here, $f_{\rm sig}$ is the ratio of D signal events to the total number of events in the signal sample. To constrain $f_{\rm sig}$, which is usually a free fit parameter, to the number of D signal events $\langle f_{\rm sig}\rangle$ with uncertainty $\sigma_{\rm sig}$, obtained from the D mass distribution, an additional χ^2 term, $\chi^2 = (f_{\rm sig} - \langle f_{\rm sig}\rangle)^2/\sigma^2_{\rm sig}$, is factored into the likelihood function defined above.

The signal probability function, $\mathcal{F}_{\rm sig}$, consists of a normalized decay exponential function convoluted with a Gaussian resolution function $\mathcal{G}$ and is smeared with a normalized K distribution, $\mathcal{H}(K)$:

$$\mathcal{F}^i_{\rm sig}(x) = \int dK\, \mathcal{H}(K) \left[\frac{K}{c\tau} \exp\left\{ -\frac{Kx}{c\tau} \right\} \otimes \mathcal{G}(\lambda_i \,|\, x, s\sigma_i) \right]. \tag{16}$$

Here, λ_i is the pseudo-proper decay length measured for event i with uncertainty σ_i and x is the true pseudo-proper decay length. The symbol $\otimes$ denotes a convolution and $\mathcal{G}(\lambda_i|x, s\sigma_i)$ is the Gaussian distribution given by

$$\mathcal{G}(\lambda_i\,|\,x, s\sigma_i) = \frac{1}{s\sigma_i\sqrt{2\pi}} \exp\left(-\frac{(x-\lambda_i)^2}{2s^2\sigma_i^2}\right). \tag{17}$$

Because of systematic uncertainties in the overall scale of the decay length uncertainties, which are estimated on an event-by-event basis, a scale factor, s, is often introduced. It is usually a free parameter in the B lifetime fit. The integration over the momentum ratio K is approximated by a finite sum

$$\int dK\,\mathcal{H}(K) \to \sum_i \Delta K\,\mathcal{H}(K_i)\,, \tag{18}$$

where the sum is taken over bin i of a histogrammed distribution $\mathcal{H}(K_i)$ with bin width ΔK, as shown for example in Fig. 22.

The background probability function, $\mathcal{F}_{\rm bg}$, is typically parametrized by a Gaussian centered at zero, a negative exponential tail, and a positive decay exponential to characterize the contribution of heavy flavor decays in the background sample:

$$\begin{aligned}\mathcal{F}^i_{\rm bg}(x) = (1-f_+-f_-)\mathcal{G}(\lambda_i\,|\,x, s\sigma_i) + \frac{f_+}{\lambda_+}\exp\left\{-\frac{x}{\lambda_+}\right\}\otimes\mathcal{G}(\lambda_i\,|\,x, s\sigma_i)\\ + \frac{f_-}{\lambda_-}\exp\left\{-\frac{x}{\lambda_-}\right\}\otimes\mathcal{G}(\lambda_i\,|\,x, s\sigma_i)\,.\end{aligned} \tag{19}$$

Here, $f_\pm$ are the fractions of positive and negative lifetime backgrounds and $\lambda_\pm$ are the effective lifetimes of those backgrounds. The parameters usually allowed to float in the fit are the B lifetime, $f_{\rm sig}$, $\lambda_\pm$, $f_\pm$, and the overall scale factor s.

For a fully reconstructed B decay, the smearing with a normalized K distribution $\mathcal{H}(K)$ does not apply but the convolution with the Gaussian resolution function $\mathcal{G}$ is essential for obtaining the true pseudo-proper decay length x. In the case of a fully reconstructed B decay, the background is usually also described by a Gaussian centered at zero, a negative exponential tail, and a positive decay exponential.

6.3. *Measurement of the average B hadron lifetime*

The measurement of the average B hadron lifetime is based on $B \to J/\psi X$ decays where the J/ψ is reconstructed through its decay into $\mu^+\mu^-$. This measurement constitutes the first publication of a B lifetime at CDF[35] using only about half of the Run Ia data. This analysis demonstrated in 1993 the capabilities of the newly installed silicon vertex detector. The final average B hadron measurement[36] uses a subset of the J/ψ data sample already shown in Fig. 15(a). Only the Run Ib data and only J/ψ candidates, where both muons are matched to a CFT track at Level 2, are used. Since the precision of the measurement is limited by systematics, including more data would not improve the result.

This analysis uses the two-dimensional decay length L_{xy} of the J/ψ vertex and corrects for the difference between the boost of the J/ψ meson and the B hadron, using a Monte Carlo model which compared the background-subtracted p_t distribution of the data with the J/ψ momentum of the MC simulation (see Subsec. 6.2.3). Care is taken in this analysis to avoid non-Gaussian components in the errors on the decay length distribution. To ensure that the J/ψ vertex is well measured and to have a good understanding of the σ of the vertex fit, strict track and vertex quality cuts are applied. These required, for example, both muons to have associated clusters in all four layers of the SVX or the calculated uncertainty on the decay length $\sigma_{L_{xy}}$ to be less than 150 μm. This leaves 67,800 pairs of oppositely charged muons in the J/ψ signal region and 7,900 pairs in the combined sidebands, which are used to determine the decay length distribution of the background underneath the J/ψ signal.

The pseudo-proper decay length distribution for the signal region, with the result of the fit superimposed, is already shown in Fig. 15(b). The dark-shaded area shows the contribution from the background, where the shape is determined from the sidebands and the magnitude is derived by normalizing the number of sideband events within Poisson fluctuations to the same range in invariant mass as used for the signal sample. The light-shaded region shows the contribution due to adding the exponential distribution from B decay to the background. The remaining unshaded region, which constitutes more than 80% of the J/ψ sample, shows the contribution from prompt J/ψ mesons produced at the primary interaction vertex.

The measured inclusive B lifetime, which is the average over all B hadrons produced in $p\bar{p}$ collisions at $\sqrt{s} = 1.8$ TeV weighted by their production cross section, branching ratios and detection efficiencies, is

$$\langle \tau(B) \rangle = \left(1.533 \pm 0.015^{+0.035}_{-0.031}\right) \text{ ps}\,. \tag{20}$$

The first uncertainty is statistical and the second is systematic. This is the standard way to present results where two uncertainties are quoted in this paper.

6.4. *Measurement of the B^+ and B^0 lifetimes*

6.4.1. *B^+ and B^0 lifetimes with fully reconstructed B mesons*

The analysis principle for the B lifetime measurement using fully reconstructed B^+ and B^0 mesons[36] is as follows. All Run I dimuons forming a J/ψ candidate, as shown in Fig. 15(a), are used. B^+ mesons are reconstructed in the decay modes $J/\psi K^+$, $J/\psi K^{*+}$, $\psi(2S)K^+$ and $\psi(2S)K^{*+}$, while B^0 mesons are reconstructed in the decay modes $J/\psi K^0_S$, $J/\psi K^{*0}$, $\psi(2S)K^0_S$ and $\psi(2S)K^{*0}$, with $\psi(2S) \to \mu^+\mu^-$. The kaons are reconstructed using the decay channels $K^{*0} \to K^+\pi^-$, $K^{*+} \to K^0_S\pi^-$ and $K^0_S \to \pi^+\pi^-$. K^* candidates are accepted if their invariant $K\pi$ mass is within ± 80 MeV/c^2 of the world average K^* mass.[3] Since swapping the assignment of the kaon and pion masses to the two tracks forming a K^{*0} candidate can also result in a K^{*0} candidate within the ± 80 MeV/c^2 mass window, the K^{*0} combination closest to the world average mass value is chosen.

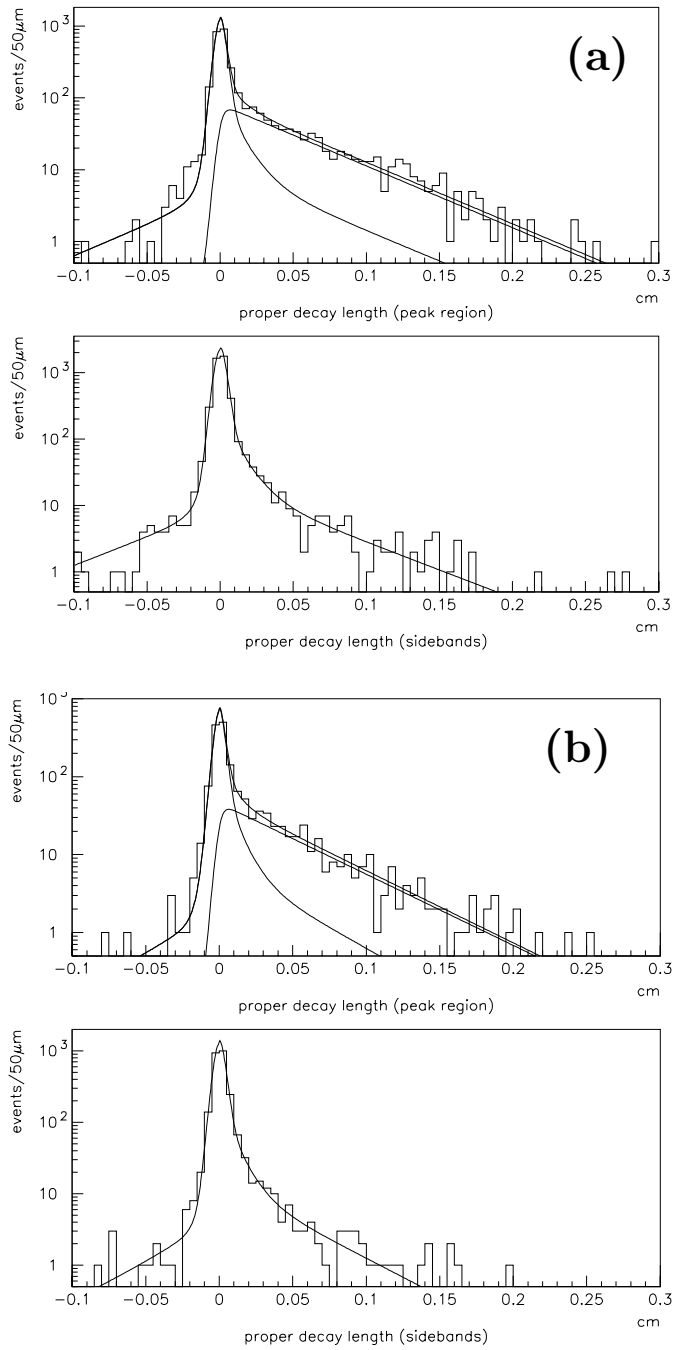

Fig. 23. The proper decay length distribution for fully reconstructed (a) B^+ mesons and (b) B^0 mesons. The upper (lower) histogram shows the peak (sideband) region distribution. The superimposed curves are the contributions from the signal, the background and their sum determined by the log-likelihood fit.

The vertex and mass constraint J/ψ and $\psi(2S)$ candidates are fit with the kaon candidates to originate from a common vertex, yielding the two-dimensional B meson decay length L_{xy}^B. Together with the measured B transverse momentum p_t, L_{xy}^B is used to obtain the proper time distributions shown in Fig. 23 for (a) charged and (b) neutral B candidates. The bottom plots represent the backgrounds as obtained by fitting the B sideband regions to a Gaussian with exponential tails. Using this background shape, an unbinned maximum log-likelihood fit of the signal, assumed to be an exponential convoluted with a Gaussian, is performed. The following lifetimes are obtained:

$$\begin{aligned} \tau(B^+) &= (1.68 \pm 0.07 \pm 0.02)\ \text{ps}\,, \\ \tau(B^0) &= (1.58 \pm 0.09 \pm 0.02)\ \text{ps}\,, \\ \tau(B^+)/\tau(B^0) &= 1.06 \pm 0.07 \pm 0.02\,. \end{aligned} \tag{21}$$

In the calculation of the uncertainty on the lifetime ratio, the correlated systematic errors are properly taken into account.

The exclusive B lifetime measurement using fully reconstructed B decays is statistics-dominated. One way to increase the number of B candidates is not to fully reconstruct the B meson. This is done in the semi-exclusive analysis described in the next subsection.

6.4.2. *B^+ and B^0 lifetimes with partially reconstructed B mesons*

The B lifetime analysis using partially reconstructed B mesons[37] exploits the semi-leptonic decays $B \to D^{(*)}\ell\nu X$ and follows the description given in Subsecs. 6.2.3 and 6.2.4, as illustrated in Fig. 21. The analysis starts with the single lepton trigger data and searches for charm mesons in a cone around the trigger electron or muon. $D^{(*)}$ meson candidates are reconstructed through their decay modes:

(a) $\bar{D}^0 \to K^+\pi^-$, where the $\bar{D}^0$ is not from a D^{*-} decay,
(b) $D^{*-} \to \bar{D}^0\pi^-$, $\bar{D}^0 \to K^+\pi^-$,
(c) $D^{*-} \to \bar{D}^0\pi^-$, $\bar{D}^0 \to K^+\pi^-\pi^+\pi^-$,
(d) $D^{*-} \to \bar{D}^0\pi^-$, $\bar{D}^0 \to K^+\pi^-\pi^0$, where the π^0 is not reconstructed.

The charm signals for the decay modes (a)–(d) can be seen in Figs. 24(a)–24(d), respectively. Figure 24(a) shows the $K^+\pi^-$ mass spectrum, while in Figs. 24(b)–24(d) the mass difference Δm between the measured invariant masses of the $\bar{D}^0\pi^-$ and $\bar{D}^0$ candidates is displayed. The mass peak is broadened for mode (d) because of the missing π^0 meson. Note that the charm signals in Fig. 24 are quite clean and rather competitive with $D^{(*)}$ signals found at e^+e^- colliders. The number of events in the signal regions and the estimated background fractions are summarized in Table 4.

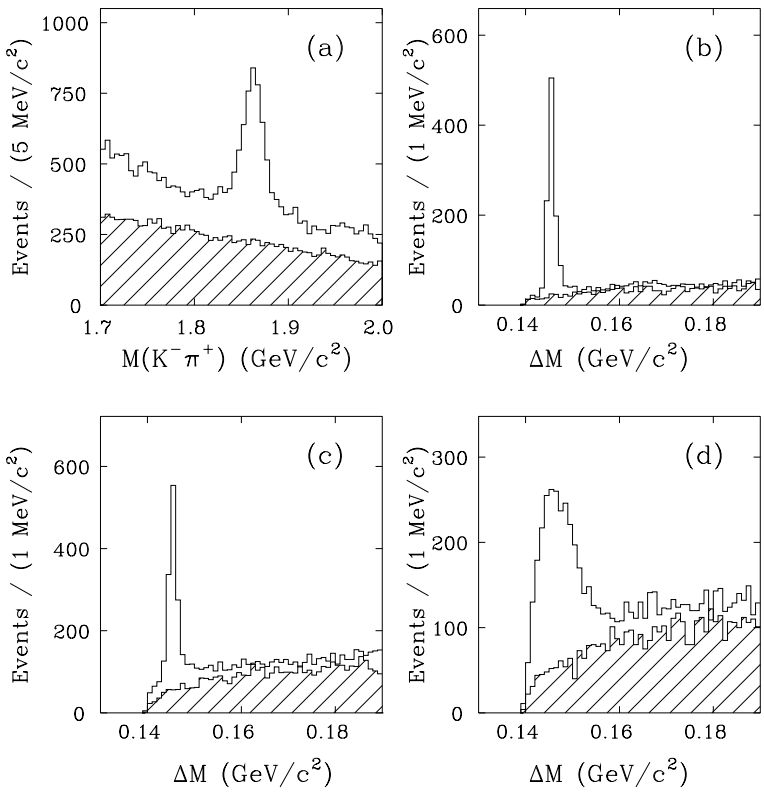

Fig. 24. Charm signals reconstructed in the B lifetime measurement using partially reconstructed $B \to D^{(*)}\ell\nu X$ decays with (a) $\bar{D}^0 \to K^+\pi^-$, where the $\bar{D}^0$ is not from a D^{*-} decay, (b) $D^{*-} \to \bar{D}^0\pi^-$, $\bar{D}^0 \to K^+\pi^-$, (c) $D^{*-} \to \bar{D}^0\pi^-$, $\bar{D}^0 \to K^+\pi^-\pi^+\pi^-$, and (d) $D^{*-} \to \bar{D}^0\pi^-$, $\bar{D}^0 \to K^+\pi^-\pi^0$. The shaded histograms show wrong-sign $D^{*+}\ell^+$ or $D^0\ell^+$ combinations.

Table 4. Summary of the definition of signal samples, numbers of charm candidates and estimated background fractions.

B Mode	$\bar{D}^0$ mode	$\bar{D}^0$ mass range (GeV/c^2)	Δm range (GeV/c^2)	Events	Background fraction
$\ell^+\bar{D}^0$	$K^+\pi^-$	1.84–1.88	Not D^{*-}	5198	0.526 ± 0.018
ℓ^+D^{*-}	$K^+\pi^-$	1.83–1.90	0.144–0.147	935	0.086 ± 0.011
ℓ^+D^{*-}	$K^+\pi^-\pi^+\pi^-$	1.84–1.88	0.144–0.147	1166	0.183 ± 0.015
ℓ^+D^{*-}	$K^+\pi^-\pi^0$	1.50–1.70	< 0.155	2858	0.366 ± 0.016

The $\bar{D}^0$ and D^{*-} candidates are then intersected with the lepton to find the B decay vertex. Since the B meson is not fully reconstructed, a $\beta\gamma$ correction has to be applied to scale from the observed $D^{(*)}\ell$ momentum to $p_t(B)$, as described in Subsec. 6.2.3. The obtained lifetime distributions from $\bar{D}^0\ell^+$ and $D^{*-}\ell^+$ are used to determine the individual B^+ and B^0 lifetimes. A $\bar{D}^0\ell^+$ combination usually

originates from a charged B meson while a $D^{*-}\ell^+$ candidate comes from a B^0. This simple picture is complicated by the existence of D^{**} states, which are the source of $\bar{D}^0$ (D^{*-}) mesons originating from a decay $B^0 \to D^{**-}\ell^+X$, $D^{**-} \to \bar{D}^0X$ ($B^+ \to \bar{D}^{**0}\ell^+X$, $\bar{D}^{**0} \to D^{*-}X$). This cross talk from D^{**} resonances, decomposed using Monte Carlo, is an important aspect of this analysis.[37] A combined lifetime fit to the pseudo-proper decay length distributions, using an unbinned maximum log-likelihood method, as described in Subsec. 6.2.4, yields the results shown in Fig. 25. The contamination of the wrong B species is only at the 10–15% level. It is indicated in Fig. 25, in addition to the respective signal and background contributions.

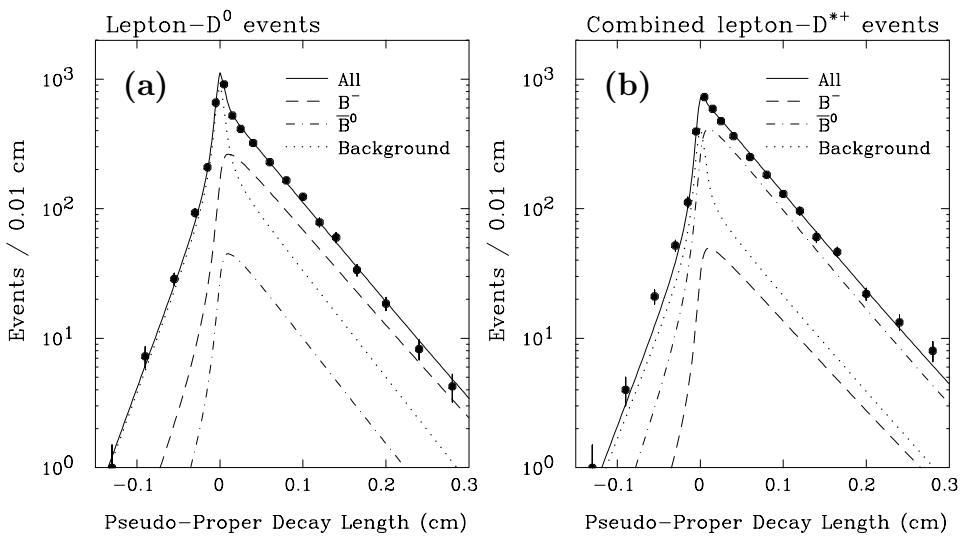

Fig. 25. Pseudo-proper decay length distribution of (a) $\bar{D}^0\ell^+$ and (b) $D^{*-}\ell^+$ candidates where the three $\bar{D}^0$ decay modes are combined. The curves show the result of the combined fit: the B^0 component (dot–dashed curves), the B^+ component (dashed curves) and the background component (dotted curves).

The final lifetimes of the B^+ and B^0 mesons, using their partially reconstructed semileptonic decays $B^+ \to \bar{D}^0\ell^+\nu X$ and $B^0 \to D^{*-}\ell^+\nu X$, are

$$\begin{aligned} \tau(B^+) &= (1.637 \pm 0.058^{+0.045}_{-0.043})\ \text{ps}\,, \\ \tau(B^0) &= (1.474 \pm 0.039^{+0.052}_{-0.051})\ \text{ps}\,, \\ \tau(B^+)/\tau(B^0) &= 1.110 \pm 0.056^{+0.033}_{-0.030}\,, \end{aligned} \tag{22}$$

where the main systematic error is from the estimate of the B meson momentum.

6.4.3. B^0 *and* B^+ *lifetime summary*

We combine the B lifetime measurement using fully reconstructed decays — described in Subsec. 6.4.1 and given in Eq. (21) — with the CDF measurement

using partially reconstructed B mesons — described in Subsec. 6.4.2 and given in Eq. (22) — to derive the following CDF average B lifetimes:

$$\begin{aligned} \tau(B^+) &= (1.661 \pm 0.052)\ \text{ps}\,, \\ \tau(B^0) &= (1.513 \pm 0.053)\ \text{ps}\,, \\ \tau(B^+)/\tau(B^0) &= 1.091 \pm 0.050\,, \end{aligned} \tag{23}$$

where the uncertainties include both statistical and systematic effects. There exists a small (about 0.01 ps) correlation in the systematic effects between the two measurements. This is taken into account in combining the results. The ratio of the two B meson lifetimes differs from unity by about 9%, or almost two standard deviations. This agrees with the small difference predicted by theory.[32]

As an example, a comparison of the CDF B^0 lifetime measurements with other experiments, compiled by the LEP B lifetime working group in July 1998 for the 29th International Conference on High Energy Physics, Vancouver, Canada, can be found in Fig. 26 on the left hand side. A comparison of the CDF B lifetime ratio measurements compared to other experiments is presented in Fig. 26 on the right hand side. These comparisons show that the CDF B lifetime measurements are very competitive with results from the Z^0 pole at LEP and SLC. The current world average B^0 and B^+ lifetimes as of July 1998, determined by the LEP B lifetime working group, taking correlated systematic uncertainties into account, are

$$\begin{aligned} \tau(B^+) &= (1.67 \pm 0.03)\ \text{ps}\,, \\ \tau(B^0) &= (1.57 \pm 0.03)\ \text{ps}\,, \\ \tau(B^+)/\tau(B^0) &= 1.07 \pm 0.03\,. \end{aligned} \tag{24}$$

6.5. *Measurement of the B_S^0 lifetime*

CDF has measured the B_S^0 lifetime using fully and partially reconstructed B_S^0 decays. A search for a lifetime difference $\Delta\Gamma/\Gamma$ in the B_S^0 system is described in Subsec. 6.5.3.

6.5.1. *B_S^0 lifetime with fully reconstructed B_S^0 mesons*

In this exclusive B_S^0 lifetime measurement,[36] the B_S^0 candidates are reconstructed in the decay chain $B_S^0 \to J/\psi\phi$, with $J/\psi \to \mu^+\mu^-$ and $\phi \to K^+K^-$. The dimuon data sample used in the lifetime measurement with fully reconstructed B^0 and B^+ mesons (see Subsec. 6.4.1) is also the starting point to reconstruct J/ψ mesons in this analysis. Once a J/ψ is found, $\phi \to K^+K^-$ candidates are searched by selecting oppositely charged track pairs assigning each track the kaon mass. If the mass of the ϕ candidate lies within ± 10 MeV/c^2 of the world average ϕ mass,[3] all four tracks are constrained to come from a common vertex. The $J/\psi\phi$ invariant mass spectrum is shown in Fig. 27(a). A fit to a Gaussian plus a second order polynomial background yields a signal of 58 ± 12 events.

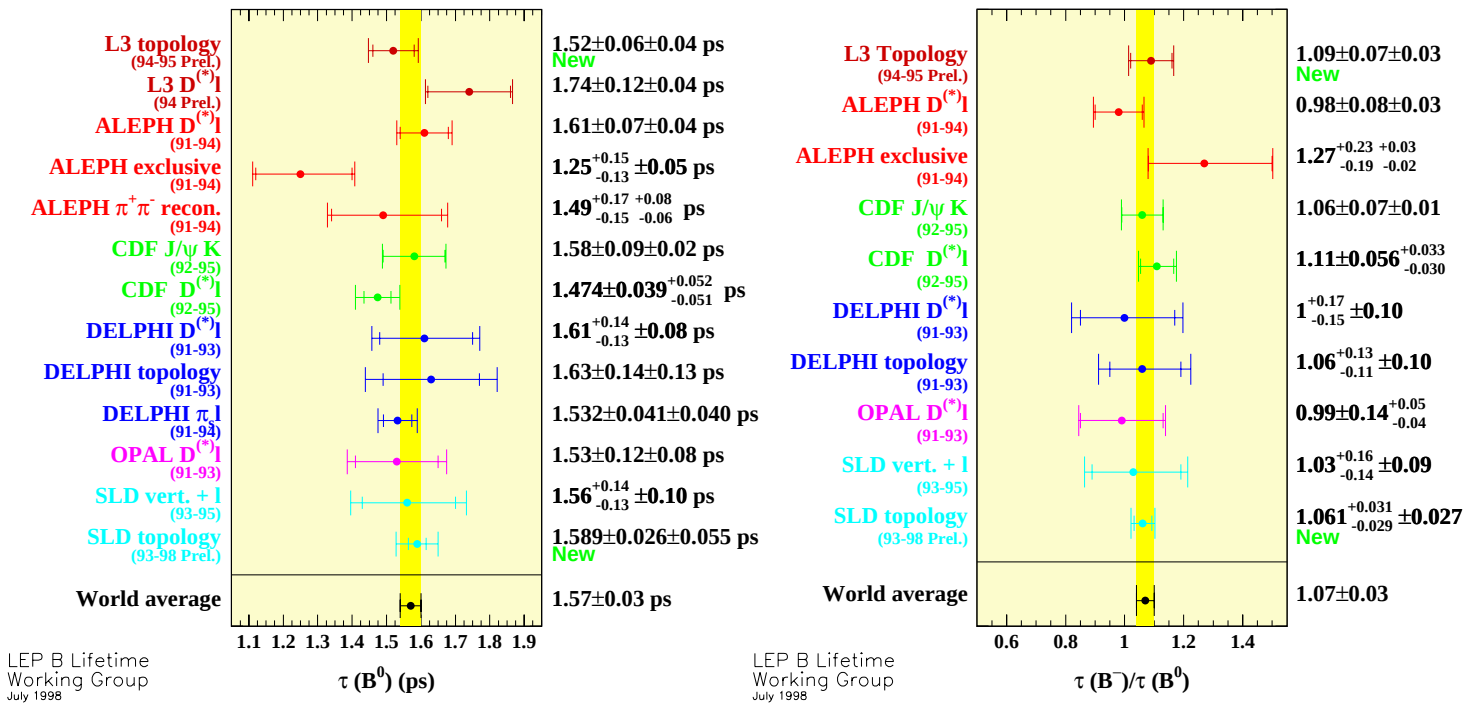

Fig. 26. Comparison of the CDF B^0 lifetime measurements (left) and the $\tau(B^+)/\tau(B^0)$ lifetime ratio measurements (right) with other experiments, compiled by the LEP B lifetime working group as of July 1998.

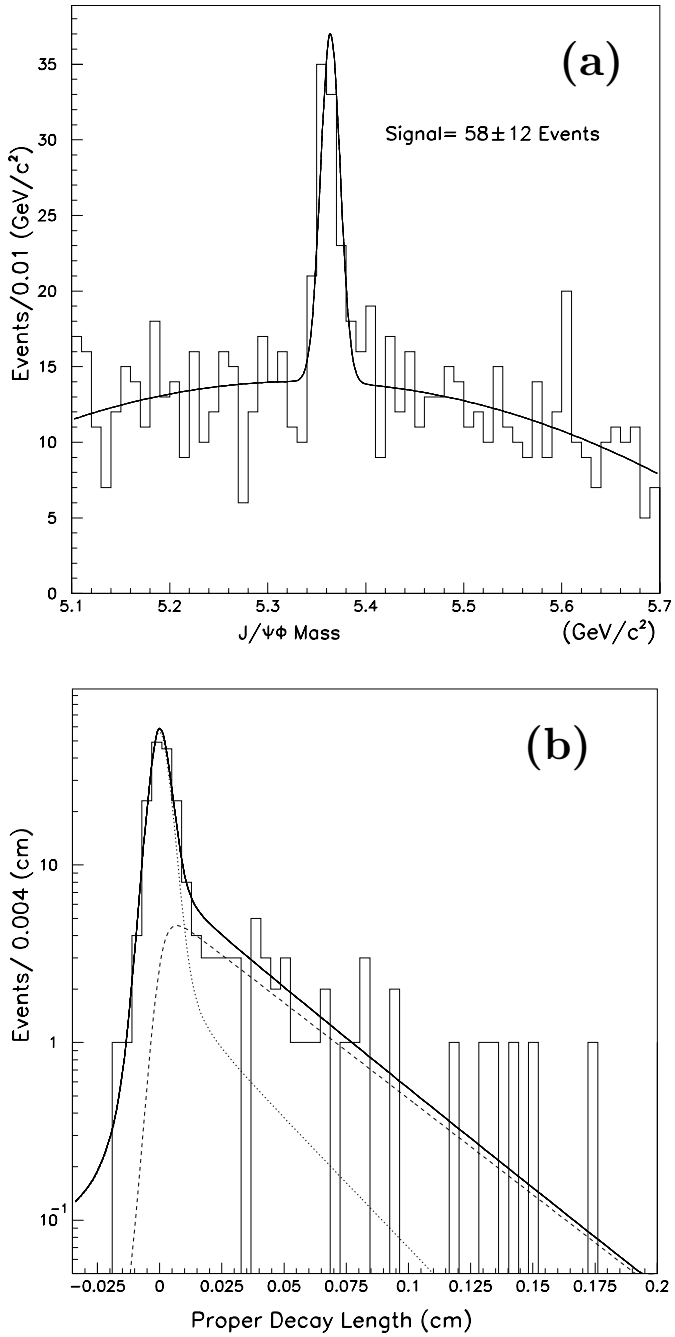

Fig. 27. (a) Invariant mass distribution of B_S^0 candidates from $B_S^0 \to J/\psi\phi$ fitted to a Gaussian plus a polynomial background. (b) B_S^0 proper decay length distribution for events selected within ± 0.05 GeV/c^2 of the fitted B_S^0 mass. The results of the lifetime fit are shown: signal (dashed line), background (dotted line) and the sum of the two (solid line).

Due to the more limited number of B_S^0 candidates in this analysis, a maximum log-likelihood fit is simultaneously performed to the invariant mass and the proper decay length distributions, in order to better constrain the number of B_S^0 signal events. A plot of the proper decay length spectrum is given in Fig. 27(b) for candidates within ± 0.05 GeV/c^2 of the fitted B_S^0 mass. The B_S^0 lifetime is measured in the exclusive mode $J/\psi\phi$ to be

$$\tau(B_S^0) = (1.34^{+0.23}_{-0.19} \pm 0.05)\ \text{ps}\,. \tag{25}$$

Since this B_S^0 lifetime measurement, using fully reconstructed B_S^0 decays, is statistics-dominated, using partially reconstructed B_S^0 decays improves the statistical precision, as described in the following subsection.

6.5.2. B_S^0 *lifetime with partially reconstructed* B_S^0 *mesons*

The B_S^0 lifetime measurement with partially reconstructed B_S^0 mesons[38] uses the semileptonic decay $B_S^0 \to D_S^- \ell^+ \nu$ and is very similar to the B^+ and B^0 lifetime analysis using partially reconstructed B decays (see Subsec. 6.4.2). The D_S^- candidates are reconstructed in the decay modes

(a) $D_S^- \to \phi\pi^-$, $\phi \to K^+K^-$,
(b) $D_S^- \to K^{*0}K^-$, $K^{*0} \to K^+\pi^-$,
(c) $D_S^- \to K_S^0 K^-$, $K_S^0 \to \pi^+\pi^-$,
(d) $D_S^- \to \phi\mu^-\bar{\nu}$, $\phi \to K^+K^-$.

For the first three decay modes the analysis starts with a single lepton trigger data set, while the semileptonic D_S^- decay mode is based on a dimuon data sample obtained with a trigger requirement of $m(\mu\mu) < 2.8$ GeV/c^2. D_S^- candidates are searched for in a cone around the lepton and then intersected with the lepton to find the B_S^0 decay vertex (see also Fig. 21). Since the B_S^0 meson is not fully reconstructed, its ct cannot be directly determined and a $\beta\gamma$ correction is applied to scale from the $D_S^-\ell^+$ momentum to $p_t(B_S^0)$. Figure 28 shows the D_S^- invariant mass distributions for (a) $\phi\pi^-$, (b) $K^{*0}K^-$, (c) $K_S^0K^-$ and (d) K^+K^- from $D_S^- \to \phi\mu^-\bar{\nu}$. The dots with error bars are for right-sign $D_S^-\ell^+$ combinations, while the shaded histograms show the corresponding wrong-sign $D_S^-\ell^-$ distributions, which show no signals. The numbers of D_S^- signal events are compiled in Table 5.

One of the crucial aspects of this analysis is that the reconstructions of the D_S^- decay modes into $K^{*0}K^-$ and $K_S^0K^-$ suffer from reflections of $D^- \to K^{*0}\pi^-$ and $D^- \to K_S^0\pi^-$, respectively, where the π^- is incorrectly assigned the kaon mass. We will discuss this reflection from D^- and the determination of the true number of events from the D_S^- decay with the example of the $D_S^- \to K^{*0}K^-$ mode. The effect of this $K-\pi$ misassignment can be seen in Fig. 29. Events from a $B \to D^-\ell\nu X$ Monte Carlo simulation with $D^- \to K^{*0}\pi^-$ yield an invariant mass distribution indicated by the shape of the shaded area in Fig. 29(c) if they are reconstructed as $B_S^0 \to D_S^-\ell\nu X$ with $D_S^- \to K^{*0}K^-$, misinterpreting the π^- as K^-. A significant

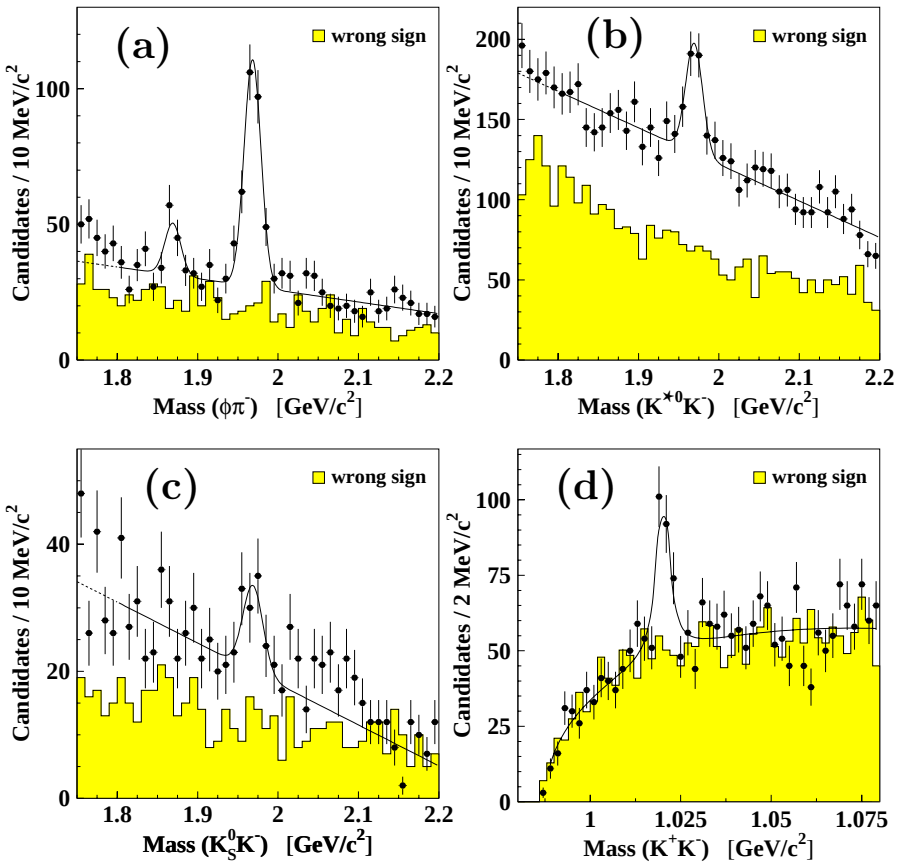

Fig. 28. Invariant mass distributions of candidates for (a) $D_S^- \to \phi\pi^-$, (b) $D_S^- \to K^{*0}K^-$, (c) $D_S^- \to K_S^0K^-$ and (d) $\phi \to K^+K^-$ from $D_S^- \to \phi\mu^-\bar{\nu}$. The dots with error bars are for right-sign $D_S^-\ell^+$ combinations while the shaded histograms show the corresponding wrong-sign distributions. In (a) evidence of the decay $D^- \to \phi\pi^-$ is also present.

Table 5. Summary of the four D_S^- decay modes: the estimated number $N(D_S^-)$ of D_S^- signal events, the number ($N_{\rm evt}$) of events in the signal samples, and the fitted B_S^0 lifetimes $c\tau(B_S^0)$, where the errors shown are statistical only.

D_S^- decay mode	$N(D_S^-)$	$N_{\rm evt}$	$c\tau(B_S^0)$
$\phi\pi^-$	220 ± 21	350	(418^{+43}_{-39}) μm
$K^{*0}K^-$	125 ± 20	820	(411^{+73}_{-66}) μm
$K_S^0K^-$	33 ± 8	146	(397^{+161}_{-152}) μm
$\phi\mu^-\bar{\nu}$	205 ± 38	635	(399^{+50}_{-45}) μm

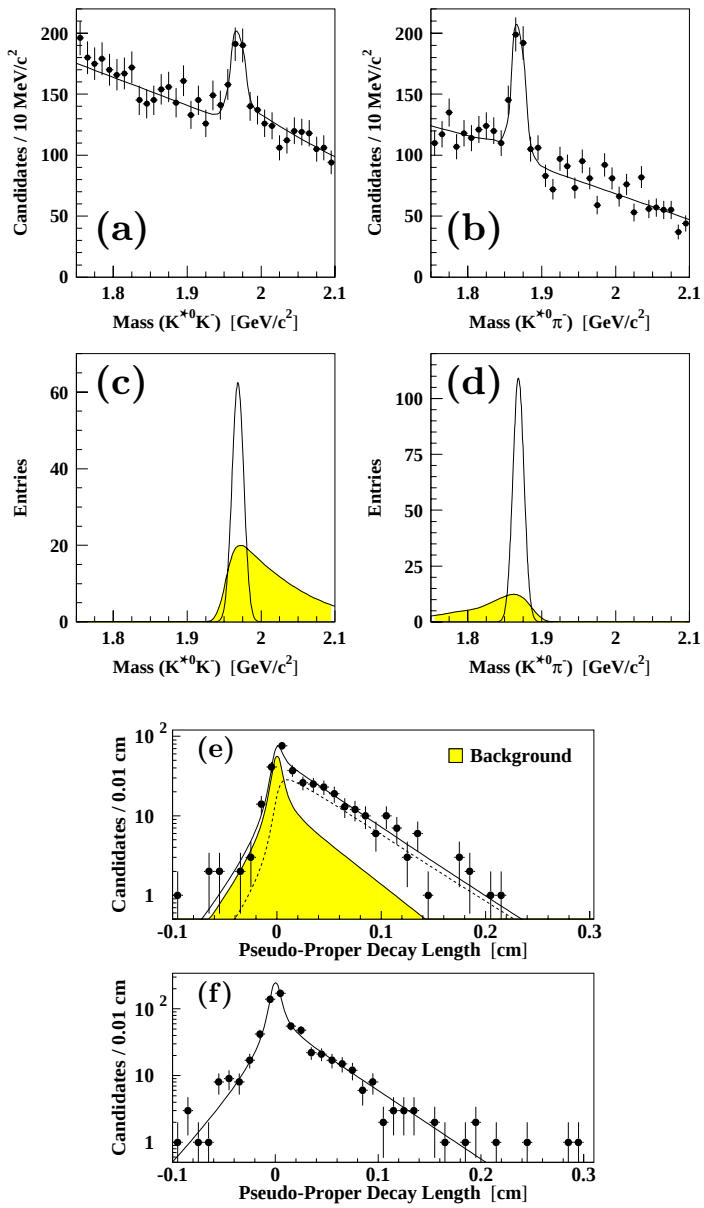

Fig. 29. (a) Mass distribution for candidates in the $D_S^- \to K^{*0}K^-$ decay mode. (b) Mass distribution if these candidates are assumed to be $D^- \to K^{*0}\pi^-$. (c) Distribution of the $D_S^- \to K^{*0}K^-$ signal and the reflection from $D^- \to K^{*0}\pi^-$ (shaded area) as obtained from Monte Carlo simulations. Normalizations are determined from the simultaneous fit described in the text. (d) Mass distribution of the corresponding $D^- \to K^{*0}\pi^-$ signal and the reflection from $D_S^- \to K^{*0}K^-$ (shaded area). (e) B_S^0 pseudo-proper decay length distribution for $D_S^- \to \phi\pi^-$ with the results of the fit superimposed. The dashed line is the B_S^0 signal contribution, while the shaded area represents the contribution from the combinatorial background. (f) Pseudo-proper decay length distribution for the background sample with the fit result superimposed.

portion of this D^- reflection lies at the D_S^- mass peak. Two methods are used to determine the D^- reflection from the data.

The first method performs a simultaneous fit to the $K^{*0}K^-$ and $K^{*0}\pi^-$ invariant mass distributions, where the $K^{*0}\pi^-$ mass distribution is created by switching the mass assignment on the K^- track to a pion. Figure 29(a) shows the $K^{*0}K^-$ mass, while the corresponding $K^{*0}\pi^-$ mass is displayed in Fig. 29(b). Each distribution is described by a Gaussian for the corresponding D^- and D_S^- signal, as shown in Figs. 29(c) and 29(d), plus a linear line shape to parametrize the combinatorial background. The shape of the corresponding D^- or D_S^- reflection, as obtained from a Monte Carlo simulation, is also included in the fit as displayed in Figs. 29(c) and 29(d) as the shaded areas. The two mass distributions are fit simultaneously, with the number of events in the Gaussian D_S^- (D^-) signal set equal to the number of events in the corresponding D^- (D_S^-) reflection. The fit result is shown in Figs. 29(a)–29(d).

The second method for determining the amount of D^- reflection in the D_S^- signal sample exploits the difference between the D^- lifetime [$\tau(D^-) = (1.057 \pm 0.0015)$ ps] and the D_S^- lifetime [$\tau(D_S^-) = (0.467 \pm 0.0017)$ ps]. Fitting for the D_S^- lifetime, the exponential describing the D_S^- signal is replaced by the sum of two exponentials, one with the D_S^- lifetime and one with the D^- lifetime. The D_S^- and D^- lifetimes are fixed to their nominal values[3] and the relative fractions of D_S^- and D^- are allowed to float in the fit. The weighted average of D_S^- events from both methods yields a D_S^- signal fraction of $(62 \pm 10)\%$ for the $D_S^- \to K^{*0}K^-$ decay. Both methods are also used to calculate the number of D_S^- events and the contribution from the D^- reflection in the $D_S^- \to K_S^0 K^-$ decay mode with the result displayed in Table 5.

The B_S^0 lifetime is determined for each of the four D_S^- decay channels individually, with the fit results and their statistical uncertainties shown in Table 5. As an example, the pseudo-proper decay length distribution of the $D_S^- \to \phi\pi^-$ signal sample with the result of the fit superimposed is shown in Fig. 29(e). The dashed line represents the B_S^0 signal contribution, while the shaded area shows the sum of the background probability function over the events in the signal sample. The same distribution of the background sample is displayed in Fig. 29(f). The combined B_S^0 lifetime from all four D_S^- decay modes is determined from a simultaneous fit to be

$$\tau(B_S^0) = (1.36 \pm 0.09^{+0.06}_{-0.05})\ \text{ps}\,. \tag{26}$$

This result is currently the world's best measurement of the B_S^0 lifetime from a single experiment.

Using the CDF average B^0 lifetime $\tau(B^0) = (1.513 \pm 0.053)$ ps (see Subsec. 6.4.3), we determine the B_S^0/B^0 lifetime ratio to be 0.899 ± 0.072, taking correlated systematic uncertainties into account. However, ignoring the correlated systematic uncertainties increases the error on the B_S^0/B^0 lifetime ratio only to ± 0.077, since $\tau(B_S^0)/\tau(B^0)$ is dominated by the statistical error on the B_S^0 lifetime measurement.

6.5.3. *Determination of* $\Delta\Gamma/\Gamma$

In the Standard Model, the B_S^0 meson exists in two CP-conjugate states, $|B_S^0\rangle = |\bar{b}s\rangle$ and $|\bar{B}_S^0\rangle = |b\bar{s}\rangle$. The two mass eigenstates of the B_S^0 meson, B_S^H and B_S^L ($H =$ "heavy" and $L =$ "light"), are not CP eigenstates but are mixtures of the two CP-conjugate quark states:

$$|B_S^H\rangle = 1/\sqrt{2}(|B_S^0\rangle - |\bar{B}_S^0\rangle)\,, \qquad |B_S^L\rangle = 1/\sqrt{2}(|B_S^0\rangle + |\bar{B}_S^0\rangle)\,. \tag{27}$$

The mass and lifetime differences between the B_S^H and B_S^L can be defined as

$$\Delta m \equiv m_H - m_L\,, \quad \Delta\Gamma \equiv \Gamma_L - \Gamma_H\,, \quad \Gamma = 1/2\,(\Gamma_H + \Gamma_L)\,, \tag{28}$$

where $m_{H,L}$ and $\Gamma_{H,L}$ denote the mass and decay width of B_S^H and B_S^L. Note that we have defined both Δm and $\Delta\Gamma$ to be positive quantities. In this case, the heavy state is the long-lived state or the CP-odd state, while the light state is the short-lived state or the CP-even state in analogy to the neutral kaon system. Unlike the B^0 meson, the width difference in the B_S^0 system is expected to be large.[39] Theoretical estimates[40,41] predict $\Delta\Gamma/\Gamma$ to be on the order of 10–20%. In the B_S^0 system the ratio $\Delta m/\Delta\Gamma$ is related to the ratio of the Cabibbo–Kobayashi–Maskawa[5,6] matrix elements $|V_{cb}V_{cs}|/|V_{ts}V_{tb}|$, which is quite well known, and depends only on QCD corrections within the Standard Model.[41,42] A measurement of $\Delta\Gamma$ would therefore imply a determination of Δm and thus a way to infer the existence of B_S^0 meson oscillations, which will ultimately determine the ratio of the CKM matrix elements $|V_{td}|/|V_{ts}|$. The current limit on Δm in the B_S^0 system,[3] $\Delta m_S > 10.2$ ps^{-1} at 95% CL, gives rise to expecting a significant lifetime difference in the B_S^0 system.

An illustrative way to better understand the relation between Δm and $\Delta\Gamma$ in neutral meson systems[43] is shown in Fig. 30. Let us first concentrate on the well-known $B^0\bar{B}^0$ system displayed in Fig. 30(a). Here, the B^0 state is illustrated as its mass excitation curve, a Breit–Wigner line shape, with the x axis representing an energy in ps^{-1}. The width of the Breit–Wigner curve is given by the reciprocal of the B^0 lifetime $1/\Gamma(B^0) \sim 1.6$ ps. The second curve represents the heavy B^0 state, which is separated from the light B^0 state by a mass difference $\Delta m \sim 0.47$ ps^{-1}, which is well measured from $B^0\bar{B}^0$ oscillations. The lifetime difference $\Delta\Gamma$ is very small in the B^0 system, resulting in the two curves appearing with the same width.

The classic system to illustrate Δm and $\Delta\Gamma$ is the $K^0\bar{K}^0$ system, displayed in Fig. 30(b). Here, a short-lived state exists, the K_S^0, shown as the broad curve with a width of $1/\Gamma(K_S^0) \sim 0.09$ ns, and a long-lived state exists, the K_L^0, shown as the narrow curve with a width of $1/\Gamma(K_S^0) \sim 52$ ns. The lifetime of the K_L^0 is about 500 times longer than the K_S^0 lifetime. The mass difference Δm between the states is about 5.3 ns^{-1}. Note that the unit here is in ns^{-1}, compared to ps^{-1} for the $B^0\bar{B}^0$ system. This means that particle–antiparticle oscillations are much slower in the K^0 system than in the B^0 system.

The system of interest, in our case, is the $B_S^0\bar{B}_S^0$ system with a large mass difference between the B_S^L and the B_S^H state. We choose, for example, $\Delta m = 15$ ps^{-1} as drawn in Fig. 30(c). In analogy to the kaon system, the B_S^L is the shorter-lived

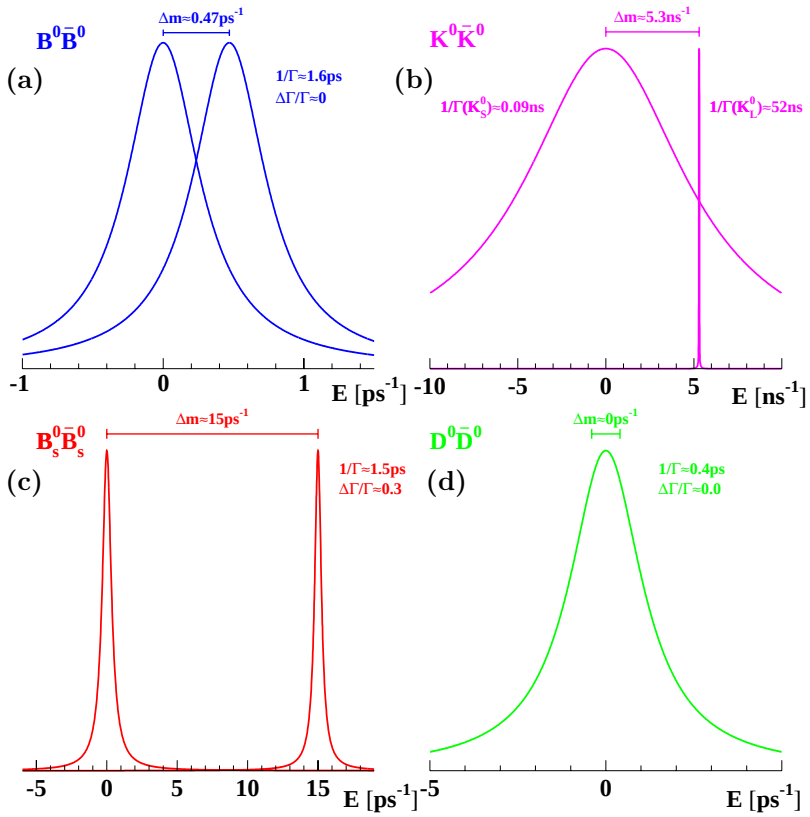

Fig. 30. Illustration of the relation between Δm and $\Delta\Gamma$ in (a) the $B^0\bar{B}^0$ system, (b) the $K^0\bar{K}^0$ system, (c) the $B_S^0\bar{B}_S^0$ system, and (d) the $D^0\bar{D}^0$ system.

state, while the B_S^H is the longer-lived state. In Fig. 30(c) a lifetime difference of $\Delta\Gamma/\Gamma \sim 0.3$ is assumed, resulting in the B_S^L state appearing slightly broader than the B_S^H. Finally, in the $D^0\bar{D}^0$ system, shown in Fig. 30(d), the mass difference Δm is very small in the Standard Model, as is $\Delta\Gamma$. This results in completely overlapping mass excitation curves for both states which appear as one curve with a width of $1/\Gamma \sim 0.4$ ps.

It is assumed that B_S^0 mesons are produced as an equal mixture[41] of B_S^H and B_S^L. One way to search for $\Delta\Gamma$ in the B_S^0 system is to describe the B_S^0 meson decay length distribution by a function of the form

$$\mathcal{F}(t) = 1/2(\Gamma_H e^{-\Gamma_H t} + \Gamma_L e^{-\Gamma_L t}), \quad \text{with} \quad \Gamma_{L,H} = \Gamma \pm \Delta\Gamma/2, \tag{29}$$

rather than by just one exponential lifetime, $\Gamma e^{-\Gamma t}$. Clearly, the integral over time $\int dt\, \mathcal{F}(t)$ returns the same number of B_S^H and B_S^L mesons as produced. This would be the right functional form in a search for a lifetime difference $\Delta\Gamma/\Gamma$, if a completely inclusive sample of B_S^0 mesons is used which is allowed to decay into any final state. However, for a semileptonic final state, the semileptonic decay widths are

the same for B_S^H and B_S^L, since the reason for a lifetime difference originates from hadronic B_S^0 decays. This can be easily seen in the following way. In an excellent approximation, the semileptonic B_S^0 decay is flavor-specific, which means that a ℓ^+ can only originate from a $|\bar{b}s\rangle$ state. Since the fraction of $|\bar{b}s\rangle$ states is the same for B_S^H and B_S^L, the semileptonic widths are the same for B_S^H and B_S^L, and thus the semileptonic branching ratios are different for B_S^H and B_S^L. The correct functional form to describe the B_S^0 meson decay length distribution from semileptonic B_S^0 decays, assuming a lifetime difference $\Delta\Gamma/\Gamma$, is therefore

$$\mathcal{F}(t) = \Gamma_H\Gamma_L/\Gamma \cdot (e^{-\Gamma_H t} + e^{-\Gamma_L t}), \quad \text{with} \quad \Gamma_{L,H} = \Gamma \pm \frac{\Delta\Gamma}{2} = \Gamma \cdot \left(1 \pm \frac{1}{2}\frac{\Delta\Gamma}{\Gamma}\right). \tag{30}$$

The parameter $\Delta\Gamma/\Gamma$ is the parameter that is fit for.

In the case of a lifetime difference $\Delta\Gamma \neq 0$, the total decay width $\Gamma = 1/2 \cdot (\Gamma_H + \Gamma_L)$ and the mean B_S^0 lifetime $\tau_m(B_S^0)$ obtained from a fit assuming a single B_S^0 lifetime, are no longer reciprocal to each other but follow the relation

$$\tau_m(B_S^0) = \frac{1}{\Gamma} \cdot \frac{1 + \left(\frac{\Delta\Gamma}{2\Gamma}\right)^2}{1 - \left(\frac{\Delta\Gamma}{2\Gamma}\right)^2}. \tag{31}$$

The relation (31) is incorporated into the likelihood fitting function for $\Delta\Gamma/\Gamma$, and the mean B_S^0 lifetime is fixed to the world average B^0 lifetime, since the two lifetimes are expected to agree[32,33] within 1%.

The fit returns $\Delta\Gamma/\Gamma = 0.34\ ^{+0.31}_{-0.34}$, where the given error is statistical only. This indicates that with the current statistics CDF is not sensitive to a B_S^0 lifetime difference. Based on this fit result, the normalized likelihood is integrated as a function of $\Delta\Gamma/\Gamma$ and the 95% confidence level limit is found at

$$\Delta\Gamma/\Gamma < 0.83\ (95\%\ \text{CL}). \tag{32}$$

Using a theoretical value of $\Delta\Gamma/\Delta m = (5.6 \pm 2.6) \cdot 10^{-3}$ from Ref. 41 and setting $\tau_m(B_S^0)$ to the world average B^0 lifetime,[3] an upper limit on the B_S^0 mixing frequency of $\Delta m_S < 96\ \text{ps}^{-1}$ (95% CL) can be determined within the Standard Model. Incorporating the dependence on $\Delta\Gamma/\Delta m$ and $\tau_m(B_S^0)$ into the limit, we obtain

$$\Delta m_S < 96\ \text{ps}^{-1} \times \left(\frac{5.6 \cdot 10^{-3}}{\Delta\Gamma/\Delta m}\right) \times \left(\frac{1.55\ \text{ps}}{\tau_m(B_S^0)}\right) \quad (95\%\ \text{CL}). \tag{33}$$

6.6. *Measurement of the Λ_b^0 lifetime*

The analysis principle for the Λ_b^0 lifetime measurement[44] is very similar to the B^0, B^+ and B_S^0 lifetime analyses using partially reconstructed decays. The Λ_b^0 baryon is reconstructed through the semileptonic decay $\Lambda_b^0 \to \Lambda_c^+\ell^-\bar{\nu}X$, with the subsequent decay $\Lambda_c^+ \to pK^-\pi^+$. The analysis again uses the single lepton trigger data searching for Λ_c^+ candidates in a cone around the lepton. The Λ_c^+ candidates

are intersected with the lepton to find the Λ_b^0 decay vertex. A signal of (197 ± 25) Λ_c^+ events is obtained as shown in Fig. 31(a), where the $pK^-\pi^+$ invariant mass distribution for right-sign $\Lambda_c^+\ell^-$ combinations is plotted. The shaded histogram shows the wrong-sign $\Lambda_c^+\ell^+$ distribution.

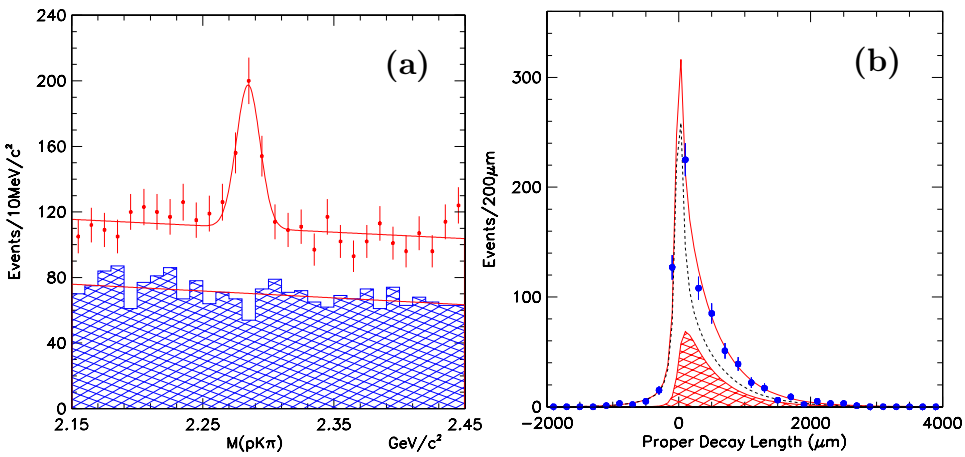

Fig. 31. (a) Invariant mass distribution of $pK^-\pi^+$ for right-sign (points with error bars) and wrong-sign events (shaded area). (b) pseudo-proper decay length distribution of events from the Λ_b^0 signal region. The points with error bars are data, the solid line is the fit result, the shaded area is the signal distribution, and the dashed line is the background contribution.

The pseudo-proper decay length distribution of events from the Λ_b^0 signal region is shown in Fig. 31(b). The points with error bars are data, the solid line is the fit result, the shaded area is the signal distribution, and the dashed line is the background contribution. Using these events, the Λ_b^0 lifetime is determined to be

$$\tau(\Lambda_b^0) = (1.32 \pm 0.15 \pm 0.07)\ \text{ps}\,. \tag{34}$$

The CDF Λ_b^0 lifetime result is competitive with the LEP measurements in precision.[3] Using the CDF average B^0 lifetime $\tau(B^0) = (1.513 \pm 0.053)$ ps (see Subsec. 6.4.3), we determine the lifetime ratio $\tau(\Lambda_b^0)/\tau(B^0) = 0.87 \pm 0.11$. Theory favors the value for this ratio[32] to be in the range of 0.9–1.0, in good agreement with the CDF measurement.

6.7. *Measurement of the B_c^+ lifetime*

Discussing the measurement of the B_c^+ lifetime involves summarizing the recent discovery of the B_c^+ meson at CDF.[45,46] The B_c^+ meson is the lowest-mass bound state of a bottom antiquark and a charm quark: $|B_c^+\rangle = |\bar{b}c\rangle$. This pseudo-scalar ground state has nonzero flavor and no strong or electromagnetic decays. It is the only state with two different heavy quarks where each can decay weakly. As seen in

Fig. 32(a), the $|\bar{b}c\rangle$ state is the last meson state predicted by the Standard Model,[4] which had not been discovered until early 1998. Figure 32(a) shows a quark periodic table with all possible combinations of meson states which can be obtained from the five quarks u, d, s, c and b.

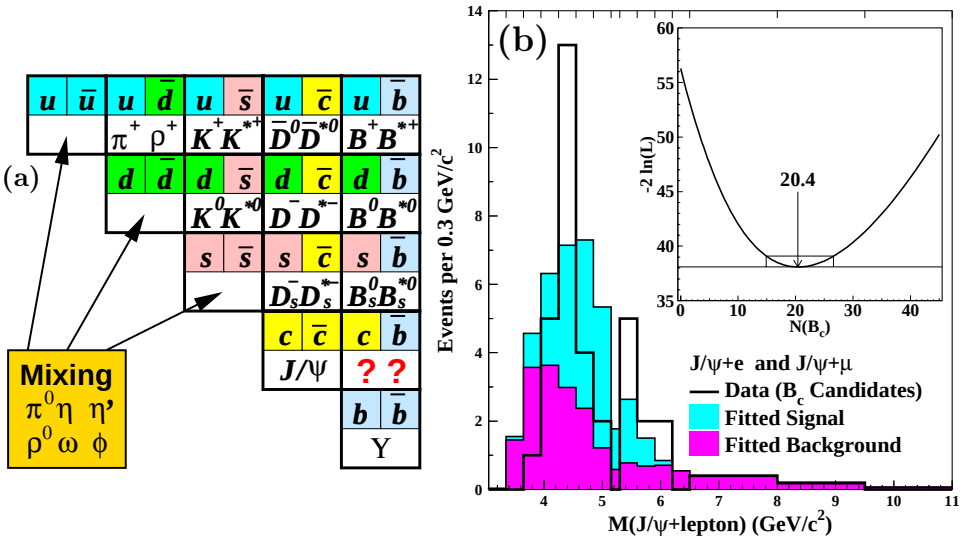

Fig. 32. (a) Sketch of the quark periodic table. (b) Histogram of the $J/\psi\ell$ mass distribution that compares the signal and background determined in the likelihood fits to the combined data for $J/\psi e$ and $J/\psi\mu$. Note that the mass bins, indicated by ticks at the top, vary in width. The inset shows the log-likelihood function versus the number of B_c^+ mesons.

Nonrelativistic potential models predict a B_c^+ mass[47] around 6.2–6.3 GeV/c^2. In these models, the c and $\bar{b}$ quarks are tightly bound in a very compact system and have a rich spectroscopy of excited states. The predicted lifetime[48] of the B_c^+ meson is in the range of 0.4–1.4 ps. Because of the wide range of predictions, a B_c^+ lifetime measurement is a test of the different assumptions made in the various calculations.

We attempt here a simple educated guess of the B_c^+ mass and its lifetime. We would estimate the B_c^+ mass as

$$m(B_c^+) \sim m(b) + m(c) \sim 4.75 \text{ GeV}/c^2 + 1.55 \text{ GeV}/c^2 = 6.3 \text{ GeV}/c^2\,, \qquad (35)$$

where we have approximated the b and c quark masses with half of the mass of the $\Upsilon(1S)$ and the J/ψ, respectively. To estimate the B_c^+ lifetime, we expect three major contributions to the B_c^+ decay width: $\Gamma(B_c^+) \sim \Gamma_b + \Gamma_c + \Gamma_{bc}$. Decays of the $\bar{b}$ quark $\bar{b} \to \bar{c}W^+$, with the c quark as a spectator, leading to final states such as $J/\psi\pi$ or $J/\psi\ell\nu$; c quark decays $c \to sW^+$, with the $\bar{b}$ as spectator, leading to final states such as $B_S^0\pi$ or $B_S^0\ell\nu$; and $c\bar{b} \to W^+$ annihilation, leading to final states like

DK, $\tau\nu_\tau$ or multiple pions. In the simplest view, the c and $\bar{b}$ decay like free quarks with no annihilation contribution, and the B_c^+ lifetime would be

$$\tau(B_c^+) = 1/\Gamma(B_c^+) \sim [\Gamma_b + \Gamma_c]^{-1} \sim [1/1.65\ \text{ps} + 1/0.47\ \text{ps}]^{-1} \sim 0.4\ \text{ps}\,, \qquad (36)$$

where Γ_b is approximated with the B^+ lifetime, while we use $\tau(D_S^-)$ to estimate Γ_c.

6.7.1. *Discovery of the B_c^+ meson at CDF*

The B_c^+ meson is reconstructed via its semileptonic decay $B_c^+ \to J/\psi\ell^+\nu X$ ($\ell = e, \mu$). In this analysis, advantage is taken of a clean $J/\psi \to \mu^+\mu^-$ signal (see Fig. 15 and Subsec. 6.4.1) and excellent lepton identification at CDF. To reduce backgrounds from prompt J/ψ production, trilepton vertices displaced from the primary vertex are searched for by requiring the $J/\psi\ell$ pseudo-proper decay length to be greater than 60 μm. 23 $B_c^+ \to J/\psi e\nu$ candidates and 14 $B_c^+ \to J/\psi\mu\nu$ candidates are found. Because of the missing neutrino the B_c^+ cannot be fully reconstructed and no B_c^+ mass peak can be obtained. The B_c^+ signal is therefore found as an excess of events over expected backgrounds. Great care is taken to correctly determine the different backgrounds in this analysis.[45]

Significant backgrounds in the B_c^+ candidates come from false leptons. These are hadrons reaching the muon detectors without being absorbed, hadrons that decay in flight into a muon in advance of entering the muon detectors and hadrons falsely identified as electrons. Background from photon conversions $\gamma \to e^+e^-$ arises when one member of the pair remains undetected and the other accidentally intersects the J/ψ decay point. Background from $B\bar{B}$ decays arises when a J/ψ from a B decay and a lepton from a semileptonic decay of the $\bar{B}$ appear to originate from the same decay point. A number of other backgrounds[45] are found to be negligible. Table 6 summarizes the results of the background calculation and of a simultaneous fit for the muon and electron channels to the mass spectrum over the region between 3.35 and 11 GeV/c^2. Figure 32(b) shows the mass spectra for the combined $J/\psi\ell$ candidates, the combined backgrounds and the fitted contribution from $B_c^+ \to J/\psi\ell\nu$ decays. The fitted number of B_c^+ events is $20.4^{+6.2}_{-5.5}$.

To test the significance of this result, a number of Monte Carlo trials is generated with the statistical properties of the backgrounds, but with no contribution from B_c^+ mesons. These are subjected to the same fitting procedure to determine contributions consistent with the signal distribution arising from background fluctuations. The probability of obtaining a yield of 20.4 events or more is 0.63×10^{-6}, equivalent to a 4.8-standard-deviation effect.

To check the stability of the B_c^+ signal, the assumed B_c^+ mass is varied from 5.52 to 7.52 GeV/c^2. The signal template for each value of $m(B_c^+)$ and the background mass distributions are used to fit the mass spectrum for the data. The magnitude of the B_c^+ signal is stable over the range of theoretical predictions for $m(B_c^+)$. The minimum in the log-likelihood function versus mass yields a B_c^+ mass of $m(B_c^+) = (6.40 \pm 0.39 \pm 0.13)$ GeV/c^2.

Table 6. Summary of B_c^+ signal and background events.

	$3.35 < m(J/\psi\ell) < 11.0$ GeV/c^2	
	$J/\psi e$ events	$J/\psi\mu$ events
False electrons	4.2 ± 0.4	
Undetected conversions	2.1 ± 1.7	
False muons		11.4 ± 2.4
$B\bar{B}$ background	2.3 ± 0.9	1.44 ± 0.25
Total background (predicted)	8.6 ± 2.0	12.8 ± 2.4
(from fit)	9.2 ± 2.0	10.6 ± 2.3
Predicted $N(B_c^+ \to J\psi e\nu)/N(B_c^+ \to J\psi\ell\nu)$	0.58 ± 0.04	
e and μ signal (derived from fit)	$12.0^{+3.8}_{-3.2}$	$8.4^{+2.7}_{-2.4}$
Total signal (fitted parameter)	$20.4^{+6.2}_{-5.5}$	
Signal + background	21.2 ± 4.3	19.0 ± 3.5
Candidates	23	14
Probability for null hypothesis	0.63×10^{-6}	

The lifetime of the B_c^+ meson is obtained from the decay length distribution using only events with $4.0 < m(J/\psi\ell) < 6.0$ GeV/c^2 and relaxing the requirement on the pseudo-proper decay length from > 60 μm to greater than -100 μm. This yields a sample of 71 events, 42 $J/\psi e$ and 29 $J/\psi\mu$ candidates. An unbinned maximum log-likelihood fit yields

$$\tau(B_c^+) = \left(0.46^{+0.18}_{-0.16} \pm 0.03\right) \text{ ps}\,. \tag{37}$$

The data, together with the signal and background distributions, are shown in Fig. 33(a).

From the 20.4 B_c^+ events and a sample of 290 $B^+ \to J/\psi K^+$ events selected with the same requirements as the B_c^+ candidates, the B_c^+ production cross section times the $B_c^+ \to J/\psi\ell^+\nu$ branching fraction $\sigma \times \text{BR}(B_c^+ \to J/\psi\ell^+\nu)$ is obtained, relative to that for the topologically similar decay $B^+ \to J/\psi K^+$. Many systematic uncertainties cancel in the ratio, while Monte Carlo calculations yielded the values for the efficiencies that do not cancel. The detection efficiency for $B_c^+ \to J/\psi\ell^+\nu$ depends on $c\tau$ because of the cut on the pseudo-proper decay length at > 60 μm. We therefore quote a separate systematic uncertainty from the lifetime uncertainty. We find that

$$\frac{\sigma(B_c) \times \text{BR}(B_c \to J/\psi\ell\nu)}{\sigma(B) \times \text{BR}(B \to J/\psi K)} = 0.132^{+0.041}_{-0.037}\ (\text{stat.}) \pm 0.031\ (\text{syst.})^{+0.032}_{-0.020}\ (c\tau) \tag{38}$$

for B_c^+ and B^+ with transverse momenta $p_t > 6.0$ GeV/c and rapidities $|y| < 1.0$. Figure 33(b) compares phenomenological predictions with the measurements of $\tau(B_c^+)$ and the $\sigma \times$ BR ratio. Within experimental and theoretical uncertainties, they are consistent.

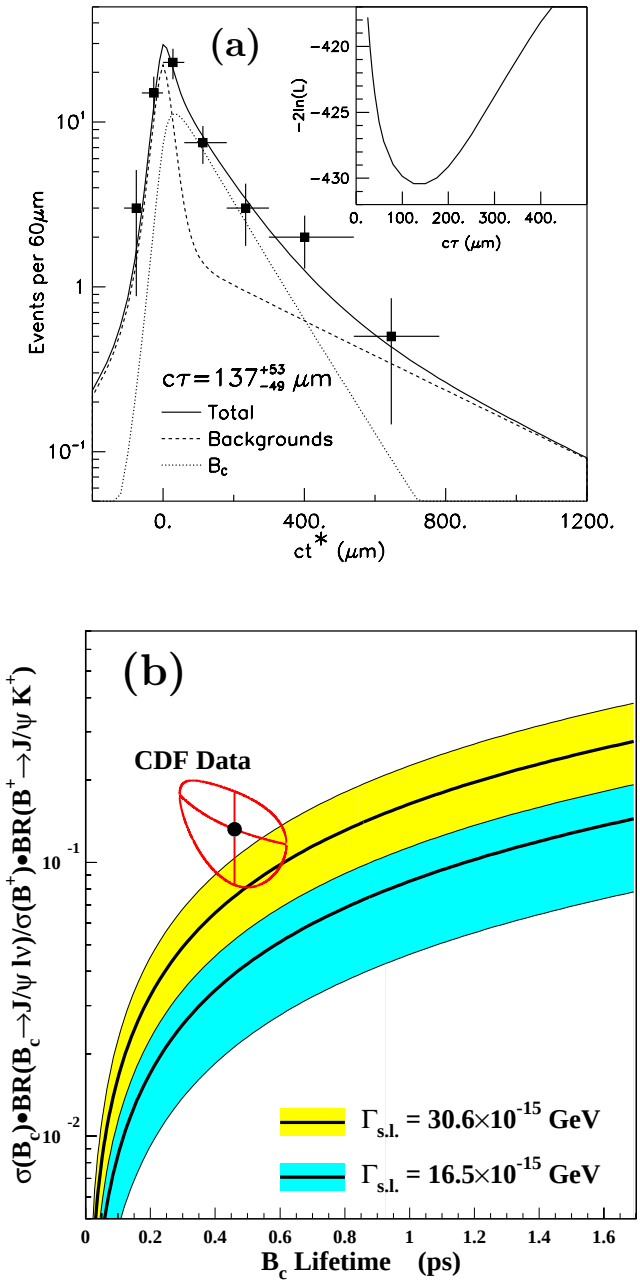

Fig. 33. (a) Pseudo-proper decay length distribution for the combined $J/\psi e$ and $J/\psi\mu$ data with the fit result and the contributions from signal and background overlaid. The inset shows the log-likelihood function versus $c\tau$. (b) Measured value of the $\sigma \times$ BR ratio shown as the point with one standard deviation contour and plotted at the measured value for $\tau(B_c^+)$. The shaded regions represent theoretical predictions and their uncertainty bands for two different values of the B_c^+ semileptonic decay width $\Gamma_{\rm sl}$.

6.8. *B lifetimes: A summary*

A summary of the B lifetime measurements at CDF is given in Fig. 34. As we have seen, CDF's B lifetime results are very competitive with the LEP and SLC measurements, where a precision of a few percent is reached. Although CDF's measurement of the B^+/B^0 lifetime ratio appears to be different from unity by almost two standard deviations, the precision is still not yet sufficient to distinguish between theoretical approaches. The Λ_b^0 lifetime lies closer to the B^0 lifetime at CDF $[\tau(\Lambda_b^0)/\tau(B^0) = 0.87 \pm 0.11]$ compared to the measurements of the LEP experiments.[3] Finally, the B_c^+ lifetime, measured for the first time at CDF, is clearly much shorter than the other B hadron lifetimes and closer to the D^0 or D_S^- lifetime.

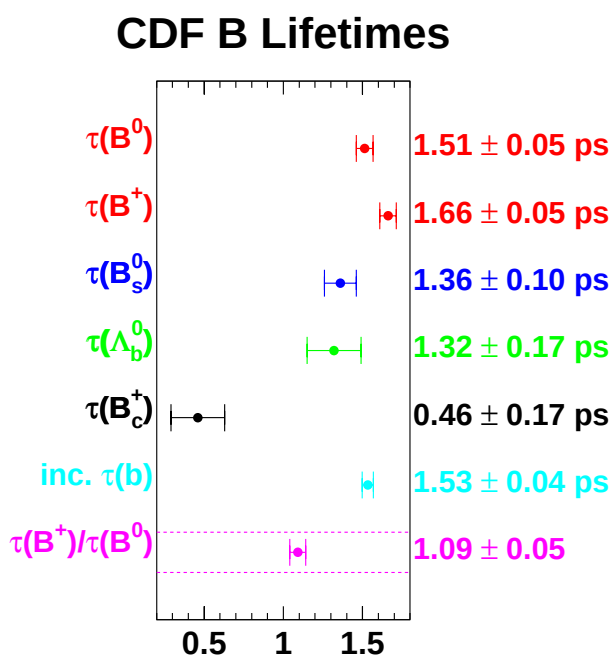

Fig. 34. Summary of CDF B hadron lifetime results.

7. Measurements of $B^0\bar{B}^0$ Oscillations

Oscillations between particles and antiparticles were predicted[49] in 1955 and observed in the system of neutral kaons[50] in 1956. Oscillations in the $B^0\bar{B}^0$ meson system were observed for the first time by the ARGUS collaboration[51] in 1987. This discovery signaled a large top quark mass and gave rise to new prospects for the observation of CP violation in B meson decays (see Sec. 8). In this section, we describe measurements of the time dependence of $B^0\bar{B}^0$ oscillations at CDF. After a short introduction in B flavor oscillations, we review different approaches for measuring the time dependence of $B^0\bar{B}^0$ oscillations at CDF.

7.1. *Introduction to $B^0\bar{B}^0$ oscillations*

As already outlined in Subsec. 6.5.3, the system of neutral B mesons, B^0 and $\bar{B}^0$, can be described in terms of states with well-defined mass and lifetime, B_H and B_L (H = "heavy" and L = "light"):

$$|B^0\rangle = 1/\sqrt{2}(|B^0_L\rangle + |B^0_H\rangle)\,, \qquad |\bar{B}^0\rangle = 1/\sqrt{2}(|B^0_L\rangle - |B^0_H\rangle)\,. \tag{39}$$

Here, we consider the effects of CP violation to be small compared to the expected mixing effects. The difference in mass Δm between the two mass eigenstates leads to a time-dependent phase difference between their wave functions. The probability that an initially pure B^0 state can be observed as a $\bar{B}^0$ at proper time t is given by

$$\mathcal{P}_{\rm mix} = {\rm Prob}(B^0 \to \bar{B}^0, t) = 1/2\Gamma e^{-\Gamma t}(1 - \cos\Delta m t)\,, \tag{40}$$

while the probability that it decays as B^0 is given by

$$\mathcal{P}_{\rm unmix} = {\rm Prob}(B^0 \to B^0, t) = 1/2\Gamma e^{-\Gamma t}(1 + \cos\Delta m t)\,. \tag{41}$$

Figure 35 shows, on the left side, the time evolution of $B\bar{B}$ oscillations displaying the unmixed (solid) and mixed (dashed) contributions for two different oscillation frequencies Δm. The sum of $\mathcal{P}_{\rm mix}$ and $\mathcal{P}_{\rm unmix}$ is just the exponential particle decay $\Gamma e^{-\Gamma t}$ and is displayed as a dotted line in Fig. 35.

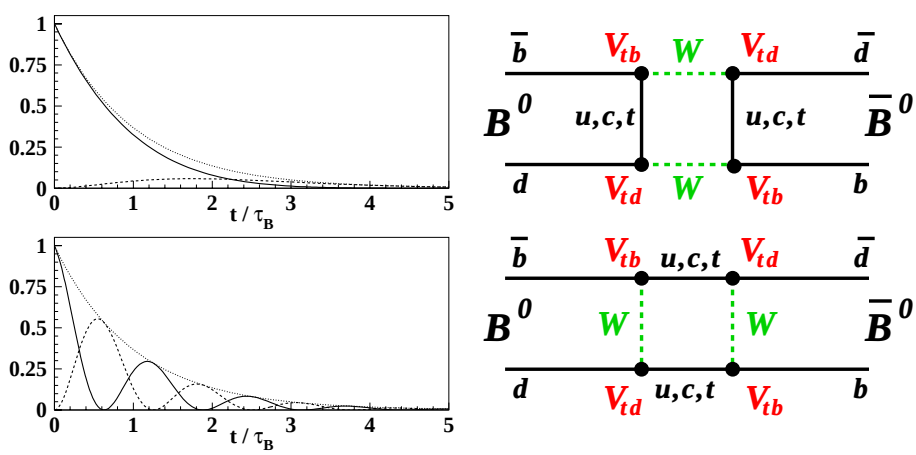

Fig. 35. *Left*: Time evolution of $B\bar{B}$ oscillations displaying the unmixed (solid) and the mixed (dashed) contribution as well as the sum of the two (dotted) for two different oscillation frequencies. *Right*: Box diagram describing $B^0\bar{B}^0$ oscillations.

If the B meson decay time t cannot be measured, the time-integrated probability, which is usually referred to as χ, can be obtained as

$$\chi = \frac{\mathcal{P}_{\rm mix}}{\mathcal{P}_{\rm mix} + \mathcal{P}_{\rm unmix}} = \frac{x^2}{2(1+x^2)}\,. \tag{42}$$

Here, the mixing parameter $x = \Delta m/\Gamma$ is introduced. It describes the oscillation period relative to the B meson lifetime $\tau_B = \hbar/\Gamma$.

If both neutral B mesons, B^0 and B_S^0, are produced, the time-integrated and flavor-averaged mixing parameter $\bar{\chi}$ is defined as

$$\bar{\chi} = f_d\,\chi_d + f_S\chi_S\,, \tag{43}$$

where f_d and f_S are the fractions of b hadrons that are produced as B^0 and B_S^0 mesons, respectively.

In the Standard Model,[4] $B^0\bar{B}^0$ mixing occurs via second order weak processes, as displayed in Fig. 35 on the right hand side. The mass difference Δm_d can be determined within the Standard Model by computing the electroweak box diagram, where the dominant contribution is through top quark exchange:

$$\Delta m_d = \frac{G_F^2}{6\pi^2}\, m_B(f_B^2 B_B)\eta_{\rm QCD} m_t^2 F\left(\frac{m_t^2}{m_W^2}\right)|V_{tb}^* V_{td}|^2\,. \tag{44}$$

Here, G_F is the Fermi coupling constant, m_B the B meson mass, f_B the weak B decay constant, B_B the bag parameter of the B meson, $\eta_{\rm QCD}$ are QCD corrections which are in the order of 1, m_t is the top quark mass, V_{tb} and V_{td} are the two CKM matrix elements involved, and $F(z)$ is a slowly varying function of the top quark mass and the W boson mass m_W:

$$F(z) = \frac{1}{4} + \frac{9}{4(1-z)} - \frac{3}{2}\frac{1}{(1-z)^2} - \frac{3}{2}\frac{z^2\ln z}{(1-z)^3}\,. \tag{45}$$

In the case of the B_S^0 meson the respective values of $B_{B_S^0}$, $f_{B_S^0}$, $m_{B_S^0}$, and $\eta_{\rm QCD} = \eta_{B_S^0}$ have to be used, and V_{td} is replaced by V_{ts}.

A measurement of Δm_d or Δm_S would in principle determine the Cabibbo–Kobayashi–Maskawa matrix elements V_{td} or V_{ts} but theoretical uncertainties connected with the poor knowledge of the B meson weak decay constant f_B and the bag parameter B_B limit the direct extraction of the CKM matrix elements from measurements of Δm_d and Δm_S. However, in the ratio $\Delta m_d/\Delta m_S$ several of the theoretical uncertainties cancel:

$$\frac{\Delta m_d}{\Delta m_S} = \frac{m_{B^0}}{m_{B_S^0}}\,\frac{\eta_{B^0}}{\eta_{B_S^0}}\,\frac{f_{B^0}^2 B_{B^0}}{f_{B_S^0}^2 B_{B_S^0}}\,\frac{|V_{td}|^2}{|V_{ts}|^2} \tag{46}$$

and $\Delta m_d/\Delta m_S$ will ultimately determine one of the legs of the unitarity triangle, as further discussed in Subsec. 8.1.

7.1.1. *Ingredients of $B^0\bar{B}^0$ mixing measurements*

In general, a measurement of the time dependence of $B^0\bar{B}^0$ oscillations requires the knowledge of the proper decay time t of the B meson, the flavor of the B meson at production, and the flavor of the B meson at decay in order to determine whether the B^0 has oscillated. The last two items require identifying the flavor of a B meson. They are the subject of the next Subsec. 7.1.2, where we discuss B flavor tagging. As outlined in Subsec. 6.2.3, the B meson decay time can be obtained from a measurement of the distance L_{xy}^B between the primary interaction vertex,

where the B meson is produced, and its secondary decay vertex. The decay time t is related to the decay distance L_{xy}^B by

$$ct(B) = \frac{L_{xy}^B}{\beta\gamma} = L_{xy}^B \frac{m(B)}{p_t(B)} \,. \tag{47}$$

If the B meson is not fully reconstructed, a $\beta\gamma$ correction is applied to scale from the only partially measured B momentum to the unknown B momentum.

From Eq. (47) the uncertainty on the decay time can be calculated (in units of the B lifetime τ_B):

$$\frac{\sigma_t}{\tau_B} = \sqrt{\left(\frac{\Delta L_{xy}^B}{L_{xy}^0}\right)^2 + \left(\frac{t}{\tau_B}\frac{\Delta p_t}{p_t}\right)^2}\,, \quad \text{where} \quad L_{xy}^0 = p_t/m_B \cdot c\tau_B \,. \tag{48}$$

The proper time resolution σ_t depends on the uncertainty to infer the decay length from the primary to the B decay vertex and on the B momentum resolution which is dominated by the magnitude of the $\beta\gamma$ correction. Note that the latter uncertainty scales with t/τ_B, while the vertexing resolution only adds an uncertainty constant with ct.

7.1.2. *B flavor tagging*

B flavor tagging refers to the task of determining the flavor of a B meson either at production or at decay. Several methods of B flavor tagging exist. Some methods identify the flavor of the other B hadron produced in the initial collision along with the B meson of interest. Since the dominant b quark production mechanism produces $b\bar{b}$ pairs, the flavors of both B hadrons are assumed to be opposite at the time of production. There are three common methods of opposite side flavor tagging. One method, called "lepton tagging," looks for a lepton from the semileptonic decay of the other B hadron in the event. The charge of this lepton is correlated with the flavor of the B hadron: an ℓ^- comes from a $b \to c\ell^-\bar{\nu}X$ transition, while an ℓ^+ originates from a $\bar{b}$ quark. Second, the charge of a $K^\pm$ from the subsequent charm decay $c \to sX$ is also correlated with the B flavor: a K^- results from the decay chain $b \to c \to s$ while a K^+ signals a $\bar{b}$ flavor. Searching for a charged kaon from the other B hadron decay is usually referred to as "kaon tagging." Third, a method called "jet charge tagging" exploits the fact that the sign of the momentum-weighted sum of the particle charges of the opposite side b jet is the same as the charge of the b quark producing this jet. Finally, the flavor of a B meson can also be tagged on the same side as the B meson of interest, by exploiting correlations of the B flavor with the charge of particles produced in association with the B meson. Such correlations are expected to arise from B quark hadronization and from B^{**} decays. We call this method "same side tagging." CDF has results on opposite side lepton tagging, jet charge tagging, and same side tagging, but has not studied kaon tagging due to the lack of particle identification at CDF. These tagging methods

are described in more detail in the following sections, where they are applied in different $B^0\bar{B}^0$ mixing measurements.

The figure of merit used to compare the "tagging power" of different flavor tags is the so-called effective tagging efficiency $\varepsilon\mathcal{D}^2$, where ε is the efficiency of how often a flavor tag is applicable. The dilution $\mathcal{D}$ is defined as the number of correctly tagged events N_R minus the number of incorrectly identified events N_W divided by the sum:

$$\mathcal{D} = \frac{N_R - N_W}{N_R + N_W} \,. \tag{49}$$

To quantify the tagging power with the expression "dilution" can be misleading. A flavor tag which always tags correctly has a dilution of 1, while a flavor tag giving the correct tag 50% of the time has a dilution of 0. This means that a tagging algorithm with a large dilution is desirable, while a small dilution characterizes a less powerful tagging method. The dilution is also related to the probability p_R that the flavor tag is correct and to the mistag probability $p_W = 1 - p_R$ that the flavor tag is incorrect:

$$\mathcal{D} = 2p_R - 1 = 1 - 2p_W \,. \tag{50}$$

To illustrate the statistical significance of the product $\varepsilon\mathcal{D}^2$, we discuss an asymmetry measurement on a data sample with N events, where the flavor tagging method identifies whether the event is of type a or type b. Type a and type b could, for example, be "mixed" and "unmixed" decays of a neutral B meson. The measured asymmetry, $\mathcal{A}_{\rm meas}$, is

$$\mathcal{A}_{\rm meas} = \frac{N_a - N_b}{N_a + N_b} \,, \tag{51}$$

where N_a and N_b are the number of events that are tagged as type a and type b, respectively. The true asymmetry, $\mathcal{A}_{\rm true}$, is

$$\mathcal{A}_{\rm true} = \frac{N_a^t - N_b^t}{N_a^t + N_b^t} \,, \tag{52}$$

where N_a^t and N_b^t are the true number of events of type a and type b in the sample. The efficiency is simply

$$\varepsilon = \frac{N_a + N_b}{N_a^t + N_b^t} \,. \tag{53}$$

It follows, from the definition of the dilution, that the true asymmetry and the measured asymmetry are related by $\mathcal{A}_{\rm true} = \mathcal{A}_{\rm meas}/\mathcal{D}$, and the statistical error on the true asymmetry is

$$\sigma(\mathcal{A}_{\rm true}) = \sqrt{\frac{1 - \mathcal{D}^2\mathcal{A}_{\rm true}^2}{\varepsilon\mathcal{D}^2 N}} \,, \tag{54}$$

where N is the total number of events in the sample $N = N_a^t + N_b^t$. The product $\varepsilon\mathcal{D}^2 N$ is the effective statistics of the data sample, i.e. it is the equivalent number of perfectly tagged events. The statistical power of different flavor tagging methods varies as $\varepsilon\mathcal{D}^2$.

7.1.3. *Outline of $B^0\bar{B}^0$ mixing measurements at CDF*

All $B^0\bar{B}^0$ mixing measurements at CDF are based on lepton data samples where the charge of the lepton determines the B flavor at decay, assuming that it originates from a semileptonic B decay. The B flavor at production is determined by an opposite side lepton tag, a jet-charge tag, or a same side tag in the various analyses described in the next sections. The proper time at decay is determined from the B decay vertex, inferred from partially reconstructed B mesons or inclusive vertices. To illustrate the effects discussed above, we consider a mixing measurement where an opposite side lepton identifies the B flavor at production.

We start with a pure sample of B^0 mesons and assume that the lepton tag is always correct. In this case, an event with an opposite-sign lepton pair signals an unmixed event, while a like-sign lepton pair indicates a mixed event. The probabilities for an opposite-sign event $\mathcal{P}_{\rm OS}$ and a like-sign event $\mathcal{P}_{\rm LS}$ are directly related to the mixing probabilities

$$\mathcal{P}_{\rm LS}(t) = \mathcal{P}_{\rm mix}(t)\,, \qquad \mathcal{P}_{\rm OS}(t) = \mathcal{P}_{\rm unmix}(t)\,, \tag{55}$$

which are defined as

$$\mathcal{P}_{\rm unmix/mix}(t) = 1/2\Gamma e^{-\Gamma t}(1 \pm \cos\Delta m t)\,. \tag{56}$$

To illustrate this behavior, we plot in Fig. 36(a) the asymmetry

$$\mathcal{A}_{\rm mix} = \frac{\mathcal{P}_{\rm OS} - \mathcal{P}_{\rm LS}}{\mathcal{P}_{\rm OS} + \mathcal{P}_{\rm LS}} = \cos\Delta m t\,, \tag{57}$$

which in this case is a pure cosine-like oscillation. We have chosen $\Delta m = 5$. Next, we introduce a vertexing resolution which smears the decay time measurement and effectively reduces the amplitude of the oscillation as shown in Fig. 36(b). The effect of introducing a momentum resolution, for example through a K factor distribution $\mathcal{H}(K)$ in the case of a partially reconstructed decay, is displayed in Fig. 36(c). Since the uncertainty on the $\beta\gamma$ resolution scales with proper time t, as seen in Eq. (48), the oscillation damps with proper time. In the case of a Gaussian vertexing resolution $\mathcal{G}$ and a momentum resolution expressed through $\mathcal{H}(K)$, the mixing probability would be modified as

$$\mathcal{P}_{\rm mix}(t) = \int dK\, \mathcal{H}(K)\big[1/2K\Gamma e^{-K\Gamma t'}(1 - \cos\Delta m K t')\big] \otimes \mathcal{G}(t'\,|\,t,\sigma)\,. \tag{58}$$

$\mathcal{P}_{\rm mix}$ would be modified accordingly.

If the lepton tag in our example does not always tag correctly but with a mistag probability p_W, we would measure the following like-sign and opposite-sign fractions:

$$\begin{aligned} \mathcal{P}_{\rm LS}(t) &= (1-p_W)\mathcal{P}_{\rm mix}(t) + p_W\mathcal{P}_{\rm unmix}(t)\,, \\ \mathcal{P}_{\rm OS}(t) &= p_W\mathcal{P}_{\rm mix}(t) + (1-p_W)\mathcal{P}_{\rm unmix}(t)\,. \end{aligned} \tag{59}$$

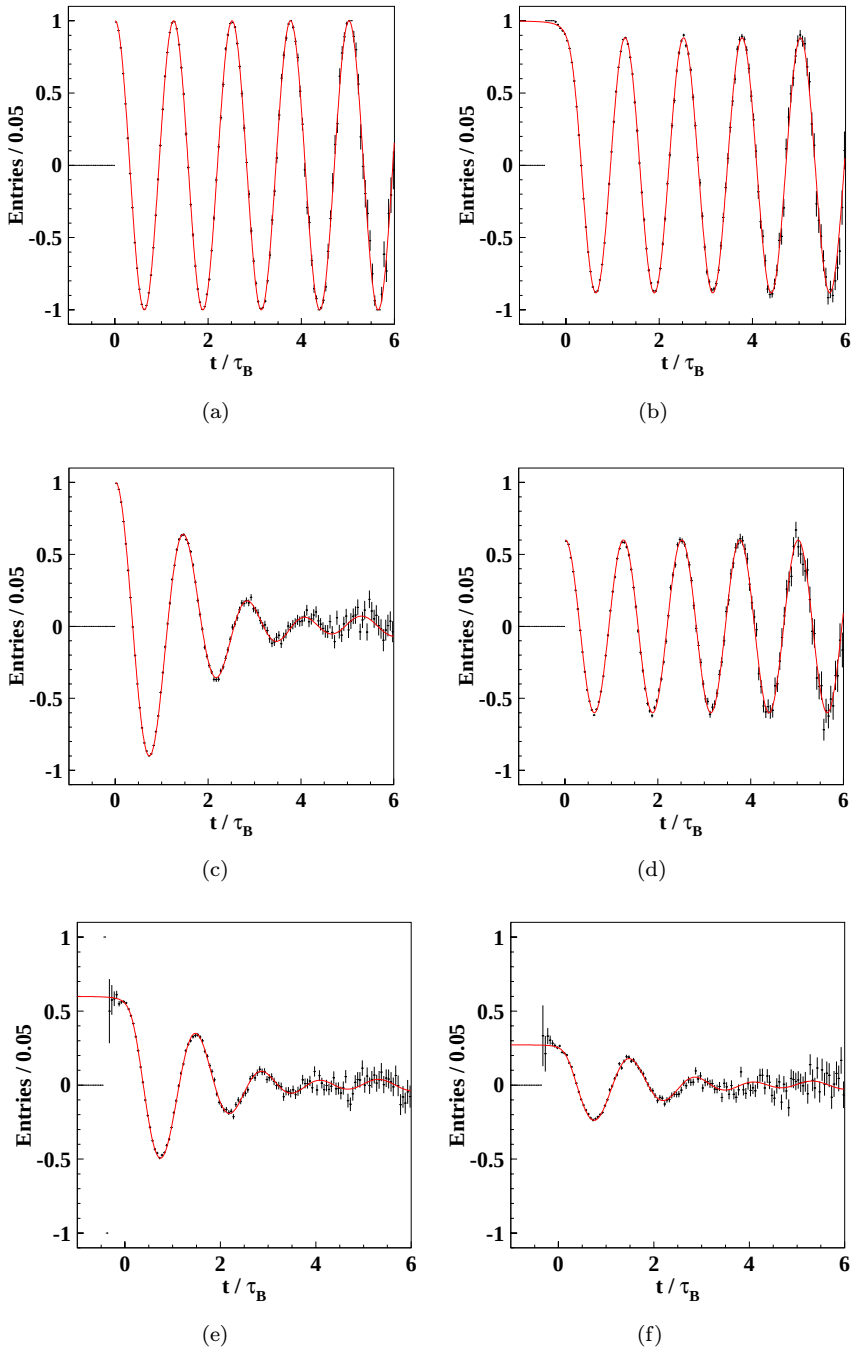

Fig. 36. Illustration of various effects on the asymmetry $\mathcal{A}_{\rm mix}$: (a) perfect resolution, (b) vertex resolution, (c) momentum resolution, (d) mistag probability, (e) vertex and momentum resolution plus mistag probability, and (f) vertex and momentum resolution plus mistag including combinatorial background.

The effect of a mistag probability p_W is shown in Fig. 36(d), while the combined effects of vertexing plus momentum resolution, together with a mistag probability, are displayed in Fig. 36(e). In a real measurement there will be background such as combinatorial background under a charm signal. We define $\mathcal{P}_{\rm LS}^{\rm sig}$ and $\mathcal{P}_{\rm OS}^{\rm sig}$ as $\mathcal{P}_{\rm LS}$ and $\mathcal{P}_{\rm OS}$ as in Eq. (59) and obtain

$$\begin{aligned}\mathcal{P}_{\rm LS}(t) &= (1-f_{\rm bg})\mathcal{P}_{\rm LS}^{\rm sig}(t) + f_{\rm bg} f_{\rm LS}\mathcal{P}^{\rm bg}(t)\,,\\ \mathcal{P}_{\rm OS}(t) &= (1-f_{\rm bg})\mathcal{P}_{\rm OS}^{\rm sig}(t) + f_{\rm bg}(1-f_{\rm LS})\mathcal{P}^{\rm bg}(t)\,.\end{aligned} \tag{60}$$

Here, $f_{\rm bg}$ is the fraction of background in a given sample, $f_{\rm LS}$ is the fraction of like-sign events in the background, while $\mathcal{P}^{\rm bg}$ is the probability function to describe the behavior of the background versus proper time t. The effect of a background on the asymmetry, in addition to a vertexing and momentum resolution, as well as a mistag rate, are shown in Fig. 36(f) and exhibit a distribution as can be expected in a real measurement. Some measurements demonstrate the time dependence of $B\bar{B}$ oscillations by plotting the so-called mixed fraction

$$\mathcal{F}_{\rm mix}(t) = \frac{\mathcal{P}_{\rm LS}}{\mathcal{P}_{\rm OS}+\mathcal{P}_{\rm LS}} = \frac{1}{2}\,(1-\cos\Delta m t)\,, \tag{61}$$

which exhibits a sinusoidal behavior with $\mathcal{F}_{\rm mix}(0)=0$.

In summary, note that a measurement of the time dependence of $B\bar{B}$ oscillations is similar to a B lifetime measurement, the difference being that the entire sample is divided into a mixed sample and an unmixed sample. In the following section we review some of the $B^0\bar{B}^0$ mixing results at CDF. These measurements are an excellent proof that B flavor tagging works in a hadron collider environment. Besides a measurement of Δm they allow, at the same time, the determination of the effective tagging efficiency $\varepsilon\mathcal{D}^2$ of the applied flavor tag. The frequency of the oscillation will determine Δm, while the amplitude characterizes $\mathcal{D}$.

7.2. $B^0\bar{B}^0$ mixing using same side tagging

The measurement of the $B^0\bar{B}^0$ oscillation frequency Δm_d, using a same side tagging technique[31,52] (SST), is based on partially reconstructed semileptonic B decays to $D^{(*)}\ell\nu X$. The lepton charge tags the B flavor at decay time, while a same side tag provides the B flavor at production. It has been suggested[53] that the electric charge of particles produced near a B meson can be used to determine its initial flavor. This can be understood in a simplified picture of fragmentation as shown in Fig. 37(a). For example, if a b quark combines with a $\bar{u}$ quark to form a B^- meson, the remaining u quark may combine with a $\bar{d}$ quark to form a π^+. Similarly, if a b quark hadronizes to form a $\bar{B}^0$ meson, the associated pion would be a π^-. Another source of correlated pions is decays of the orbitally excited ($L=1$) B mesons (B^{**}),[54] $B^{**0}\to B^{(*)+}\pi^-$ or $B^{**+}\to B^{(*)0}\pi^+$ (see also Subsec. 7.2.1). Here, no attempt is made to distinguish the hadronization pions from those originating from B^{**} decays.

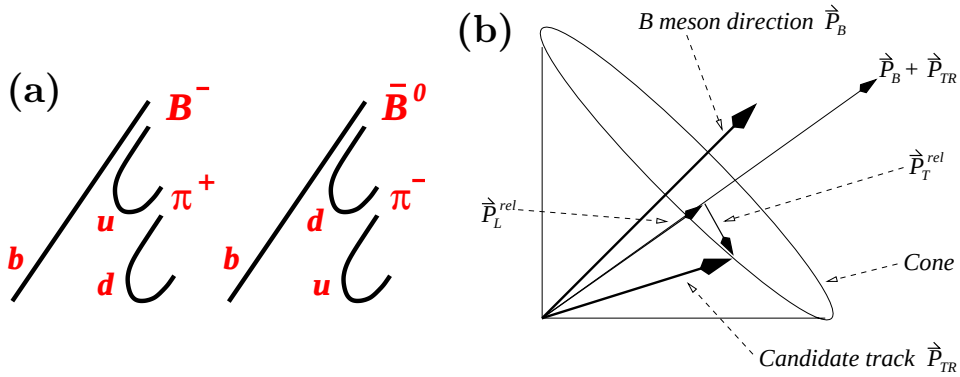

Fig. 37. (a) A simplified picture of b quark fragmentation. (b) Schematic drawing of the momentum vectors determining the $p_t^{\rm rel}$ of a same side tagging track candidate.

As in the B lifetime analysis with partially reconstructed B mesons (see Subsec. 6.4.2), B candidates are reconstructed using the decay chains $B^0 \to D^{(*)-}\ell^+\nu$, with $D^- \to K^+\pi^-\pi^-$, or $D^{*-} \to \bar{D}^0\pi_*^-$ followed by $\bar{D}^0$ decaying to $K^+\pi^-$, $K^+\pi^-\pi^+\pi^-$, or $K^+\pi^-\pi^0$, where π_*^- denotes the low-momentum (soft) pion from the D^{*-} decay. Charged B mesons are reconstructed through $B^+ \to \bar{D}^0\ell^+\nu$, with $\bar{D}^0 \to K^+\pi^-$, where the $\bar{D}^0$ is required not to form a D^{*-} candidate with any other π candidate in the event. The mass distributions of the four decay signatures with fully reconstructed D mesons are shown in Figs. 38(a)–38(c), while the distribution of $m(K\pi\pi_*) - m(K\pi)$ for the signature with $D^{*-} \to \bar{D}^0\pi_*^-$, followed by $\bar{D}^0 \to K^+\pi^-\pi^0$ (the π^0 is not reconstructed), is displayed in Fig. 38(d).

To select the SST pion, all tracks within a cone of radius 0.7 in $\eta\varphi$ space, centered around the direction of the B meson, approximated by $\mathbf{p}(\ell) + \mathbf{p}(D)$, are considered [see Fig. 37(b)]. SST candidate tracks should originate from the B production point (the primary event vertex), and are therefore required to satisfy $d_0/\sigma_{d_0} < 3$, where σ_{d_0} is the uncertainty on the track impact parameter d_0. String fragmentation models[55] indicate that particles produced in the b quark hadronization chain have low momenta transverse to the direction of the b quark momentum. We thus select as the tag the track that has the minimum component of momentum, $p_t^{\rm rel}$, orthogonal to the momentum sum of the track and the B meson [see Fig. 37(b)]. The tagging efficiency, ε, is defined as the fraction of B candidates with at least one track satisfying the above requirements. It is measured as $\varepsilon \sim 70\%$, independent of the decay signature used. On average, there are about 2.2 SST candidate tracks per B candidate.

For each of the five decay signatures, the B candidates are subdivided into six bins in proper decay length, ct, and the B-π combinations are classified as right-sign (RS: $B^+\pi^-$ and $B^0\pi^+$) or wrong-sign (WS: $B^+\pi^+$ and $B^0\pi^-$). In addition, the asymmetry in the RS and WS combinations is formed, $\mathcal{A}(ct) \equiv [N_{\rm RS}(ct) - N_{\rm WS}(ct)]/[N_{\rm RS}(ct) + N_{\rm WS}(ct)]$. For B^+ mesons, we expect an asymmetry

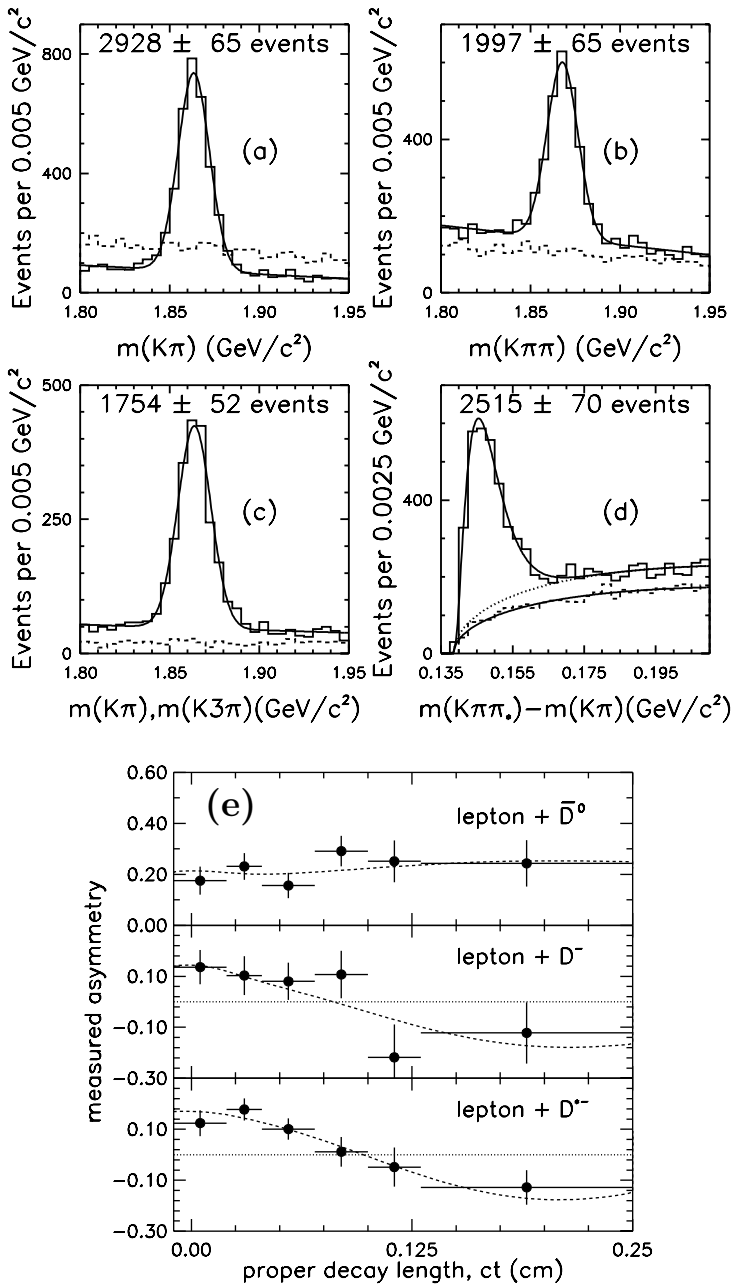

Fig. 38. *Left*: Invariant mass distributions of the five $B \to D^{(*)}\ell^+\nu X$ signatures used in the analysis: (a) $\bar{D}^0 \to K^+\pi^-$ in $\bar{D}^0\ell^+X$, (b) $D^- \to K^+\pi^-\pi^-$ in $D^-\ell^+X$, (c) $D^{*-} \to \bar{D}^0\pi^-$ with $\bar{D}^0 \to K^+\pi^-$ and $\bar{D}^0 \to K^+\pi^-\pi^+\pi^-$ in $D^{*-}\ell^+X$, (d) $K^+\pi^-\pi_*^-$ minus $K^+\pi^-$ mass difference for $D^{*-} \to \bar{D}^0\pi_*^-$ with $\bar{D}^0 \to K^+\pi^-\pi^0$ in $D^{(*)-}\ell^+X$. (e) Measured asymmetries as a function of proper decay length for the decay signatures: $\bar{D}^0\ell^+$ (top), $D^-\ell^+$ (middle), and the sum of all three $D^{*-}\ell^+$ (bottom). The dashed lines are the results of the fit.

independent of ct: $\mathcal{A}_+(ct) = \text{const} \equiv \mathcal{D}_+$. The dilution $\mathcal{D}_+$ is a direct measure of the SST purity, where $(1+\mathcal{D})/2$ is the fraction of correctly tagged events. Due to $B^0\bar{B}^0$ mixing, $\mathcal{A}_0(ct)$ for the neutral B mesons will vary as a function of ct. It follows from Eq. (57) that the asymmetry is expected to oscillate as $\mathcal{A}_0(ct) = \mathcal{D}_0 \cdot \cos\Delta m_d t$. Mistags result in a decrease of the oscillation amplitude by the dilution factor $\mathcal{D}_0$. The asymmetry is measured as a function of the proper decay length ct for both B^+ and B^0 mesons, and fit with the expected time dependence, obtaining Δm_d, $\mathcal{D}_0$ and $\mathcal{D}_+$.

The measured asymmetries $\mathcal{A}^{\text{meas}}(ct)$ are shown in Fig. 38(e). If the $\ell^+\bar{D}^0$ and $\ell^+D^{(*)-}$ signatures are pure signals of B^+ and B^0 decays, Δm_d could simply be extracted using the time dependence of $\mathcal{A}_0(ct)$. However, the signatures are mixtures of B^+ and B^0 decays, and thus $\mathcal{A}^{\text{meas}}(ct)$ is a linear combination of the true asymmetries $\mathcal{A}_0(ct)$ and $\mathcal{A}_+(ct)$. To extract Δm_d, $\mathcal{D}_0$ and $\mathcal{D}_+$, it is necessary to determine the sample composition of each $D^{(*)}\ell^+$ signature, which is the fraction of $D^{(*)}\ell^+$ candidates originating from the decays of the B^0 and B^+ mesons. Because a B^+ is associated with a π^-, whereas an unmixed B^0 is associated with a π^+, the observed asymmetries are reduced by cross-contamination which can arise if the soft pion π_*^- from the D^{*-} decay is not identified. The decay sequence $B^0 \to D^{*-}\ell^+\nu$ will be reconstructed as $\ell^+\bar{D}^0$, i.e. as a B^+ candidate. Another source of cross-contamination arises from semileptonic B decays involving P-wave D^{**} resonances as well as nonresonant $D^{(*)}\pi$ pairs, which cannot be easily recognized and removed from the sample. For example, the decay sequence $B^0 \to D^{**-}\ell^+\nu$, followed by $D^{**-} \to \bar{D}^0\pi_{**}^-$ (by π_{**} we denote the pion originating from a D^{**} decay), will be reconstructed as $\ell^+\bar{D}^0$, because of the missed π_{**}^-. Again, a B^0 decay is misclassified as a B^+ candidate. The tagging is further complicated when a $\pi_{**}^\pm$ from a D^{**} decay is present. The $\pi_{**}^\pm$ may be incorrectly selected as the SST pion, always resulting in a RS correlation. The requirement $d_0/\sigma_{d_0} < 3$, described above, reduces this effect. The π_{**} originates from the B meson decay point, whereas the appropriate tagging track comes from the B meson production point.

Taking these effects properly into account, the mass difference Δm_d and the dilutions $\mathcal{D}_0$ and $\mathcal{D}_+$ are determined from a χ^2 fit to the measured asymmetries $\mathcal{A}^{\text{meas}}(ct)$ with the fit result overlaid, as shown in Fig. 38(e). The oscillation in the neutral B signatures is clearly present. The final result for the mixing frequency is

$$\Delta m_d = (0.471^{+0.078}_{-0.068} \pm 0.034)\ \text{ps}^{-1}\,. \tag{62}$$

In addition, the following values for the neutral and charged SST flavor tagging dilutions are obtained:

$$B^0:\ \mathcal{D}_0 = (18 \pm 3 \pm 2)\%\,, \quad \varepsilon\mathcal{D}_0^2 = (2.4 \pm 0.7^{+0.6}_{-0.4})\%\,, \tag{63}$$

$$B^+:\ \mathcal{D}_+ = (27 \pm 3 \pm 2)\%\,, \quad \varepsilon\mathcal{D}_+^2 = (5.2 \pm 1.2^{+0.9}_{-0.6})\%\,. \tag{64}$$

The fit indicates that $\sim$82% of the $\bar{D}^0\ell^+$ signature comes from B^+ decays, while $\sim$80% of the $D^-\ell^+$ and $\sim$95% of the $D^{*-}\ell^+$ originate from B^0. The B^0 component of the $\bar{D}^0\ell^+$ signature can be seen as a small anti-oscillation in Fig. 38(e), top.

7.2.1. *Production of B^{**} mesons*

To shed some light on the question of how much of the observed tagging power of same side tagging arises from fragmentation tracks compared to pions from B^{**} decays, we briefly discuss the production of B^{**} mesons at CDF. The term B^{**} is a collective name for the four lowest-lying $L = 1$ states of B mesons, which are usually labeled by the total angular momentum J of the light quark resulting in two doublets with $J = 1/2$ and $3/2$. The states in the $J = 1/2$ doublet are expected to be broad ($\sigma \sim 100$ MeV/c^2), since they can decay through an S wave transition, while the $J = 3/2$ states decay through a D wave transition and are therefore expected to be narrow ($\sigma \sim 20$ MeV/c^2). B^{**} states have been observed at LEP[54] with properties in reasonable agreement with the expectations.

The procedure for selecting B mesons follows the one described above in Subsec. 7.2 reconstructing semileptonic B decays into $D^{(*)}\ell\nu X$. About 5500 $D^{*+}\ell$ and $D^{+}\ell$ candidates associated with a B^0 signature and about 4200 $D^0\ell$ events indicating a B^+ signature are selected. B^{**} candidates are constructed by combining the B candidates with all tracks compatible with those originating from the primary interaction vertex. Since the resolution on the B^{**} invariant mass is impaired by the unknown momentum of the missing neutrino, a quantity $Q = m(B\pi) - m(B) - m(\pi)$ is constructed. A resolution of ~ 50 MeV/c^2 on Q is expected from B^{**} decays. Since the charge of the pion from a B^{**} decay always matches the B flavor, the sample is divided into right-sign and wrong-sign combinations. We expect an excess of RS combinations confined to $Q < 500$ MeV/c^2 corresponding to the B^{**} states.

The essential task of this analysis it to properly determine the backgrounds to the B^{**} signal. These can be divided into correlated and uncorrelated components. Three sources of uncorrelated background are taken into account: combinatorial background from fake B meson candidates, particles from the underlying event and tracks from events with multiple hard $p\bar{p}$ collisions. All three components are measured from data and subtracted from the Q distributions. The main correlated background arises from fragmentation particles which contribute to the right-sign excess. The shape of this background is predicted using Monte Carlo calculations tuned to CDF data (see Subsec. 4.5.2). To extract the B^{**} production fraction from the Q distribution, cross-contamination between B^0 and B^+ via D^{**} and B^* states is taken into account as well as the known flavor mixing of B^0 mesons.

The result of the fit to the Q distributions is shown in Fig. 39. The points are the data, the dashed curves are the fitted shapes of the hadronization component, the dotted histograms include all backgrounds, and the solid histograms are the sum including the fitted B^{**} signal. The B^{**} production fraction, defined as the probability that a B quark hadronizes into a B^{**} state, is measured as $f^{**} = 0.28 \pm 0.06 \pm 0.03$. The experimental resolution does not allow disentangling of the four B^{**} states and the average mass of the ensemble is varied collectively to obtain $m(B_1) = (5.71 \pm 0.02)$ GeV/c^2 for $m(B_1)$ of the narrowest state ($J = 3/2$).

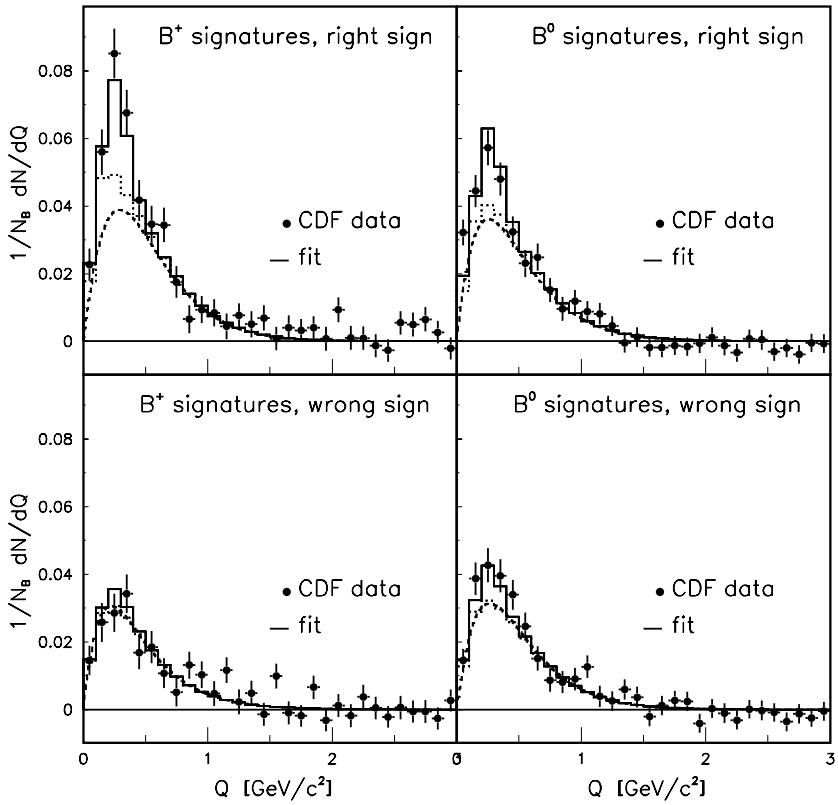

Fig. 39. Result of the fit to the Q distributions of the $B\pi$ candidates. The dashed curves are the fitted hadronization components, the dotted histograms include all backgrounds, and the solid histograms are the sum including the fitted B^{**} signal.

7.3. $B^0\bar{B}^0$ *mixing using jet charge and lepton tagging*

The analysis reported next[56] uses the same single lepton data samples as the SST mixing result but increases the number of B mesons by over an order of magnitude by inclusively reconstructing B hadrons decaying semileptonically rather than using lepton–charm correlations. The inclusive reconstruction is based on identifying the B hadron decay point by associating the trigger lepton with other B decay products to form a secondary vertex.

First, charged particle jets are reconstructed in the event using a track-based jet clustering algorithm (see Subsec. 4.4). The trigger lepton is associated with a jet. The search for the B decay point in the trigger lepton jet is based on the technique to identify b quark jets coming from top quark decays.[57] Some modifications are made to maintain good efficiency for reconstructing displaced vertices, since B hadrons in this data sample have substantially lower p_t than B hadrons from top decays. Tracks in the jet are selected for reconstructing the secondary vertex based on the significance of their impact parameter d_0/σ_{d_0} with respect to the primary vertex,

where σ_{d_0} is the estimate of the error on d_0. First, displaced vertices containing three or more tracks satisfying a loose set of track quality requirements are searched for. If no such vertices are found, two-track vertices which satisfy more stringent quality requirements are accepted and the two-dimensional decay length of the secondary vertex is calculated. To reduce background from false vertices formed from random combinations of tracks coming from the primary interaction vertex, $|L_{xy}/\sigma_{L_{xy}}| > 2.0$ is required, where $\sigma_{L_{xy}}$ is the estimated error on L_{xy}. This leaves 243,800 events: 114,665 from the electron data sample and 129,135 from the muon data sample. Secondary vertices are also searched for in the other jet in the event. If an additional displaced vertex is found, the event is classified as a "double-vertex" event.

The flavor of the B hadron producing the trigger lepton is identified using a jet charge tag and an opposite side lepton tag. First, an additional lepton (e or μ) from the semileptonic decay of the opposite side B hadron is searched for in the event. The invariant mass of this lepton and the trigger lepton must be greater than 5 GeV/c^2 to reject leptons that come from the same B hadron producing the trigger lepton. Approximately 5.2% of the 243,800 events contain an opposite side lepton. If such a lepton is not found, the jet produced by the opposite b quark is identified by calculating a quantity called the jet charge $Q_{\rm jet}$,

$$Q_{\rm jet} = \frac{\sum_i q_i \cdot (\mathbf{p}_i \cdot \hat{a})}{\sum_i \mathbf{p}_i \cdot \hat{a}}\,, \tag{65}$$

where q_i and $\mathbf{p}_i$ are the charge and momentum of track i in the jet and $\hat{a}$ is a unit vector defining the jet axis. On average, the sign of the jet charge is the same as the sign of the b quark that produced the jet. In the case of a double-vertex event the jet containing the other secondary vertex is used to calculate $Q_{\rm jet}$. About 7.5% of the sample consists of jet charge double-vertex events and 42% are jet charge single-vertex events. Figure 40 shows, on the left side, the jet charge distributions for single-vertex and double-vertex events. The degree of separation between the solid and dashed distributions is related to the tagging power of the jet charge flavor tag. For double-vertex events, the presence of the second displaced vertex increases the probability that the selected jet in fact originates from the other B hadron in the event. This translates into a significantly larger separation in the jet charge for double-vertex events.

Unlike the case of the SST mixing analysis, where a charm peak in the invariant mass spectrum indicates the amount of signal and background, the number of trigger leptons from $b\bar{b}$ production must be determined differently in this analysis. Other sources of the selected events include $c\bar{c}$ production and light quark or gluon production that can result in fake leptons or vertices. The fraction of events from false vertices and fake leptons is found to be small. The fraction of events due to $b\bar{b}$ and $c\bar{c}$ production is determined using two kinematic quantities: the trigger lepton $p_t^{\rm rel}$ and the invariant mass $m^{\rm cl}$ of the cluster of secondary vertex tracks. The quantity $p_t^{\rm rel}$ is defined as the magnitude of the component of the trigger lepton

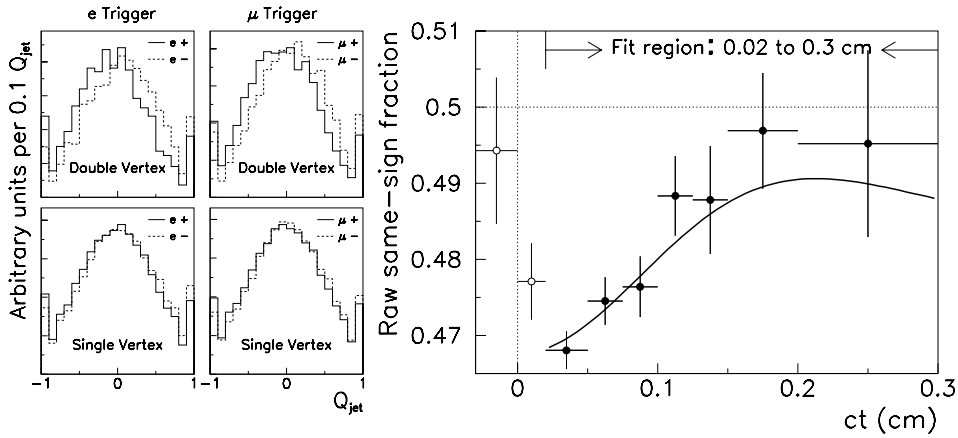

Fig. 40. *Left*: Jet charge distributions for double-vertex (top) and single-vertex (bottom) events for the e- and μ-trigger data. *Right*: Same-sign fraction as a function of proper decay length. A representation of the fit result is superimposed on the data.

momentum perpendicular to the jet axis. The trigger lepton is removed from the jet, and the jet axis is recalculated to determine $p_t^{\rm rel}$. To calculate $m^{\rm cl}$, the pion mass is assigned to all of the tracks used to form the secondary vertex (except the lepton). The trigger lepton is included in this calculation even if it is not attached to the secondary vertex. Both kinematic quantities are effective in discriminating between $b\bar{b}$ and $c\bar{c}$ events because of the significant mass difference between hadrons containing b and c quarks. Template $p_t^{\rm rel}$ and $m^{\rm cl}$ distributions are obtained from $b\bar{b}$ and $c\bar{c}$ Monte Carlo samples (see Subsec. 4.5.2) and fit to the data. The determination of the sample composition yields the data being primarily ($> 90\%$) from $b\bar{b}$ production.

According to the flavor tag and the charge of the trigger lepton, the data are divided in a like-sign and opposite-sign sample. The proper decay time of the B hadron is determined from the L_{xy} of the secondary vertex, combined with an estimate of the B momentum obtained from Monte Carlo calculations. From an unbinned maximum log-likelihood fit to the time dependence of the OS and LS sample, the B^0 oscillation frequency is determined to be

$$\Delta m_d = (0.500 \pm 0.052 \pm 0.043)\ \mathrm{ps}^{-1}\,. \tag{66}$$

The distribution of the like-sign fraction as a function of proper decay length is shown in Fig. 40 on the right hand side. A representation of the fit result is superimposed on the data. In addition, the effective tagging efficiencies of the jet charge and opposite side lepton tags are obtained:

$$\text{jet charge tag}: \quad \varepsilon\mathcal{D}^2 = (0.78 \pm 0.12 \pm 0.08)\%\,, \tag{67}$$

$$\text{lepton tag}: \quad \varepsilon\mathcal{D}^2 = (0.91 \pm 0.10 \pm 0.11)\%\,. \tag{68}$$

These values for $\varepsilon\mathcal{D}^2$ are much lower than those achieved in experiments on the Z^0 resonance.[58] On the other hand, the much higher $b\bar{b}$ cross section at the Tevatron can be used to compensate for the disadvantage in $\varepsilon\mathcal{D}^2$.

7.4. $B^0\bar{B}^0$ mixing using dilepton data

The previous analysis searches single lepton events for additional leptons used as opposite side flavor tags. However, there exist large dilepton data sets at CDF where the lepton tag has already been triggered on. These data are also used for proper-time-dependent measurements of $B\bar{B}$ oscillations. In these data sets both leptons are assumed to come from the semileptonic decay of both B hadrons in the event: $b \to \ell_1 X$ and $\bar{b} \to \ell_2 X$. This means that the flavor of the B meson at decay is tagged by its semileptonic decay, while the lepton from the semileptonic decay of the other B hadron in the event tags the B flavor at production. The requirement $m(\ell_1\ell_2) > 5$ GeV/c^2 ensures that both leptons originate from two B hadrons and not from a sequential decay of one B hadron: $b \to c\ell_1 X$, with $c \to \ell_2 X$. Here, we briefly describe two mixing results using the $e\mu$ trigger data as well as dimuon trigger events.

The analysis using $e\mu$ data[59] also searches for an inclusive secondary vertex associated with one of the leptons. As in the previous analysis in Subsec. 7.3, secondary vertices are reconstructed using a modified version of the algorithm used to find displaced vertices in the search for the top quark.[57] The decay length L_{xy} of this vertex and the momenta of the tracks associated with the lepton provide an estimate of the ct of the B meson. Again, the important task of this analysis is to determine the sample composition, the fraction of events coming from $b\bar{b}$ decays with respect to events from $c\bar{c}$ or background events. The sample composition is estimated from several kinematic quantities, like $p_t^{\rm rel}$ or the invariant mass of the tagged secondary vertex. Here, $p_t^{\rm rel}$ is defined as the transverse momentum of the lepton with respect to the highest p_t track in a cone around the lepton. The determination of the sample composition finds that more than 80% of the events originate from $b\bar{b}$ decays.

From a fit to the like-sign lepton fraction, as a function of ct, the mixing frequency Δm_d is extracted as shown in Fig. 41(a). The fit includes components for direct and sequential b decays, $c\bar{c}$, and fake events. In about 16% of the events with a secondary vertex around one lepton, a secondary vertex is also found around the other lepton. These events enter the like-sign fraction distribution twice, where we allow for a statistical correlation between the two entries. The final fit result is

$$\Delta m_d = (0.450 \pm 0.045 \pm 0.051)\ \text{ps}^{-1}\,, \tag{69}$$

where the dominant systematic error arises from the uncertainty in the sample composition.

The measurement of the $B^0\bar{B}^0$ oscillation frequency using dimuon data[60] is very similar to the $e\mu$ analysis. Here, the algorithm used to find displaced vertices around

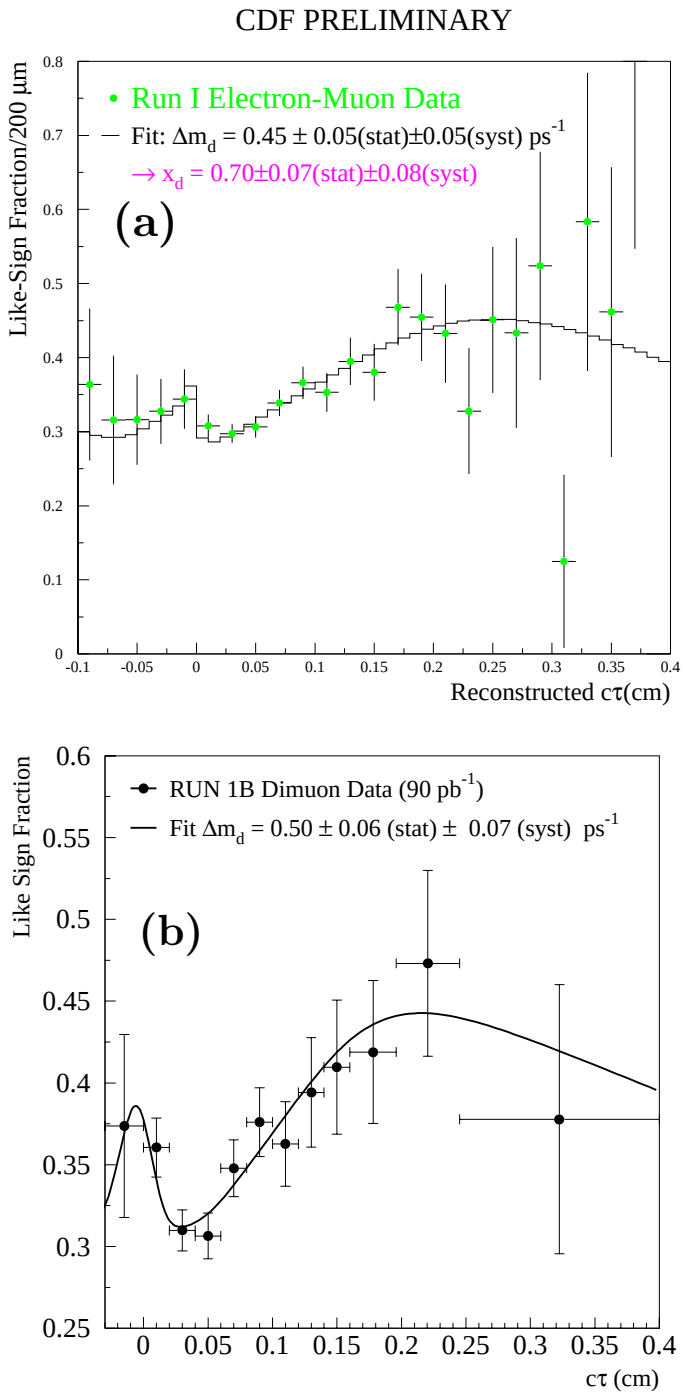

Fig. 41. Fraction of (a) like-sign $e\mu$ events and (b) like-sign dimuon events as a function of pseudo-proper decay length. The results of the Δm_d fits are superimposed.

one of the muons is based on the correlation between the impact parameter d_0 and the azimuthal angle φ of tracks coming from these vertices. A vertex is formed by three or more correlated tracks with a significance $d_0/\sigma_{d_0} > 2$. Tracks from a secondary vertex form a line in the $\varphi\, d_0$ plane with nonzero slope, while tracks from the primary interaction vertex have small d_0 values and show no correlation with φ.

The determination of the sample composition again uses different kinematic variables and finds the fraction of events from $b\bar{b}$ production to be larger than 80%. The final sample amounts to 2044 like-sign and 3924 opposite-sign dimuon events. The fraction of events with like-sign muons is shown in Fig. 41(b) as a function of proper time of the B hadron associated with the identified secondary vertex. From a χ^2 fit to the like-sign fraction, the B^0 oscillation frequency is determined to be

$$\Delta m_d = (0.503 \pm 0.064 \pm 0.071)\ \mathrm{ps}^{-1}\,, \tag{70}$$

where the main systematic error arises from the determination of the background and the fraction of muons from sequential charm decays.

7.5. $B^0\bar{B}^0$ mixing using charm decays with a lepton tag

We briefly describe two more $B^0\bar{B}^0$ mixing results[59] also using a lepton tag to identify the B flavor at production. Both preliminary analyses allow the determination of the dilution or mistag probability of the lepton tag. One analysis uses higher momentum leptons than the other, which can shed some light on the momentum dependence of the tagging dilution.

The first analysis uses the dimuon as well as $e\mu$ trigger data and searches for a charm decay around one of the leptons identifying semileptonic B decays. In particular, leptons associated with a D^{*+} meson are used as signature for B^0 decays. The D^{*+} mesons are reconstructed in the decay mode $D^{*+} \to D^0\pi^+$, followed by $D^0 \to K^-\pi^+$, $K^-\pi^+\pi^+\pi^-$ or $K^-\pi^+\pi^0$. A signal of about 500 such decays is found on low backgrounds. The decay vertices of the $D^{*+}\ell^-$ combinations are reconstructed and the proper decay length of the B^0 meson is estimated using the $D^{*+}\ell^-$ momentum. The charge of the final state identifies the B^0 flavor at decay time, while the other lepton in the event provides the B flavor at production. As in the B lifetime analysis using partially reconstructed B decays (Subsec. 6.4.2), $D^{*+}\ell^-$ combinations are a good signature for neutral B mesons, but D^{**} decays allow a contamination of charged B decays into the $D^{*+}\ell^-$ sample, diluting the charge correlation between the final states and the parent B meson. Using Monte Carlo techniques as in Subsec. 6.4.2, the cross contamination from B^+ decays is found to be $0.19^{+0.08}_{-0.10}$ for the $D^{*+}\mu^-$ sample and $0.14^{+0.06}_{-0.08}$ for the $D^{*+}e^-$ sample.

The signal sample is divided into OS and LS events and the corresponding asymmetry distribution is shown in Fig. 42(a). From the time dependence of the OS and LS sample, the B^0 oscillation frequency Δm_d and the mistag probability

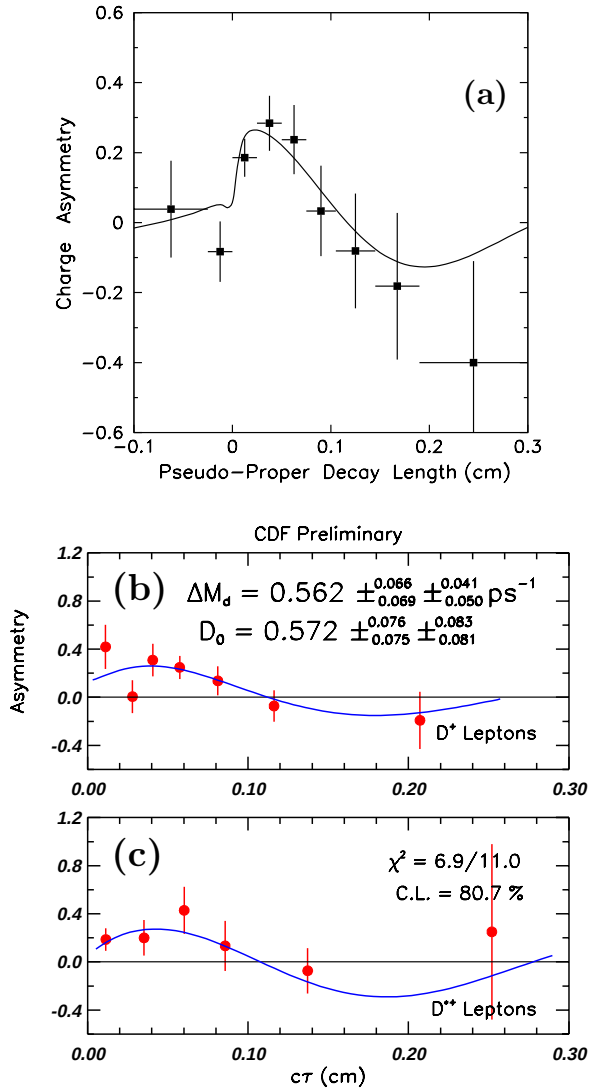

Fig. 42. Asymmetry distribution of (a) $D^{*+}\ell^-$ candidates, (b) D^- candidates, and (c) D^{*-} candidates as a function of proper decay length. The points are the data and the curves show the result of the Δm_d fits.

p_W of the lepton tag are simultaneously extracted. The unbinned log-likelihood fit yields

$$\Delta m_d = \left(0.516 \pm 0.099^{+0.029}_{-0.035}\right)\ \mathrm{ps}^{-1}\,, \tag{71}$$

while the flavor misidentification probability is $p_W = 0.325 \pm 0.033^{+0.005}_{-0.010}$, yielding a dilution of the lepton tag of $\mathcal{D} = 0.35 \pm 0.07$.

The second analysis uses the trigger lepton from the single lepton trigger data as the B flavor tag. The transverse momentum of these leptons is greater than 8 GeV/c, in comparison to the dilepton data where $p_t(\ell)$ is greater than about 2 GeV/c. The B^0 meson is inferred from a $D^{(*)-}$ decay opposite the trigger lepton, where the charge of the $D^{(*)-}$ meson tags the B^0 flavor at decay. This means that this analysis searches for events with $b \to \ell^- X$ and $\bar{b} \to B^0 \to D^{(*)-} X$. A $\ell^- D^{(*)-}$ combination is therefore a signature for an unmixed event, while a $\ell^+ D^{(*)-}$ pair signals a mixed event. $D^{(*)-}$ candidates are reconstructed as $D^- \to K^+\pi^-\pi^-$ and $D^{*-} \to \bar{D}^0\pi^-$, with $\bar{D}^0 \to K^+\pi^-$. The decay length of the charm meson provides an estimate of the B^0 decay time together with the measurement of $p_t(D^{(*)-})$ used to infer $p_t(B^0)$.

Signals of (460 ± 31) D^- events and (358 ± 32) D^{*-} events are selected. The $D^{(*)-}$ mesons may originate from $b\bar{b}$ and $c\bar{c}$ production. In addition, cross-contamination of $D^{(*)-}$ mesons from charged B mesons via D^{**} decays must be considered, as discussed above and in Subsec. 6.4.2. Using MC techniques and fits to kinematic variables, it is found that approximately 65% of the signal sample comes from B^0 decays, $\sim 20\%$ from B^+, and $\sim 15\%$ from $c\bar{c}$ production. The time-dependent asymmetry distribution of $\ell^+ D^{(*)-}$ and $\ell^- D^{(*)-}$ pairs is plotted in Fig. 42(b) for D^- (top) and D^{*-} (bottom). The fit for the B^0 mixing frequency results in

$$\Delta m_d = \left(0.562 \pm 0.068^{+0.041}_{-0.050}\right)\ \mathrm{ps}^{-1}\,, \tag{72}$$

while the dilution of the lepton tag is determined to be $\mathcal{D} = 0.572 \pm 0.080^{+0.083}_{-0.081}$.

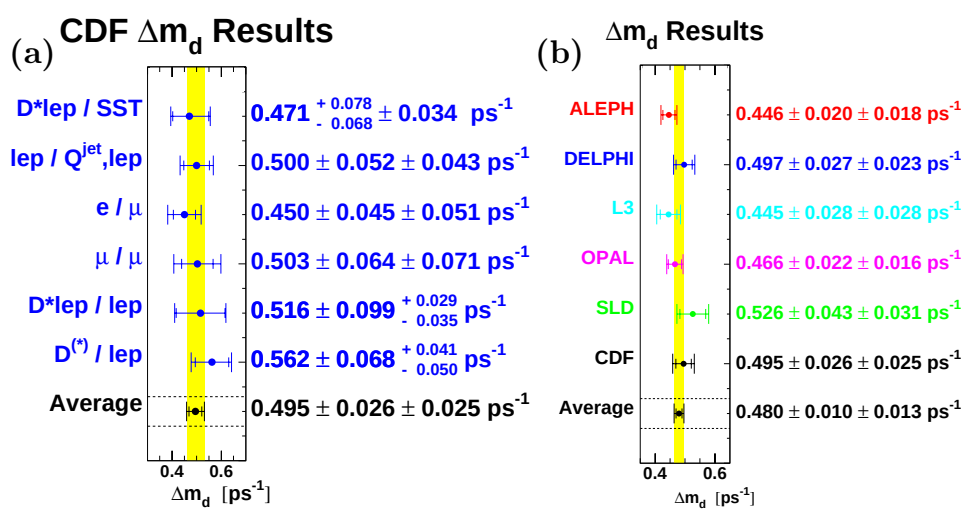

Fig. 43. Compilation of (a) the CDF time-dependent $B^0\bar{B}^0$ mixing measurements and (b) the Δm_d average results for the LEP, SLD and CDF experiments as of July 1998.

7.6. *Summary of $B^0\bar{B}^0$ mixing measurements*

A compilation of all Δm_d measurements at CDF is found in Fig. 43(a). We use these measurements to determine a CDF average result for Δm_d. Since the measurements of Δm_d are quite precise, it is important to correctly take the correlated systematic uncertainties into account in forming the average. In addition, most of the presented results depend on common physics parameters, where different values are used in the original analyses. In order to correctly handle these issues, we use the procedure developed by the LEP B Oscillation Working Group and adjust the measurements of Δm_d on the basis of a common consistent set of input values. First, the procedure linearly rescales each measurement of Δm_d for each common physics parameter, in accordance with the difference between the originally used parameter value and its new common value, and with the corresponding systematic uncertainty determined in the analysis. This systematic uncertainty is also adjusted, if the uncertainty on the parameter is different from that originally used. The combination procedure then performs a common fit of Δm_d and of the physics parameters related to the sources of the common systematic uncertainties. We also take into account a statistical correlation of about 20% between the Δm_d result using jet charge and lepton tagging and the Δm_d analyses using dilepton data. We determine the average of all Δm_d results at CDF to be

$$\Delta m_d = (0.495 \pm 0.026 \pm 0.025)\ \mathrm{ps}^{-1}\,. \tag{73}$$

A comparison of this CDF average with the Δm_d averages of the LEP and SLD experiments as of July 1998 is displayed in Fig. 43(b). The CDF Δm_d results are quite competitive with other experiments.

8. Search for CP Violation

In 1964, Christenson, Cronin, Fitch and Turlay discovered[61] that the laws of nature are not invariant under the combined action of charge conjugation C and parity P. They found that the K_L^0 meson, associated with the CP-odd state in the neutral kaon system, decays with a branching fraction of about $2 \cdot 10^{-3}$ into $\pi^+\pi^-$, which is a CP-even state. This result can briefly be illustrated in the following way. As in the B meson system, discussed in Subsecs. 6.5.3 and 7.1, neutral kaons exist in two CP-conjugate flavor states $|K^0\rangle = |\bar{s}d\rangle$ and $|\bar{K}^0\rangle = |s\bar{d}\rangle$. Applying the CP operation to these states, we define the following phase convention:

$$CP|K^0\rangle = -|\bar{K}^0\rangle\,, \qquad CP|\bar{K}^0\rangle = -|K^0\rangle\,. \tag{74}$$

The physical kaon states with well-defined mass and lifetime, which decay through the weak interaction, are linear combinations of the two CP-conjugate quark states:

$$|K_1^0\rangle = 1/\sqrt{2}(|K^0\rangle - |\bar{K}^0\rangle)\,, \quad |K_2^0\rangle = 1/\sqrt{2}(|K^0\rangle + |\bar{K}^0\rangle)\,. \tag{75}$$

If CP is conserved, the physical kaon states are CP eigenstates:

$$CP|K_1^0\rangle = CP[1/\sqrt{2}(|K^0\rangle - |\bar{K}^0\rangle)] = 1/\sqrt{2}(-|\bar{K}^0\rangle + |K^0\rangle) = +|K_1^0\rangle\,. \tag{76}$$

We call K_1^0 the "CP-even" state. For K_2^0, we obtain

$$CP|K_2^0\rangle = CP[1/\sqrt{2}(|K^0\rangle + |\bar{K}^0\rangle)] = 1/\sqrt{2}(-|\bar{K}^0\rangle - |K^0\rangle) = -|K_2^0\rangle \tag{77}$$

and call K_2^0 the "CP-odd" state. From experiment, we know that neutral kaons decay into either two or three pions. Since $CP\,|\pi^+\pi^-\rangle = +1$ and $CP|\pi^+\pi^-\pi^0\rangle = -1$, we associate $|K_1^0\rangle$ with $K_S^0 \to \pi^+\pi^-$ and $|K_2^0\rangle$ with $K_L^0 \to \pi^+\pi^-\pi^0$. If CP is conserved, a K_L^0 is not allowed to decay into two pions. The discovery of K_L^0 decays into $\pi^+\pi^-$ thus manifests the existence of CP violation and states that the laws of nature are not exactly the same for matter and antimatter.

More than 30 years have passed since the surprising discovery of CP violation, and the kaon system is still the only place where CP violation has been observed in nature. However, the system of neutral B mesons is expected to yield large CP-violating effects. This is the subject of this section, where we report on a search for CP violation in $B^0 \to J/\psi K_S^0$ decays at CDF. First, we briefly introduce the Cabibbo–Kobayashi–Maskawa mixing matrix and the CKM unitarity triangle.

8.1. *CKM matrix and unitarity triangle*

CP violation in the kaon system can be explained in an elegant way in the Standard Model[4] with three generations, as originally suggested by Kobayashi and Maskawa[6] in 1973. Note that this was still before the discovery of the J/ψ resonance[62] in 1974. In the Standard Model with SU(2)×U(1) as the gauge group of electroweak interactions, the quark mass eigenstates are not the same as the weak flavor eigenstates. The matrix which relates the mass eigenstates to the weak eigenstates was defined for six quarks and given an explicit parametrization by Kobayashi and Maskawa.[6] It generalizes the four-quark case, where the corresponding matrix is parametrized by a single parameter, the Cabibbo angle.[5] The mixing is often expressed in terms of a 3×3 unitarity matrix $V_{\rm CKM}$, called the Cabibbo–Kobayashi–Maskawa mixing matrix, which operates by convention on the charge $-1/3$ quarks d, s and b:

$$\begin{pmatrix} d' \\ s' \\ b' \end{pmatrix} = \begin{pmatrix} V_{ud} & V_{us} & V_{ub} \\ V_{cd} & V_{cs} & V_{cb} \\ V_{td} & V_{ts} & V_{tb} \end{pmatrix} \begin{pmatrix} d \\ s \\ b \end{pmatrix} . \tag{78}$$

The individual matrix elements can, in principle, all be determined from weak decays of the relevant quarks or from deep inelastic neutrino scattering.

There are several parametrizations of the CKM matrix. In the standard parametrization, three rotation angles and an imaginary phase must be used. This phase being nonzero gives rise to CP violation in the weak interaction. Another popular approximation of the CKM matrix which emphasizes the hierarchy in the size of the matrix elements is due to Wolfenstein:[63]

$$V_{\rm CKM} = \begin{pmatrix} 1-\lambda^2/2 & \lambda & A\lambda^3(\rho - i\eta) \\ -\lambda & 1-\lambda^2/2 & A\lambda^2 \\ A\lambda^3(1-\rho-i\eta) & -A\lambda^2 & 1 \end{pmatrix} + \mathcal{O}(\lambda^4)\,. \tag{79}$$

Here, the CKM matrix is parametrized in powers of λ, the sine of the Cabibbo angle $\lambda = \sin\theta_c = |V_{us}|$. The Cabibbo angle is well measured from leptonic kaon decays $K \to \pi\ell\nu$, yielding $\lambda = 0.2196 \pm 0.0023$. The other parameters used in the Wolfenstein parametrization are A, ρ and η. The parameter A is related to the CKM matrix element $V_{cb} = A\lambda^2$ and can be determined from semileptonic $b \to c$ transitions. As we will see below, the parameters ρ and η are related to CP violation in the B meson system and are connected to the matrix elements V_{ub} and V_{td}.

Because of the unitarity of the CKM matrix derived from conserving probabilities, we obtain a relation involving the two smallest elements V_{ub} and V_{td} of $V_{\rm CKM}$:

$$V_{ud}V_{ub}^* + V_{cd}V_{cb}^* + V_{td}V_{tb}^* = 0\,. \tag{80}$$

This is a triangle relation in the complex plane as shown in Fig. 44(a). The Cabibbo–Kobayashi–Maskawa matrix elements determine the size of the legs of this triangle, often called the CKM unitarity triangle. The angles α, β and γ are related to CP-violating asymmetries in B decays. For example, an asymmetry in $B^0 \to J/\psi K_S^0$ decays measures $\sin 2\beta$, while $B^0 \to \pi\pi$ decays are related to $\sin 2\alpha$. For CP violation to be permitted in the Standard Model, the area of the unitarity triangle must be nonzero and the angles of the triangle different from zero or π.

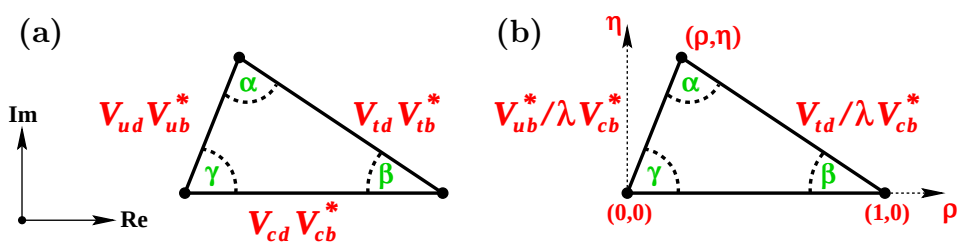

Fig. 44. The CKM unitarity triangle (a) in standard representation and (b) in the (ρ, η) plane using the Wolfenstein parametrization.

We briefly illustrate the current knowledge about the CKM unitarity triangle. For this purpose, we use the Wolfenstein parametrization, where the unitarity triangle is described in the (ρ, η) plane, as shown in Fig. 44(b). We make the approximations $|V_{tb}^*| = 1$, $V_{cd} = -\lambda$, and set $V_{ud} = 1 - \lambda^2/2 \approx 1$. We also normalize the legs of the triangle by $|V_{cb}|$ keeping the base of the triangle of unit length. The other two legs are then described by $|V_{ub}^*/\lambda V_{cb}^*|$ and $|V_{td}/\lambda V_{cb}^*|$. A measurement of $|V_{ub}/V_{cb}|$ constrains one leg of the triangle to lie between the two half circles centered at the origin, as shown in Fig. 45. The other leg of the triangle is constrained by our current knowledge of V_{td} obtained from $B^0\bar{B}^0$ mixing measurements. The large uncertainty with which the B meson decay constant f_B and the bag parameter (see Subsec. 7.1) are known, allows this leg of the unitarity triangle to lie in the broad area between the two circles centered around the point $(1, 0)$. Finally, the knowledge of CP violation in the kaon system adds another constraint to the CKM unitarity triangle indicated by the third band in Fig. 45. We fit the three bands to

originate from a common area and obtain the 95% confidence level contour, also shown in Fig. 45. We see that the apex of the unitarity triangle, described by the coordinates (ρ, η), can be placed in a fairly wide range. Direct measurements of the angles α, β or γ would better constrain the CKM unitarity triangle.

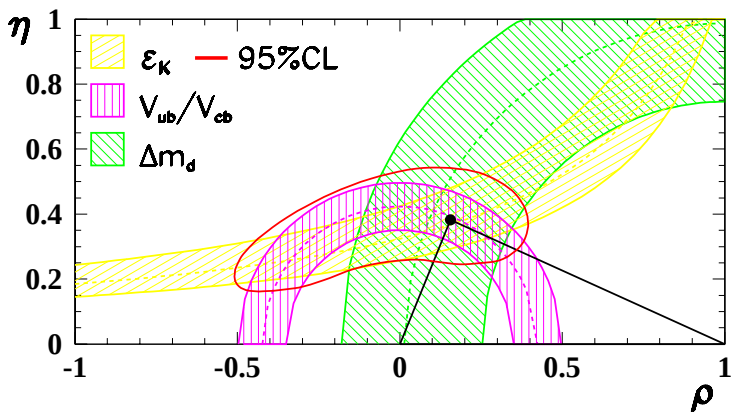

Fig. 45. Constraints on the (ρ, η) plane arising from measurements of $|V_{ub}/V_{cb}|$, $B^0\bar{B}^0$ mixing (Δm_d), and CP violation in kaon decays (ϵ_K).

8.2. *Measurement of the CP violation parameter* $\sin 2\beta$ *in* $B^0 \to J/\psi K_S^0$

One way to observe CP violation in B meson decays is to use the interference between the direct decay of a B^0 into a CP final state f_{CP} and the process $B^0 \to \bar{B}^0 \to f_{CP}$, which can provide a second amplitude to interfere with the direct decay $B^0 \to f_{CP}$. A large CP-violating effect is expected[64] in $B^0/\bar{B}^0$ decays to the CP eigenstate $J/\psi K_S^0$. The interference of direct decays, $B^0 \to J/\psi K_S^0$, versus those that undergo mixing, $B^0 \to \bar{B}^0 \to J/\psi K_S^0$, gives rise to a decay asymmetry:

$$\mathcal{A}_{CP}(t) \equiv \frac{\bar{B}^0(t) - B^0(t)}{\bar{B}^0(t) + B^0(t)} = \sin 2\beta \cdot \sin \Delta m_d t\,, \tag{81}$$

where $B^0(t)$ $[\bar{B}^0(t)]$ is the number of decays to $J/\psi K_S^0$ at proper time t given that the produced meson was a B^0 $(\bar{B}^0)$ at $t = 0$. The CP phase difference between the two decay paths appears via the factor $\sin 2\beta$, and the $B\bar{B}$ flavor oscillation through the mass difference Δm_d between the two B^0 mass eigenstates. Figure 46(a) illustrates the connection between the time dependence of the $B^0\bar{B}^0$ mixing asymmetry $\mathcal{A}_{\rm mix}$ (top) and the CP asymmetry $\mathcal{A}_{CP}$ (bottom) in, for example, $B^0 \to J/\psi K_S^0$ decays. At $t = 0$ we start with a pure $\bar{B}^0$ state. Since no B^0 mesons are present to interfere with, the CP asymmetry is zero. After about two B lifetimes, we have the same amount of B^0 and $\bar{B}^0$ due to mixing $(\mathcal{A}_{\rm mix} = 0)$ and the CP asymmetry is maximal. From this we see that the CP asymmetry follows a sinusoidal time

behavior with $\sin 2\beta$ characterizing the amplitude of this sine curve as shown in Eq. (81) while the mixing asymmetry follows a cosine-like time curve as expressed in Eq. (57).

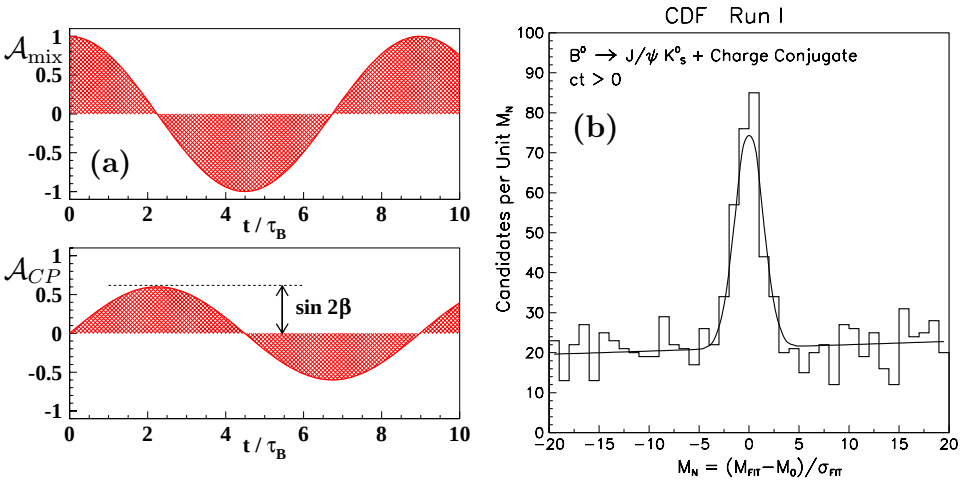

Fig. 46. (a) Illustration of the connection between the time dependence of the $B^0\bar{B}^0$ mixing asymmetry (top) and the CP asymmetry (bottom) in $B^0 \to J/\psi K^0_S$ decays. (b) Normalized mass distribution of $J/\psi K^0_S$ candidates. The curve is the Gaussian signal plus linear background.

The measurement of the CP violation parameter $\sin 2\beta$ using $B^0/\bar{B}^0 \to J/\psi K^0_S$ decays[65] reconstructs J/ψ mesons through $\mu^+\mu^-$ and searches for $K^0_S \to \pi^+\pi^-$ candidates. The J/ψ and K^0_S daughter tracks are combined in a four-particle fit to originate from a common B^0 vertex. The decay length of the B^0 is used to calculate its proper decay length ct. We define $M_N \equiv (m_{\rm fit} - m_0)/\sigma_{\rm fit}$, where $m_{\rm fit}$ is the mass of the B candidate from the fit described above, $\sigma_{\rm fit}$ is its uncertainty (typically ~ 9 MeV/c^2), and m_0 is the central value of the B^0 mass peak. The normalized masses M_N for the selected candidates with $ct > 0$ are shown in Fig. 46(b) along with the result of the maximum log-likelihood fit described later. The fit yields (198 ± 17) $B^0/\bar{B}^0$ mesons for all ct.

To measure $\mathcal{A}_{CP}(t)$, we need to know whether the production flavor of the B meson is B^0 or $\bar{B}^0$. We determine this with a same side tagging method described in Subsec. 7.2. The effectiveness of this method is demonstrated by tagging $B \to D^{(*)}\ell\nu$ decays and observing the time dependence of $B^0\bar{B}^0$ oscillations measuring Δm_d. Applying the SST method to the $J/\psi K^0_S$ sample yields a tagging efficiency of $\sim$65%. Since negative (positive) tags are associated with $\bar{B}^0$'s (B^0's), the asymmetry

$$\mathcal{A}(ct) \equiv \frac{N^-(ct) - N^+(ct)}{N^-(ct) + N^+(ct)} \tag{82}$$

is formed analogously to Eq. (81), where $N^{\pm}(ct)$ are the numbers of positive and negative tags in a given ct bin. The sideband-subtracted asymmetry is displayed in Fig. 47(a) along with a χ^2 fit (dashed curve) to $\mathcal{A}_0 \sin \Delta m_d t$, where Δm_d is fixed[3] to 0.474 ps^{-1}. The amplitude, $\mathcal{A}_0 = 0.36 \pm 0.19$, measures $\sin 2\beta$ attenuated by the dilution factor $\mathcal{D}_0 = 2p_R - 1$, where p_R is the probability that the tag correctly identifies the B flavor.

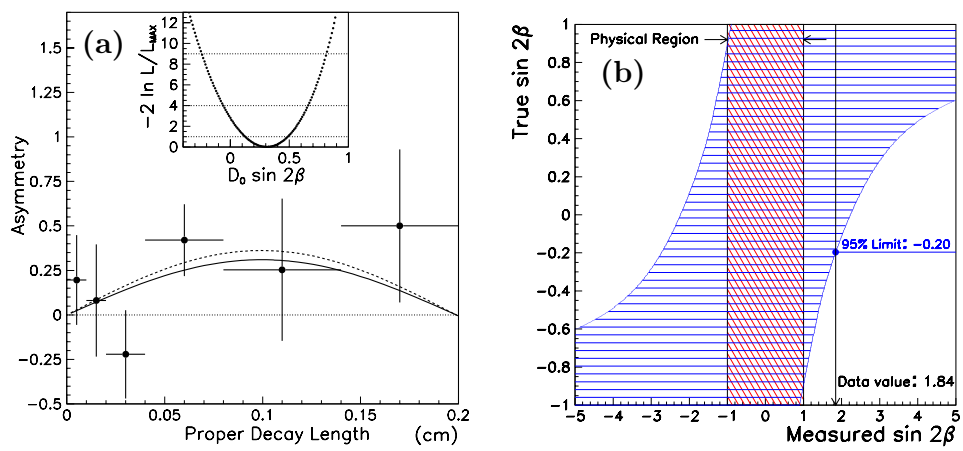

Fig. 47. (a) The sideband-subtracted tagging asymmetry as a function of the reconstructed $J/\psi K_S^0$ proper decay length (points). The dashed curve is the result of a simple χ^2 fit to $\mathcal{A}_0 \sin \Delta m_d t$. The solid curve is the likelihood fit result, and the inset shows a scan through the log-likelihood function as $\mathcal{D}_0 \sin 2\beta$ is varied about the best fit value. (b) "Confidence belt" of the true value of $\sin 2\beta$ versus the measured value of $\sin 2\beta$ used to extract the limit on $\sin 2\beta$.

The fit is refined using an unbinned maximum log-likelihood method. This fit makes optimal use of the low statistics by fitting signal and background distributions in M_N and ct, including sideband and $ct < 0$ events which help constrain the background. The likelihood fit also incorporates resolution effects and corrections for systematic biases, such as the inherent charge asymmetry favoring positive tracks resulting from the wire plane orientation in the main drift chamber. The solid curve in Fig. 47(a) is the result of the likelihood fit, which yields $\mathcal{D}_0 \sin 2\beta = 0.31 \pm 0.18 \pm 0.03$, including systematic effects. As expected, the two fits give similar results, indicating that the result is dominated by the sample size and that the corrections and improvements of the likelihood fit introduce no dramatic effects. Also shown in Fig. 47(a) inset is the relative log-likelihood as a function of $\mathcal{D}_0 \sin 2\beta$. The shape is parabolic, indicating Gaussian errors.

To obtain $\sin 2\beta$, dilution measurements from other B samples are used. CDF's best single $\mathcal{D}_0$ measurement from a large $B \to D^{(*)}\ell X$ sample[31,52] is $0.181^{+0.036}_{-0.032}$ (see Subsec. 7.2). Because of differing lepton p_t trigger thresholds, the average p_t of the semileptonic B sample is $\sim$21 GeV/c, but it is only $\sim$12 GeV/c in the $J/\psi K_S^0$ data. This difference is corrected for using Monte Carlo studies. The $\mathcal{D}_0$ appropriate

for the $J/\psi K_S^0$ sample is found to be $0.166 \pm 0.018 \pm 0.013$, indicating a small shift from 0.181. The first error is due to the uncertainty in the dilution measurement, and the second is due to the Monte Carlo extrapolation.

Using this value of $\mathcal{D}_0$, $\sin 2\beta$ is determined to be

$$\sin 2\beta = 1.8 \pm 1.1 \pm 0.3\,. \tag{83}$$

The central value is unphysical since the amplitude of the measured asymmetry is larger than $\mathcal{D}_0$. To express this result in terms of a confidence interval in $\sin 2\beta$, the frequentist construction by Feldman and Cousins[66] is followed. This approach gives proper confidence intervals even for measurements in the unphysical region. Figure 47(b) shows the "confidence belt" of the true value of $\sin 2\beta$ versus the measured value of $\sin 2\beta$ using the frequentist method. This measurement thereby corresponds to excluding $\sin 2\beta < -0.20$ at 95% confidence level. This result favors current Standard Model expectations of a positive value of $\sin 2\beta$ and establishes the feasibility of measuring CP asymmetries in B meson decays at a hadron collider.

8.2.1. *Updated measurement of the CP violation parameter* $\sin 2\beta$ *in* $B^0 \to J/\psi K_S^0$

Just prior to completion of this article, the CDF collaboration released an updated measurement of the CP violation parameter $\sin 2\beta$ in $B^0 \to J/\psi K_S^0$ decays. This preliminary result combines the same side tagging method with a lepton and jet charge flavor tag (see Subsec. 7.3). In addition, it includes $J/\psi K_S^0$ events which are not fully contained within the acceptance of the SVX detector.

The selection criteria for the $B^0 \to J/\psi K_S^0$ sample with $J/\psi \to \mu^+\mu^-$ and $K_S^0 \to \pi^+\pi^-$ are very similar to the requirements used in the analysis in Subsec. 8.2. To increase the sample size, both muon candidate tracks are no longer required to be measured in the silicon vertex detector. The data are divided into two samples. The non-SVX sample contains events where both muons are not required to have SVX information, accepting events that do not have a precise decay length measurement. However, about 30% of the events in this sample have one muon track with SVX information. The other sample of $J/\psi K_S^0$ decays, called the SVX sample, requires both muons to be well measured in the SVX, providing precise decay length information. This sample is very similar to the data used in the $\sin 2\beta$ analysis described in Subsec. 8.2. The normalized mass distribution (see Subsec. 8.2) for all $J/\psi K_S^0$ candidates is shown in Fig. 48(a), constituting a sample of (395 ± 31) signal events. The SVX sample contains (202 ± 18) signal events while the non-SVX sample consists of (193 ± 26) events.

This analysis combines all three flavor tagging methods studied at CDF. In addition to the same side tagging algorithm, the two opposite side tagging methods, jet charge tagging and lepton tagging, as described in Subsec. 7.3, are added. The tagging dilutions and efficiencies for both opposite side tags are determined from a sample of (985 ± 46) $B^+ \to J/\psi K^+$ events and are presented in Table 7. The SST

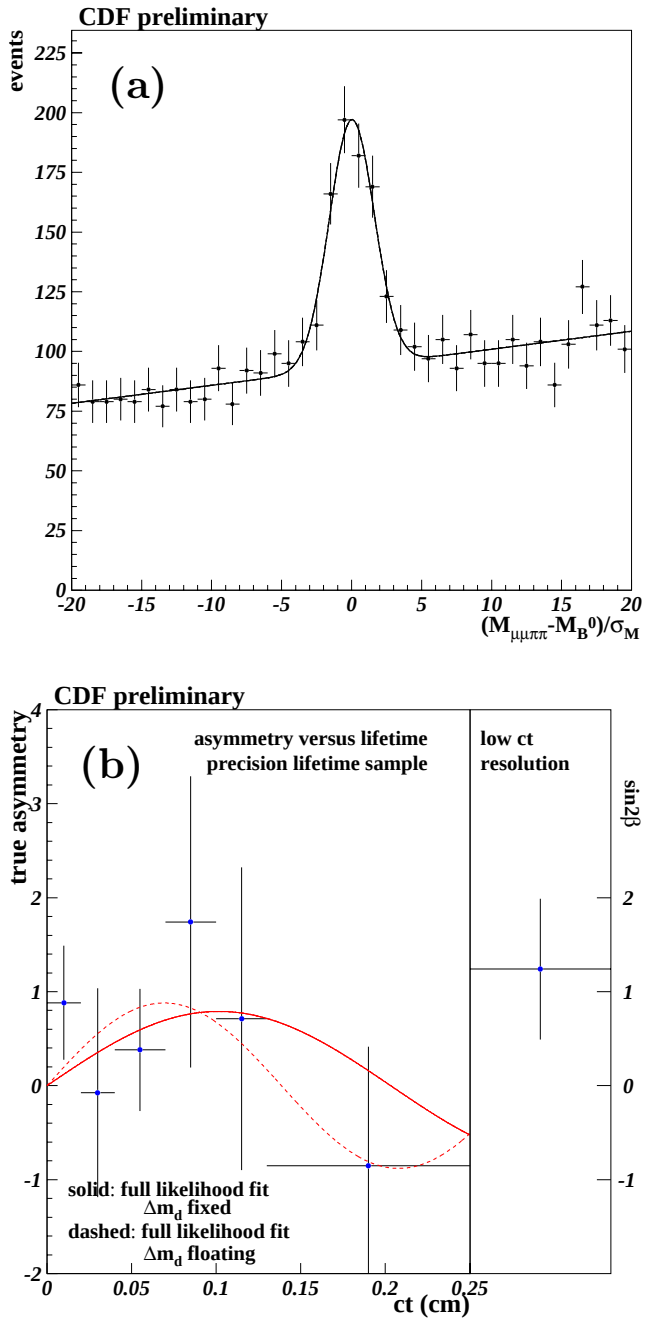

Fig. 48. (a) Normalized mass distribution of $J/\psi K_S^0$ candidates. The curve is the Gaussian signal plus linear background from the log-likelihood fit. (b) True asymmetry $\sin 2\beta$ as a function of the reconstructed $J/\psi K_S^0$ proper decay length. The data points are sideband-subtracted and are combined according to the effective dilution for single and double tags. The non-SVX events are shown on the right.

tagging dilution for the SVX sample ($\mathcal{D} = (16.6 \pm 2.2)\%$) is taken from the $\sin 2\beta$ analysis summarized in Subsec. 8.2. For the non-SVX sample, the SST algorithm is slightly modified to include non-SVX tracks as candidate tagging tracks. A dilution scale factor, which relates the SST tagging performance from the SVX sample to the non-SVX sample, is derived from the $J/\psi K^+$ data resulting in $\mathcal{D} = (17.4 \pm 3.6)\%$ for the non-SVX sample (see also Table 7).

Table 7. Summary of efficiency ε and dilution $\mathcal{D}$ of the tagging algorithms. The quoted efficiencies are relative to the entire $J/\psi K_S^0$ sample. To compare the SST efficiency with the number given in Subsec. 8.2, it is necessary to double the SST efficiency for the SVX sample.

Flavor tag	Data	Efficiency ε	Dilution $\mathcal{D}$	$\varepsilon\mathcal{D}^2$
Same side tag	SVX sample	$(35.5 \pm 3.7)\%$	$(16.6 \pm 2.2)\%$	$(1.0 \pm 0.3)\%$
	non-SVX sample	$(38.1 \pm 3.9)\%$	$(17.4 \pm 3.6)\%$	$(1.2 \pm 0.5)\%$
Lepton tag	all events	$(5.6 \pm 1.8)\%$	$(62.5 \pm 14.6)\%$	$(2.2 \pm 1.2)\%$
Jet charge tag	all events	$(40.2 \pm 3.9)\%$	$(23.5 \pm 6.9)\%$	$(2.2 \pm 1.3)\%$

Each event can be tagged by as many as two tags: one same side tag and one opposite side tag. If both the lepton and jet charge tags are available, only the lepton tag is used, following the $B^0\bar{B}^0$ mixing analysis described in Subsec. 7.3. The procedure used to combine double-tagged events calculates a combined dilution weighted by the individual dilutions and combines the efficiencies in a similar way. Defining the two tags q_1 and q_2 as $+1$ if they identify a B^0 meson, as -1 if they tag a $\bar{B}^0$ and as 0 if the tag is not applicable, the individual tags are weighted by the dilutions $\mathcal{D}_1$ and $\mathcal{D}_2$ according to $\mathcal{D}_1' = q_1\,\mathcal{D}_1$ and $\mathcal{D}_2' = q_2\,\mathcal{D}_2$, respectively. With the individual efficiencies ε_1 and ε_2, the combined dilution $\mathcal{D}_{\rm com}$ and efficiency $\varepsilon_{\rm com}$ are defined as

$$\mathcal{D}_{\rm com} = \frac{\mathcal{D}_1' + \mathcal{D}_2'}{1 + \mathcal{D}_1'\mathcal{D}_2'}\,, \qquad \varepsilon_{\rm com} = \varepsilon_1\varepsilon_2(1 + \mathcal{D}_1'\mathcal{D}_2')\,, \tag{84}$$

where the sign of $\mathcal{D}_{\rm com}$ is the combined tag with dilution $|\mathcal{D}_{\rm com}|$.

In the same way as was summarized in Subsec. 8.2, a maximum log-likelihood method is used to make optimal use of the statistics by fitting signal and background distributions in normalized mass and ct, including sideband events. The true asymmetry as a function of the reconstructed $J/\psi K_S^0$ proper decay length is shown in Fig. 48(b) separately for the SVX and the non-SVX sample with the result of the fit overlaid. The non-SVX sample contribution is included as a single point because of the low decay length resolution. The full log-likelihood fit uses both the SVX and the non-SVX sample and properly treats the decay length and error for each event. The final fit yields

$$\sin 2\beta = 0.79 \pm 0.39 \pm 0.16\,, \tag{85}$$

where the systematic error reflects the uncertainty in the dilution parameters. Although the individual dilutions are not precisely determined due to the limited

statistics of the $B^+ \to J/\psi K^+$ sample, this error does not dominate the uncertainty on $\sin 2\beta$. Removing the constraint that fixes Δm_d to its world average value,[3] the fit determines $\sin 2\beta$ and Δm_d simultaneously to be $\sin 2\beta = 0.88^{+0.44}_{-0.41}$ and $\Delta m_d = (0.68 \pm 0.17)\ \mathrm{ps}^{-1}$, as indicated by the dashed line in Fig. 48(b). The result given in Eq. (85) leads to the confidence interval $\sin 2\beta < -0.08$ (95% CL) using the frequentist method by Feldman and Cousins.[66] This result excludes $\sin 2\beta < 0$ at the 93% confidence level and is the best direct hint for CP violation in the neutral B meson system to date.

9. Future B Physics at CDF

The Fermilab accelerator complex is currently undergoing an upgrade to produce an order of magnitude higher luminosities in the Tevatron collider. The largest change is the replacement of the Main Ring with the new Main Injector, which will provide higher proton intensity onto the antiproton production target, and a larger aperture for the antiproton transfer into the Tevatron, increasing the antiproton current and thus the luminosity of the Tevatron. After the completion of the Main Injector, the Tevatron is scheduled to run again in April 2000 at a center-of-mass energy of 2.0 TeV. In this so-called Run II, luminosities of $2.0 \cdot 10^{32}\ \mathrm{cm}^{-2}\mathrm{s}^{-1}$ will be reached, yielding an integrated luminosity of 2 fb^{-1} delivered to the collider experiments within two years. To handle the higher luminosities and shorter bunch spacing of initially 396 ns and later 132 ns, the CDF experiment is currently undergoing a major detector upgrade. In this section, we first briefly describe the CDF detector upgrade and then summarize the prospects for measuring $\sin 2\beta$ and $\sin 2\alpha$ at CDF in Run II.

9.1. *CDF II detector upgrade*

The CDF detector improvements for Run II are motivated by the shorter accelerator bunch spacing and the increase in luminosity by an order of magnitude. The primary upgrade goal is to maintain detector occupancies at Run I levels, although many of the detector changes also provide qualitatively improved detector capabilities. The CDF II upgrade is described in detail elsewhere.[67] A schematic view of the CDF II detector is shown in Fig. 49(a). We briefly summarize here the changes most relevant for B physics in Run II.

One major upgrade is to the charged particle tracking system [see Fig. 49(b)], vital for the CDF B physics program. A new silicon vertex detector (SVX II) will consist of five layers of double-sided silicon from radii of 2.9 cm to 10 cm arranged in five axial layers, two small angle (1.2°) and three 90° stereo layers. SVX II will consist of three modules covering the entire $p\bar{p}$ luminous region and provide stand-alone three-dimensional tracking. The silicon sensors are read out by a radiation hard chip in deadtimeless mode. In addition, an intermediate silicon layer (ISL) consisting of two double-sided silicon layers at larger radii permits stand-alone silicon tracking out to $|\eta| < 2$. The inner layer provides complete η coverage while

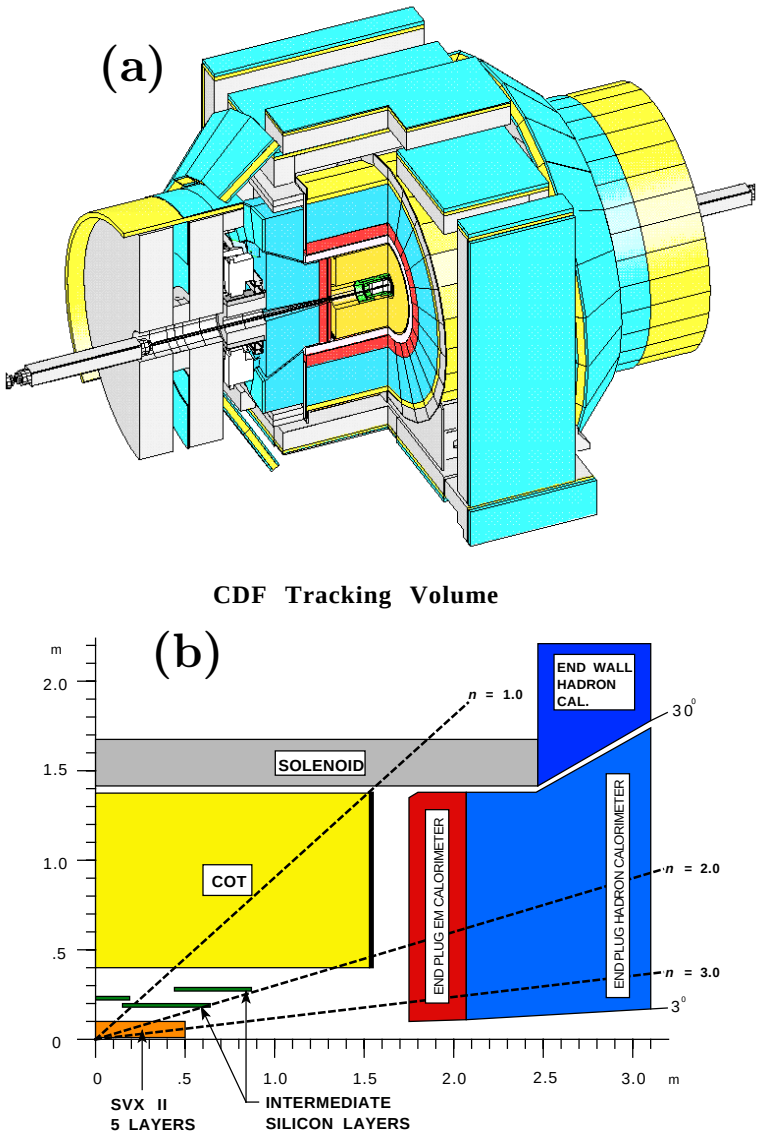

Fig. 49. (a) Schematic cut-away view of the CDF II detector. (b) Longitudinal view of the CDF II tracking system.

the outer layer has partial coverage ($1 < |\eta| < 2$). A new open cell drift chamber (COT) will operate at a beam crossing time of 132 ns without having overlapping events in a single cell. This is accomplished with a fast gas and shorter drift cells of 0.9 cm. The COT consists of 96 layers arranged in four axial and four stereo superlayers. It increases the number of stereo layers from 24 in the CTC to 48 and provides dE/dx information for particle identification.

The upgrades to the muon system almost double the central muon coverage. The CMP coverage increases by $\sim$17% while the CMX system is completed, increasing its coverage by $\sim$45%. A new intermediate muon system (IMU) extends the muon coverage up to $|\eta| < 1.5$ with fine granularity and provides coverage sufficient to identify isolated high p_t tracks as muons or hadrons between $|\eta|$ of 1.5 and 2.0. In addition, a new scintillating tile plug calorimeter will allow good electron identification up to $|\eta| < 2$.

All front-end electronics is designed to handle the 132 ns beam crossing period. The trigger and data acquisition upgrade allows for higher data rates such as a 50 kHz Level 1 accept rate and increases the sophistication of the trigger decision. Data are stored in a 42-cell pipeline while awaiting the Level 1 trigger decision and can be transferred to Level 2 with no deadtime to the Level 1 trigger. Finally, the CDF collaboration has recently proposed two "beyond the baseline" projects which will significantly enhance the B physics capabilities of the CDF II detector. These include the installation of a low-mass radiation hard single-sided silicon detector, with axial strips at a very small radius of ~ 1.6 cm, just outside the beam pipe, as well as the installation of a time-of-flight (TOF) system, employing 216 three-meter-long scintillator bars with fine mesh photomultiplier tubes on each end, to be located between the outer radius of the COT and the superconducting solenoid magnet.

9.2. *Measurement of* $\sin 2\beta$ *in Run II*

CDF has the advantage of being an existing experiment with plenty of data and experience from Run I. We will make use of the Run I knowledge to estimate the Run II expectations for measuring CP violation. For the measurement of $\sin 2\beta$ in the $B^0 \to J/\psi K^0_S$ channel, CDF expects $10,000 J/\psi K^0_S$ events with $J/\psi \to \mu^+\mu^-$ and $K^0_S \to \pi^+\pi^-$. This number is estimated in the following way. Starting with $\sim 200 J/\psi K^0_S$ events reconstructed in the SVX in Run I and multiplying it by 2 fb^{-1}/110 pb^{-1} for the total Run II integrated luminosity, by a factor of 1.5 for the extended coverage of SVX II, and by 2 for a lower p_t threshold of 1.5 GeV/c in the muon trigger, as well as an improved muon coverage with the completed CMX, one obtains 10,800 reconstructed $J/\psi K^0_S$ events. CDF also plans to trigger on $J/\psi \to e^+e^-$, which would increase the number of $J/\psi K^0_S$ events by $\sim 50\%$. However, these data are not included in this estimate.

In Run II, CDF expects to improve the effective tagging efficiencies $\varepsilon\mathcal{D}^2$ of the B flavor tagging methods, as summarized in Table 8. The extended lepton coverage with the completed CMX, IMU, and the plug calorimeter results in a total $\varepsilon\mathcal{D}^2$ of 1.7% for lepton tagging. A significant improvement in $\varepsilon\mathcal{D}^2 \sim 3\%$ is possible for jet charge tagging. The extended coverage of SVX II and ISL as well as their added pattern recognition capabilities will substantially enhance the purity of the algorithm. Finally, for our Run II extrapolation a value of $\varepsilon\mathcal{D}^2 \sim 2\%$ is assumed for same side tagging.

Table 8. Summary of flavor tagging methods used in the measurement of $\sin 2\beta$ in Run II and the data samples used to calibrate the tagging algorithms.

Flavor tag	$\varepsilon\mathcal{D}^2$	Calibration sample	Sample size
Same side tag	2.0%	$J/\psi K^{*0}$	$\sim 20,000$
Jet charge tag	3.0%	$J/\psi K^{+}$	$\sim 40,000$
Lepton tag	1.7%	$J/\psi K^{+}$	$\sim 40,000$

To estimate the uncertainty on a $\sin 2\beta$ measurement in Run II, we extrapolate from the measured error of the Run I result given in Eq. (83), which uses SVX events only. Defining the CP asymmetry as $\mathcal{A} = \mathcal{D}\sin 2\beta$, we obtain $\sin 2\beta = \mathcal{A}/\mathcal{D}$ and write the error on $\sin 2\beta$ as

$$\sigma^2(\sin 2\beta) = \left(\frac{\sigma(\mathcal{A})}{\mathcal{D}}\right)^2 + \left(\sin 2\beta\,\frac{\sigma(\mathcal{D})}{\mathcal{D}}\right)^2 , \tag{86}$$

where we substitute $\mathcal{A}/\mathcal{D}$ with $\sin 2\beta$ in the second term. This way, the error on $\sin 2\beta$ can be broken up into a statistical part from the measurement of the CP asymmetry $\mathcal{A}$ and a systematic part due to the dilution uncertainty. In Run II, the flavor tag dilutions will be calibrated with large samples of about 40,000 $J/\psi K^+$ and $\sim 20,000$ $J/\psi K^{*0}$ events. Assuming $\sin 2\beta = 1$ in the second term of Eq. (86) as the worst case and the same signal-to-noise ratios for the $J/\psi K$ samples as in Run I, the error on a measurement of $\sin 2\beta$ can be estimated to $\sigma^2(\sin 2\beta) = 0.078^2 + 0.031^2$. This will allow the observation of CP violation in Run II and a measurement of $\sin 2\beta$ from $B^0 \to J/\psi K^0_S$ with a precision of ± 0.08, comparable to e^+e^- machines.

9.3. *Measurement of* $\sin 2\alpha$ *in Run II*

Another goal of B physics in Run II is the observation of CP violation in $B^0 \to \pi^+\pi^-$ measuring $\sin 2\alpha$. The key to measuring the CP asymmetry in $B^0 \to \pi^+\pi^-$ is to trigger on this hadronic decay mode in $p\bar{p}$ collisions. CDF plans to do this with its three-level trigger system. On Level 1, two oppositely charged tracks with $p_t > 2$ GeV/c found with a fast track processor yield an accept rate of about 22 kHz at luminosities of $\sim 1.0 \cdot 10^{32}$ cm^{-2}s^{-1}. This rate will be reduced to less than $\sim$25 Hz on Level 2 using track impact parameter information ($d_0 > 100$ μm). On Level 3, the full event information is available, further reducing the trigger rate to about 1 Hz. With this trigger, CDF expects about 10,000 $B^0 \to \pi^+\pi^-$ events in 2 fb^{-1}, assuming that BR$(B^0 \to \pi^+\pi^-) = 1.0 \cdot 10^{-5}$. With the same effective tagging efficiency as in the $\sin 2\beta$ measurement above (see Table 8), CDF estimates an uncertainty of 0.10 on $\sin 2\alpha$. Backgrounds from $B \to K\pi$ and $B \to KK$ decays can be extracted from the untagged signal by making use of the invariant mass distribution, as well as CDF's dE/dx capability with the COT.

10. Conclusions

The CDF collaboration has shown that it is possible to take advantage of the high production rate for B hadrons at the Tevatron Collider. The key elements for a broad B physics program at a hadron collider are the successful operation of a silicon vertex detector to identify B decay vertices displaced from the primary $p\bar{p}$ interaction vertex, the excellent tracking capabilities of CDF's central tracking chamber, together with the silicon vertex detector and the use of specialized triggers. Due to these features of the CDF detector together with the high yield of B hadrons, the hadron collider B physics program complements that at e^+e^- machines.

In this article, we gave a brief overview of heavy quark production in $p\bar{p}$ collisions and described some of the features of B physics at a hadron collider. We reviewed the B hadron lifetime measurements at CDF, all very competitive with results from LEP and SLC. We discussed several proper-time-dependent measurements of $B^0\bar{B}^0$ oscillations as well as B tagging methods to identify the B flavor in hadronic collisions. The application of all B flavor tags to the current data set of $B^0 \to J/\psi K_S^0$ decays at CDF established the feasibility of measuring CP asymmetries in B meson decays at a hadron collider. With many years of experience in B physics at the Tevatron, the CDF collaboration plans to observe CP violation in $B^0 \to J/\psi K_S^0$ in the next run of the Tevatron collider scheduled to start in the year 2000 and will measure $\sin 2\beta$ with a precision comparable to the dedicated e^+e^- B factories.

Acknowledgments

The results assembled in this article are the work of the CDF collaboration. It is a pleasure to thank all friends and colleagues at CDF and especially the CDF B physics group for their excellent work. I wish to thank especially F. Bedeschi, J. Boudreau, K. Burkett, B. Carithers, F. DeJongh, L. Galtieri, M. Garcia-Sciveres, C. Gay, A. Goshaw, C. Haber, J. Kroll, C. Lacunza, N. Lockyer, O. Long, J. Lys, P. Maksimović, M. Mangano, V. Papadimitriou, M. Peters, K. Pitts, M. Schmidt, M. Shapiro, P. Sinervo, P. Sphicas, D. Stuart, S. Tkaczyk, F. Ukegawa, as well as B. Wicklund. This article is dedicated to my wife, Ann, a constant source of inspiration and support, and to our daughter Emma, born during the preparation of this manuscript. I would like to thank them both for their continuous understanding about the life of a physicist. The standard acknowledgments of the CDF collaboration follow: We thank the Fermilab staff and the technical staffs of the participating institutions for their vital contributions. This work was supported by the U.S. Department of Energy and the National Science Foundation; the Italian Istituto Nazionale di Fisica Nucleare; the Ministry of Education, Science and Culture of Japan; the Natural Sciences and Engineering Research Council of Canada; the National Science Council of the Republic of China; the Swiss National Science Foundation; and the A.P. Sloan Foundation.

References

1. S. W. Herb *et al.*, *Phys. Rev. Lett.* **39**, 252 (1977).
2. Ch. Berger *et al.* (PLUTO Collaboration), *Phys. Lett.* **B76**, 243 (1978); C. W. Darden *et al.* (DASP Collaboration), *Phys. Lett.* **B76**, 246 (1978).
3. C. Caso *et al.* (Particle Data Group), *Eur. Phys. J.* **C3**, 1 (1998).
4. S. L. Glashow, *Nucl. Phys.* **22**, 579 (1961); S. Weinberg, *Phys. Rev. Lett.* **19**, 1264 (1967); A. Salam, *Elementary Particle Theory*, ed. N. Svartholm (Almquist and Wiksells, Stockholm, 1969), p. 367.
5. N. Cabibbo, *Phys. Rev. Lett.* **10**, 531 (1963).
6. M. Kobayashi and T. Maskawa, *Prog. Theor. Phys.* **49**, 652 (1973).
7. N. Ellis and A. Kernan, *Phys. Rep.* **195**, 23 (1990).
8. P. Nason, in *Heavy Flavors*, eds. A. J. Buras and M. Lindner (World Scientific, Singapore, 1992); R. K. Ellis, W. J. Stirling and B. R. Webber, *QCD and Collider Physics* (Cambridge University Press, 1996).
9. S. Frixione, M. L. Mangano, P. Nason and G. Ridolfi, in *Heavy Flavors II*, eds. A. J. Buras and M. Lindner (World Scientific, Singapore, 1998). Also hep-ph/9702287.
10. M. L. Mangano, Lectures at the International School of Physics "E. Fermi," *Heavy Flavor Physics: A Probe of Nature's Grand Design*, CERN-TH/97-328 (1997). Also hep-ph/9711337.
11. G. Altarelli and G. Parisi, *Nucl. Phys.* **B126**, 298 (1977).
12. V. N. Gribov and L. N. Lipatov, *Sov. J. Nucl. Phys.* **15**, 438 (1972); L. N. Lipatov, *Sov. J. Nucl. Phys.* **20**, 95 (1975); Yu. L. Dokshitzer, *Sov. Phys. JETP* **46**, 641 (1977).
13. A. D. Martin, R. G. Roberts and W. J. Stirling, *Phys. Rev.* **D47**, 867 (1993).
14. A. D. Martin, R. G. Roberts and W. J. Stirling, *Phys. Lett.* **B306**, 145 (1993); *Phys. Rev.* **D50**, 6734 (1994); *Phys. Lett.* **B354**, 155 (1995); *Eur. Phys. J.* **C4**, 463 (1998).
15. J. Botts *et al.* (CTEQ Collaboration), *Phys. Lett.* **B304**, 159 (1993).
16. H. L. Lai *et al.* (CTEQ Collaboration), *Phys. Rev.* **D55**, 1280 (1997).
17. M. Glück, J. F. Owens and E. Reya, *Phys. Rev.* **D17**, 2324 (1978); L. M. Jones and H. Wyld, *Phys. Rev.* **D17**, 782 (1978); J. Babcock, D. Sivers and S. Wolfram, *Phys. Rev.* **D18**, 162 (1978); H. M. Georgi, S. L. Glashow, M. E. Machacek and D. V. Nanopoulos, *Ann. Phys.* **114**, 273 (1978); B. L. Combridge, *Nucl. Phys.* **B151**, 429 (1979); K. Hagiwara and T. Yoshino, *Phys. Lett.* **B80**, 282 (1979).
18. Z. Kunszt and E. Pietarinen, *Nucl. Phys.* **B164**, 45 (1980); G. Kopp, H. J. Kühn and P. Zerwas, *Phys. Lett.* **B153**, 315 (1985); F. Halzen and P. Hoyer, *Phys. Lett.* **B154**, 324 (1985); V. Barger and R. J. N. Phillips, *Phys. Rev.* **D31**, 215 (1985); A. Ali and G. Ingelman, *Phys. Lett.* **B156**, 111 (1985).
19. P. Nason, S. Dawson and R. K. Ellis, *Nucl. Phys.* **B303**, 607 (1988); W. Beenakker, H. Kuijf, W. L. van Neeren and J. Smith, *Phys. Rev.* **D40**, 54 (1989); W. Beenakker, W. L. van Neeren, R. Meng, G. A. Schuler and J. Smith, *Nucl. Phys.* **B351**, 507 (1991).
20. P. Nason, S. Dawson and R. K. Ellis, *Nucl. Phys.* **B327**, 49 (1989); M. L. Mangano, P. Nason and G. Ridolfi, *Nucl. Phys.* **B373**, 295 (1992).
21. T. Sjöstrand, *Int. J. Mod. Phys.* **A3**, 715 (1988).
22. C. Peterson, D. Schlatter, I. Schmitt and P. Zerwas, *Phys. Rev.* **D27**, 105 (1983).
23. J. Binnewies, B. A. Kniehl and G. Kramer, *Phys. Rev.* **D58**, 034016 (1998).
24. F. Abe *et al.* (CDF Collaboration), *Nucl. Instrum. Methods* **A271**, 387 (1988), and references therein.
25. D. Amidei *et al.*, *Nucl. Instrum. Methods* **A350**, 73 (1994).
26. P. Azzi *et al.*, *Nucl. Instrum. Methods* **A360**, 137 (1995).

27. G. W. Foster, J. Freeman, C. Newman-Holmes and J. Patrick, *Nucl. Instrum. Methods* **A269**, 93 (1988).
28. H.-U. Bengtsson and T. Sjöstrand, *Comput. Phys. Commun.* **46**, 43 (1987); "PYTHIA 5.7 and JETSET 7.4: Physics and Manual," by T. Sjöstrand (Lund Univ.) LU-TP-95-20 (1995).
29. P. Avery, K. Read and G. Trahern, Cornell Internal Note CSN-212, 1985 (unpublished).
30. H. L. Lai *et al.* (CTEQ Collaboration), *Phys. Rev.* **D51**, 4763 (1995).
31. F. Abe *et al.* (CDF Collaboration), *Phys. Rev.* **D59**, 032001 (1999).
32. M. B. Voloshin and M. A. Shifman, *Sov. Phys. JETP* **64**, 698 (1986); I. I. Bigi and N. G. Uraltsev, *Phys. Lett.* **B280**, 271 (1992); I. I. Bigi, *Nuovo Cimento* **A109**, 713 (1996).
33. M. Neubert, *Int. J. Mod. Phys.* **A11**, 4173 (1996); M. Neubert and C. T. Sachrajda, *Nucl. Phys.* **B483**, 339 (1997).
34. E. Fernandez *et al.* (MAC Collaboration), *Phys. Rev. Lett.* **51**, 1022 (1983); N. Lockyer *et al.* (MARKII Collaboration), *Phys. Rev. Lett.* **51**, 1316 (1983).
35. F. Abe *et al.* (CDF Collaboration), *Phys. Rev. Lett.* **71**, 3421 (1993).
36. F. Abe *et al.* (CDF Collaboration), *Phys. Rev.* **D57**, 5382 (1998).
37. F. Abe *et al.* (CDF Collaboration), *Phys. Rev.* **D58**, 092002 (1998).
38. F. Abe *et al.* (CDF Collaboration), *Phys. Rev.* **D59**, 032004 (1999).
39. I. Bigi, B. Blok, M. Shifman, N. Uraltsev and A. Vainshtein, in *B Decays*, 2nd ed., ed. S. Stone (World Scientific, Singapore, 1994), p. 132. Also hep-ph/9401298.
40. I. Dunietz, *Phys. Rev.* **D52**, 3048 (1995).
41. M. Beneke, G. Buchalla and I. Dunietz, *Phys. Rev.* **D54**, 4419 (1996).
42. J. Hagelin, *Nucl. Phys.* **B193**, 123 (1981); V. A. Khoze, M. A. Shifman, N. G. Uraltsev and M. B. Voloshin, *Sov. J. Nucl. Phys.* **46**, 112 (1987); A. Datta, E. A. Paschos and U. Türke, *Phys. Lett.* **B196**, 382 (1987); I. Dunietz, *Ann. Phys.* **184**, 350 (1988).
43. E. Golowich, *Proc. 30th Recontre de Moriond, QCD and High Energy Hadronic Interactions* (Meribel les Allues, France, 1995), ed. J. Trân Thanh Vân (Editions Frontieres, 1995). Also hep-ph/9505381.
44. F. Abe *et al.* (CDF Collaboration), *Phys. Rev. Lett.* **77**, 1439 (1996).
45. F. Abe *et al.* (CDF Collaboration), *Phys. Rev.* **D58**, 112004 (1998).
46. F. Abe *et al.* (CDF Collaboration), *Phys. Rev. Lett.* **81**, 2432 (1998).
47. W. Kwong and J. Rosner, *Phys. Rev.* **D44**, 212 (1991); E. Eichten and C. Quigg, *Phys. Rev.* **D49**, 5845 (1994).
48. M. Lusignoli and M. Masetti, *Z. Phys.* **C51**, 549 (1991); S. S. Gershtein *et al.*, *Int. J. Mod. Phys.* **A6**, 2309 (1991); P. Colangelo *et al.*, *Z. Phys.* **C57**, 43 (1993); C. Quigg, *Proc. Workshop on B Physics at Hadron Accelerators*, eds. P. McBride and C. Shekhra Mishra, Fermilab-CONF-93/267 (SSCL-SR-1225) (1994); I. I. Bigi, *Phys. Lett.* **B371**, 105 (1996); M. Beneke and G. Buchalla, *Phys. Rev.* **D53**, 4991 (1996).
49. M. Gell-Mann and A. Pais, *Phys. Rev.* **97**, 1387 (1955).
50. E. E. Lande *et al.*, *Phys. Rev.* **103**, 1901 (1956).
51. H. Albrecht *et al.* (ARGUS Collaboration), *Phys. Lett.* **B192**, 245 (1987).
52. F. Abe *et al.* (CDF Collaboration), *Phys. Rev. Lett.* **80**, 2057 (1998).
53. M. Gronau, A. Nippe and J. Rosner, *Phys. Rev.* **D47**, 1988 (1993).
54. P. Abreu *et al.* (DELPHI Collaboration), *Phys. Lett.* **B345**, 598 (1995); R. Akers *et al.* (OPAL Collaboration), *Z. Phys.* **C66**, 19 (1995); D. Buskulic *et al.* (ALEPH Collaboration), *Z. Phys.* **C69**, 393 (1996).
55. B. Andersson, G. Gustafson, G. Ingelman and T. Sjöstrand, *Phys. Rep.* **97**, 31 (1983).
56. F. Abe *et al.* (CDF Collaboration), Fermilab-Pub-99/019-E (1999).

57. F. Abe *et al.* (CDF Collaboration), *Phys. Rev.* **D50**, 2966 (1994); *Phys. Rev. Lett.* **74**, 2626 (1995).
58. D. Buskulic *et al.* (ALEPH Collaboration), *Z. Phys.* **C75**, 397 (1997); P. Abreu *et al.* (DELPHI Collaboration), *Z. Phys.* **C72**, 17 (1996); R. Akers *et al.* (OPAL Collaboration), *Phys. Lett.* **B327**, 411 (1994); K. Abe *et al.* (SLD Collaboration), *Phys. Rev. Lett.* **74**, 2890 (1995).
59. M. Paulini, *Proc. IV Int. Workshop on Progress in Heavy Quark Physics* (Rostock, Germany, 1997), eds. M. Beyer, T. Mannel and H. Schröder (1998). Also hep-ex/9802018.
60. F. Abe *et al.* (CDF Collaboration), Fermilab-Pub-99/030-E (1999).
61. J. H. Christenson, J. W. Cronin, V. L. Fitch and R. Turlay, *Phys. Rev. Lett.* **13**, 138 (1964).
62. J. Aubert *et al.*, *Phys. Rev. Lett.* **33**, 1404 (1974); J. E. Augustin *et al.*, *Phys. Rev. Lett.* **33**, 1406 (1974); G. E. Abrams *et al.*, *Phys. Rev. Lett.* **33**, 1453 (1974).
63. L. Wolfenstein, *Phys. Rev. Lett.* **51**, 1945 (1983).
64. A. B. Carter and A. I. Sanda, *Phys. Rev. Lett.* **45**, 952 (1980); *Phys. Rev.* **D23**, 1567 (1981); I. I. Bigi and A. I. Sanda, *Nucl. Phys.* **B193**, 85 (1981).
65. F. Abe *et al.* (CDF Collaboration), *Phys. Rev. Lett.* **81**, 5513 (1998).
66. G. J. Feldman and R. D. Cousins, *Phys. Rev.* **D57**, 3873 (1998).
67. R. Blair *et al.* (CDF Collaboration), *The CDF II Detector: Technical Design Report*, Fermilab-Pub-96/390-E (1996).